ROLE OF NUCLEAR ROTATION IN H_2^+ DISSOCIATION BY ULTRASHORT LASER PULSES

by

FATIMA ANIS

M.S., University of the Punjab, 2002

AN ABSTRACT OF A DISSERTATION

submitted in partial fulfillment of the
requirements for the degree

DOCTOR OF PHILOSOPHY

Department of Phyiscs
College of Arts and Sciences

KANSAS STATE UNIVERSITY
Manhattan, Kansas
2009

Abstract

The nuclear rotational period of the simplest molecule H_2^+ is about 550 fs, which is more than 35 times longer than its vibrational period of 15 fs. The rotational time scale is also much longer than widely available ultrashort laser pulses which have 10 fs or less duration. The large difference in rotational period and ultrashort laser pulse duration raises questions about the importance of nuclear rotation in theoretical studies of H_2^+ dissociation by these pulses. In most studies, reduced-dimensionality calculations are performed by freezing the molecular axis in one direction, referred to as the aligned model. We have systematically compared the aligned model with our full-dimensionality results for total dissociation probability and field-free dynamics of the dissociating fragments. The agreement between the two is only qualitative even for ultrashort 10 fs pulses. Post-pulse dynamics of the bound wave function show rotational revivals. Significant alignment of H_2^+ occurs at these revivals. Our theoretical formulation to solve the time-dependent Schrödinger equation is an important step forward to make quantitative comparison between theory and experiment. We accurately calculate observables such as kinetic energy, angular, and momentum distributions. Reduced-dimensionality calculations cannot predict momentum distributions. Our theoretical approach presents the first momentum distribution of H_2^+ dissociation by few-cycle laser pulses. These observables can be directly compared to the experiment. After taking into account averaging steps over the experimental conditions, we find remarkable agreement between the theory and experiment. Thus, our theoretical formulation can make predictions. In H_2^+ dissociation by pulses less than 10 fs, an asymmetry in the momentum distribution occurs by the interference of different pathways contributing to the same energy. The asymmetry, however, becomes negligible after averaging over experimental conditions.

In a proposed pump-probe scheme, we predict an order of magnitude enhancement in the asymmetry and are optimistic that it can be observed.

ROLE OF NUCLEAR ROTATION IN H_2^+ DISSOCIATION BY ULTRASHORT LASER PULSES

by

FATIMA ANIS

M.S., University of the Punjab, 2002

A DISSERTATION

submitted in partial fulfillment of the
requirements for the degree

DOCTOR OF PHILOSOPHY

Department of Phyiscs
College of Arts and Sciences

KANSAS STATE UNIVERSITY
Manhattan, Kansas
2009

Approved by:

Major Professor
Dr. Brett D. Esry

Copyright

This document is prepared using LaTeX

Abstract

The nuclear rotational period of the simplest molecule H_2^+ is about 550 fs, which is more than 35 times longer than its vibrational period of 15 fs. The rotational time scale is also much longer than widely available ultrashort laser pulses which have 10 fs or less duration. The large difference in rotational period and ultrashort laser pulse duration raises questions about the importance of nuclear rotation in theoretical studies of H_2^+ dissociation by these pulses. In most studies, reduced-dimensionality calculations are performed by freezing the molecular axis in one direction, referred to as the aligned model. We have systematically compared the aligned model with our full-dimensionality results for total dissociation probability and field-free dynamics of the dissociating fragments. The agreement between the two is only qualitative even for ultrashort 10 fs pulses. Post-pulse dynamics of the bound wave function show rotational revivals. Significant alignment of H_2^+ occurs at these revivals. Our theoretical formulation to solve the time-dependent Schrödinger equation is an important step forward to make quantitative comparison between theory and experiment. We accurately calculate observables such as kinetic energy, angular, and momentum distributions. Reduced-dimensionality calculations cannot predict momentum distributions. Our theoretical approach presents the first momentum distribution of H_2^+ dissociation by few-cycle laser pulses. These observables can be directly compared to the experiment. After taking into account averaging steps over the experimental conditions, we find remarkable agreement between the theory and experiment. Thus, our theoretical formulation can make predictions. In H_2^+ dissociation by pulses less than 10 fs, an asymmetry in the momentum distribution occurs by the interference of different pathways contributing to the same energy. The asymmetry, however, becomes negligible after averaging over experimental conditions.

In a proposed pump-probe scheme, we predict an order of magnitude enhancement in the asymmetry and are optimistic that it can be observed.

Table of Contents

List of Figures

List of Tables

Acknowledgments

I am truly grateful to Allah, the most beneficent and the most merciful, for giving me the opportunity to earn a Ph.D. and strength to continue my education in difficult times. I prayed for His kindness and forgiveness in our lives and hereafter.

The person on the top of my list to acknowledge is my advisor Prof. Brett D. Esry. I wish to acknowledge him for giving me the opportunity to work with him, for providing a comfortable, friendly and enjoyable work environment, for being patient with my occasional slow progress, for understanding and cooperation in my difficult times to work, for encouraging and guiding me in our research problems, and for the confidence I gained through my progress towards the Ph.D. My aim for the Ph.D was to learn, and it is his kind supervision and habit to interact with students that enabled me to learn a lot. Brett is an outstanding advisor and an excellent person. I will extend this learning experience through our future collaboration. I would like to recognize useful discussions with Prof. Itzik Ben-Itzhak, which particularly helped building my understanding about the experimental setup and observables. I also acknowledge other members on the committee for taking time to read my dissertation. Earlier in my Ph.D., Brett's former post-docs Jose, Remi and Vladimir helped me learn a basic knowledge of Linux, programing, and plotting. I am thankful to them for their help as at that time problems with commands and programming were unsolvable in my mind. I appreciate support from Jesus and Dustin in improving parts of this dissertation and also acknowledge them, our other group members, and Itzik's group's current and former members for useful conversations and a good time. Particularly, I enjoyed working with Jarlath and acknowledge him for constructive discussions about pump-probe studies and for recognizing vibrational suppression and performing experiments based on our theoretical results. Dr. Kevin Carnes gave me a generous favor and took time to read my dissertation. Mostly, finalizing this dissertation have been achieved because of him reading this thesis to find many spelling and grammatical errors. I appreciate his help a lot in this regard. I

am also grateful to Siddique for taking time to implement all those changes. Furthermore, I want to credit all my school, F.Sc, B.Sc, M.Sc, and Ph.D. teachers for their effort and contribution in building my knowledge. I want to acknowledge them as their teaching has only encouraged me in all these stages to continue my academic career.

On a personal note, my parents are the sole reason for my education. I want to acknowledge my father for sending all his children to school on limited resources and difficult times. I also owe a lot of thanks to my mother for her sacrifices and prayers through the course of my life. I acknowledge her for always reminding me that time is too precious to waste and for wishing nothing but education for all her children. I am also thankful to my sisters and brother for their prayers and good wishes, and friends for their support. I acknowledge my mother- and father-in-law for their prayers and continuously reminding us to remain focused on our studies. I also want to acknowledge my son's babysitter, for taking good care of him and for giving him extra time when I was extremely busy writing my dissertation. I acknowledge my two years old son, Daniyal S. Khan, for his love that makes me feel happy. After finishing my Ph.D., I hope I will be able to spend more time with him.

Finally, I again want to acknowledge my husband, Siddique J. Khan. I do not have appropriate words to weigh his encouragement and cooperation in finishing my Ph.D., my dissertation, and in everything I do. I thank him with deep love for his support.

I acknowledge the Chemical Sciences, Geo-Sciences, and Biosciences Division, Office of Basic Energy Sciences, Office of Science, U.S. Department of Energy for the financial support.

Dedication

To my great parents, my
loving husband and my cute
son

Chapter 1

Introduction

1.1 Interaction of atoms and molecules with intense short laser pulses

Understanding the dynamics of atoms and molecules in intense laser fields is currently an active area of research. One reason for this activity is the potential for using broad bandwidth ultrashort pulses to control various physical processes. One of the first steps in efficient control is understanding the fundamental dynamics involved. Fortunately for this endeavor, laser technology has flourished, and ultrashort laser pulses can themselves be controlled quite well. At the same time, fragment imaging techniques have also flourished, allowing complete measurements of simple processes [15–19]. The convergence of these technologies has led to a renewed interest in studying the dynamics of the simplest molecule, H_2^+ [20–23].

The Hydrogen molecular ion H_2^+, was discovered by J. J. Thomson in 1907 [24, 25]. Burru in 1927 obtained its first successful solution for the fixed nuclei and the moving electron by numerical integration [26] of the newly developed Schrödinger wave equation (1926) [27]. See Ref. [28] for a review of the theoretical study of the structure of H_2^+. Some experimental and theoretical studies for photodissociation of H_2^+ were already performed in 1951 [29]. Ever since the birth of the LASER (light amplification by stimulated emission and radiation), physicists have found reasons to revisit the dissociation of H_2^+ by "short laser

pulses" to understand the dynamics during its break up and envision dynamics of complex molecules based on this understanding. Thus H_2^+ provides a benchmark system for diatomic molecules.

Depending on the available technology at a given time, short or ultrashort laser pulses refer to pulses with different duration. As the regime changes for the available pulses, so does the meaning of ultrashort pulses. With progressing laser technology from nanosecond to less than ten femtosecond pulses, questions arise about the behavior of H_2^+ on these shorter and shorter time scales. In fact, as laser pulses get shorter, previously studied phenomena need to be re-examined, as they form the basis of our physical intuition. That intuition, however, may be underpinned by assumptions — good for long pulses — that fail for short pulses.

For more than a decade, most theoretical and experimental studies have involved the interaction of H_2^+ with a Ti:Sapphire laser with central wavelength ranging from 760 to 800 nm and pulse lengths from a few hundred femtoseconds to less than 10 fs and laser intensities up to 10^{16} W/cm^2 [20, 30–43]. In most of the recent experiments, short pulses like 10 fs are used to study ionization and dissociation of H_2^+ [4][22, 44–47].

Many phenomena have emerged from extensive experimental and theoretical work involving laser interaction with the simplest molecule H_2^+. Absorption of one-photon by H_2^+ is commonly referred as bond-softening and gives the dominant contribution to the H_2^+ dissociation [37]. The one-photon dissociation for weak fields is mostly referred to as photodissociation and is commonly used to do spectroscopic measurement and to calculate absorption cross sections for different rotational and vibrational levels of molecules [29, 48–54]. In an analogy to above-threshold ionization of atoms, dissociation can occur by absorbing more than one photon and is thus called above-threshold dissociation (ATD) [4][55–57]. Some of the fragments dissociate with very low kinetic energy, and the phonomenon responsible for this behavior is known as below-threshold dissociation [58]. As a special case of below-threshold dissociation, if fragments dissociate with near zero kinetic energy it is referred to as zero-photon dissociation.

For fixed internuclear distances of about 7 and 10 a.u. (1 a.u. $= 5.29 \times 10^{-9}$ cm), enhancement in the ionization of H_2^+, and also other molecules, was reported by Zuo and Bandrauk [59]. The signature of this enhancement was a characteristic double peak structure in the kinetic energy distribution of the ionization fragments. Enhanced ionization at a crictical internuclear distance corresponds to each peak in the kinetic energy distribution. Theoretical calculations with dynamical nuclei do not show the enhancement. Instead of double peaks, multiple peak structure in the kinetic energy release (KER) spectrum of H_2^+ ionization at low KER was observed [43, 60]. In an analogy to above-threshold ionization and above-threshold dissociation, the multiple peaks can be explained due to the absorption of more than minimum number of photons required to ionize. Thus, the effect is called above threshold Coulomb explosion [43].

In a strong electric field, the electron gets ionized by an oscillating field but as the field changes its direction, it can drive electrons back to the nuclei. Electrons which are driven back to the nuclei by the electric field are called rescattered electrons and the phenomenon is termed as rescattering [61]. Rescattered electrons can recombine with the parent ion and recombination causes the electrons to emit harmonics of the oscillating field. This phenomenon of generating harmonics is termed high harmonic generation [62, 63]. In addition to high harmonic generation, returning electrons to the nuclei can also rescatter and thus provide structural information about the atoms and molecules [64, 65]. High harmonic generation and the structural information obtained from rescattered electrons depend on the orientation and alignment of the molecule [66]. The topic of ionization, rescattering, and high harmonic generation are not discussed in the dissertation. It is, however, important to note that the approximations which are revisited in this work may also be reconsidered for these phenomena.

Laser parameters can effect the phenomena of bond-softening, above-threshold dissociation, above-threshold Coulomb explosion, high harmonic generation and rescattering of electrons. Experimental and theoretical study and understanding of these phenomena sug-

gest different control schemes for dissociation and ionization by varying laser parameters [4][43].

Technological advances in short, intense laser pulses have made it possible to do pump-probe studies of interesting dynamics in atoms and molecules [67, 68]. A pump pulse creates a coherent vibrational or rotational wavepacket in the molecules and the wavepacket evolves according to structural properties of the molecules. A subsequent probe pulse monitors the dynamics by the instantaneous ionization process. Mostly, it is assumed that the probe pulse ionizes molecules or atoms and does not initiate dynamics in an unpredictable way. The energy and angular distrubitions of the fragments, therefore, can be used to find the state of the system at the time delay between pump and probe pulses. In a particular example, a pump initiates a coherent bound vibrational and rotational wavepacket in H_2^+, the wavepacket evolves to become dephased and later revives to its initial shape. A probe pulse can monitor the dephasing and rephasing to provide information about the revival times of these wavepackets either in KER or angular distributions for vibrational or rotational revivals respectively.

To look into the ultrafast dynamics of the molecules, probe pulses should be shorter than the time scale of motion. Three time scales can be associated with the degrees of freedom of our benchmark system, H_2^+. It contains two protons and one electron. The electron has its orbital motion on the time scale of a few hundred attoseconds. Nuclei can have vibrational and rotational motion. Estimates from the difference in the lowest two vibrational states give the fastest vibrational motion on the time scale of 15 femtoseconds, and finally the time scale for the fastest rotational motion is about 550 femtoseconds. Thus, the nuclear vibration is about two orders of magnitude slower than the electronic rotation. This difference in electronic and vibrational time periods is the basis of the Born-Oppenheimer (BO) approximation. And clearly nuclear rotation is the slowest among all degrees of freedom. H_2^+ can either dissociate into p+H or can ionize into $p + p + e^-$ by intense laser fields. My focus will be on the dissociation of H_2^+. Since, in this process, the electron remains bound

to one of the protons, nuclear vibration and rotation are the relavent time scales. To probe vibrational dynamics, pulses with duration $\leq$ 10 fs are appropriate to use. For the short pulses of about 10 fs duration, 55 times shorter than the rotational period of 550 fs, the question arises "*Does the nuclear rotation play any role in H_2^+ dissociation and affect the dynamics*?" This is exactly the question I have tried to answer in my work for the past four years for many aspects of H_2^+ dissociation, and I have been able to convert my findings into my dissertation (see [3–5] for some of our publications).

Unfortunately, even though H_2^+ is the simplest molecule, calculating its response to an intense laser field still lies beyond our abilities if all degrees of freedom are retained. For this reason, it has become common to neglect nuclear rotation, fixing the molecular axis along the laser polarization, based on the observation that these aligned molecules dominate dissociation and ionization processes. This observation was made in early calculations that included nuclear rotation for long pulses [20]. The resulting angular distribution of dissociation fragments was tightly focused along the polarization direction. Since then, the vast majority of calculations have assumed aligned, non-rotating molecules, even when the typical pulse lengths became shorter than the free rotation period, $\approx$ 550 fs for H_2^+. For very short pulses like 10 fs, the argument to neglect nuclear rotation relies on geometric alignment, that is only those molecules can dissociate which are preferentially aligned along laser polarization. The aligned, non-rotating molecule approximation, commonly referred to as the aligned model, nowadays appears to be taken by many as a more serious quantitative tool for understanding intense field dissociation. Even so, there are studies that still recognize the importance of including rotation to obtain quantitative agreement with experiment [31, 69].

In most studies, the time-dependent Schrödinger equation for H_2^+ is solved in the BO representation. According to the BO approximation, since electronic motion is much faster than nuclear motion because of the large difference in their masses (the reduced mass of the nuclei is $\sim$ 1000 times larger than the electron mass), the electronic part of the total Hamil-

tonian can be solved for a fixed internuclear distance. The electronic part of the Hamiltonian is known as the adiabatic Hamiltonian. The solutions of the adiabatic Hamiltonian are BO basis functions, and the internuclear-distance-dependent energy eigenvalues give BO potentials for the nuclear motion. Born-Oppenheimer potentials, essentially electronic energy levels, are also called electronic channels. For H_2^+ dissociation, mostly the lowest two electronic channels $1s\sigma_g$ and $2p\sigma_u$, with a dissociation limit of p+H($1s$), have been included in theoretical calculations. A detailed description of the method is documented in the following chapter.

We revisit the H_2^+ dissociation including nuclear rotation and vibration and the necessary electronic states. Wherever possible we compare our results with the aligned model calculation to find its limitations. In the aligned model, the dissociation probability for initial vibrational states of the nuclei becomes small with an increase in laser intensity [20, 30, 33]. We refer to this behavior as stabilization. It was already found that stabilization can be suppressed after including nuclear rotation in some cases [33]. In our study, we found that for an initial spherical distribution stabilization disappears completely in all cases after including nuclear rotation [3].

The expectation value of $\langle \cos^2 \theta \rangle$, where θ is the angle between the laser polarization direction and the internuclear axis, provides information about the angular distribution of both the bound and dissociating parts of the wave function. A laser pulse initiates coherent rotational and vibrational wavepackets in the bound wave function for the short pulses used in our study. We found the revival time to be about 4 ps, much larger than the rotational period of 550 fs. Typical revival times for individual vibrational states are comparable to the rotational period. Detailed discussion about the dynamics of the bound nuclear wave function will come in Chap. 5

Moreover, discussion about the dynamics of the dissociating fragments leads to some surprising conclusions about the axial-recoil approximation and dynamic alignment [5]. According to the axial-recoil approximation, the angular distribution of the fragments at the

detector and at the moment the molecule breaks are the same, that is nuclei move along the internuclear axis after ionization or dissociation. We also calculate the more differential physical observables like the kinetic energy release spectrum, the angular distribution and the momentum distribution of the dissociating fragments. These observables can be compared to the experimental results after necessary averaging which depends on experimental conditions [4, 12].

Two important concepts are used to describe most of the phenomena related to H_2^+ dissociation in this dissertation. I find it important to briefly describe these in the introduction.

1.2 Incoherent Franck-Condon averaging

In an experiment, H_2^+ is typically created in two different ways. For an experiment involving the interaction of an intense laser field with a neutral H_2 target, H_2^+ is created by the field ionization of H_2. Field ionization launches a coherent vibrational wavepacket on the $1s\sigma_g$ potential curve of H_2^+. This coherent wavepacket can later be dissociated or ionized by the same pulse or by another probe pulse. The coherent wavepacket retains the phase information between its creation and subsequent ionization or dissociation.

In another scenario, H_2^+ is created in an ion source by electron-impact ionization of H_2. The ionization occurs on a time scale much shorter than the nuclear vibration and can be best described by the Franck-Condon principle. According to the Franck-Condon (FC) principle, an instantaneous electronic transition between two molecular states is accurately represented by a vertical transition, that is at constant internuclear distance [70]. Thus the ground vibrational state of H_2 becomes the initial state in H_2^+ and can be expressed as a linear combination of all the vibrational states of H_2^+. The distribution of ground H_2 vibrational states in terms of H_2^+ vibrational states is called the Franck-Condon distribution. In electron-impact ionization, the Franck-Condon distribution gives a good approximation to the initial vibrational states distribution [71].

After creation, H_2^+ ions are accelerated towards the laser beam and travel for microsec-

onds before their interaction with the laser. Moreover, in an ion-beam molecules have a velocity distribution over the averaged beam velocity and the travel time varies for different molecules. Therefore, to get the exact phase information about the initial state, phases should be integrated over the distribution of travel times, which effectively makes the initial vibrational state distribution an "incoherent Franck-Condon distribution". Thus the incoherent FC-averaged expectation value of any observable O will be

$$\langle O \rangle = \sum_v f_v \langle O \rangle_v \tag{1.1}$$

In Eq. (1.1), the summation is over the bound vibrational states v in the $1s\sigma_g$ channel of the H_2^+. Franck-Condon factors f_v in Eq. (1.1) are defined as

$$f_v = |\langle \chi_v | g \rangle|^2, \tag{1.2}$$

the overlap between the lowest vibrational state wave function $g(R)$ of H_2 and the wave functions $\chi_v(R)$ for the bound vibrational states in H_2^+. Sometimes $\langle \chi_v | g \rangle$ are called the Franck-Condon factors. Since we are only using incoherent FC-averaging, for simplicity we will refer to $|\langle \chi_v | g \rangle|^2$ as FC-factors. In H_2^+, bound vibrational states of the $1s\sigma_g$ potential account for about 98 percent of the H_2 vibrational state population. The rest of the population dissociates after electron-impact ionization of H_2.

To include the field ionization of H_2 exactly in a theoretical formulation is a complete study by itself. Our focus is to perform the exact calculations for H_2^+ dissociation by intense short laser pulses. Thus, our study corresponds to an ion-beam experiment. So, we start calculations from individual bound vibrational states of $1s\sigma_g$ and perform "incoherent FC-averaging" of the observables to make connection with the experiment.

1.3 Diabatic Floquet picture

The diabatic Floquet picture is an intuitive way to understand different H_2^+ dissociation pathways. According to the diabatic Floquet representation, the BO potential curves are

dressed by $\pm n$ photons and the transition occurs between different photon curves by diabatic coupling (See Ref. [72] for a review on the Floquet formalism). We want to identify different dissociation processes by their final states in the diabatic Floquet picture. For that, the lowest two potential curves of H_2^+ are plotted in Fig. 1.1. Figure 1.1 shows the $1s\sigma_g$ potential (red lines) shifted by 0ω and 2ω, and the $2p\sigma_u$ potential (black lines) by 1ω and 3ω. We will refer to these four potentials by their thresholds $1s\sigma_g - 0\omega(2\omega)$ and $1s\sigma_g - 1\omega(3\omega)$, respectively.

Some of the commonly used terms for dissociation processes are based on adiabatic Floquet potential curves. These are bond-softening (BS) and vibrational trapping (VT). Adiabatic potential curves are obtained by diagonalizing the field-dressed diabatic potential curves with dipole coupling. In adiabatic potentials, diabatic crossings become avoided crossings, and the transitions between different adiabatic pathways occur by non-adiabatic coupling. The gaps between avoided crossings become larger with the field strength, or, in other words, the crossings "soften". Thus, the adiabatic dissociation pathway that goes to $2p\sigma_u - 1\omega$ is normally referred to as bond-softening (marked as BS in Fig. 1.1) [36]. Another common phenomenon which relies on the adiabatic Floquet representation is vibrational trapping (marked as VT in Fig. 1.1). In adiabatic potential curves, a well is formed above the avoided crossing between $1s\sigma_g - 0\omega$ and $2p\sigma_u - 1\omega$ curves and the vibrational states lying above the avoided crossing become trapped in the well. This trapping is referred to as vibrational trapping (VT).

The adiabatic and diabatic representations are completely equivalent. We want to use the diabatic Floquet representation to define a simple notation for different photon processes briefly described in Sec. 1.1 by their final states. These dissociation processes are zero-photon dissociation, bond-softening, above-threshold dissociation, and below-threshold dissociation. Zero-photon dissociation is a net-zero photon process and a specialized case of below-threshold dissociation.

First, we will identify different curve crossings. We define the crossing between $1s\sigma_g - 0\omega$

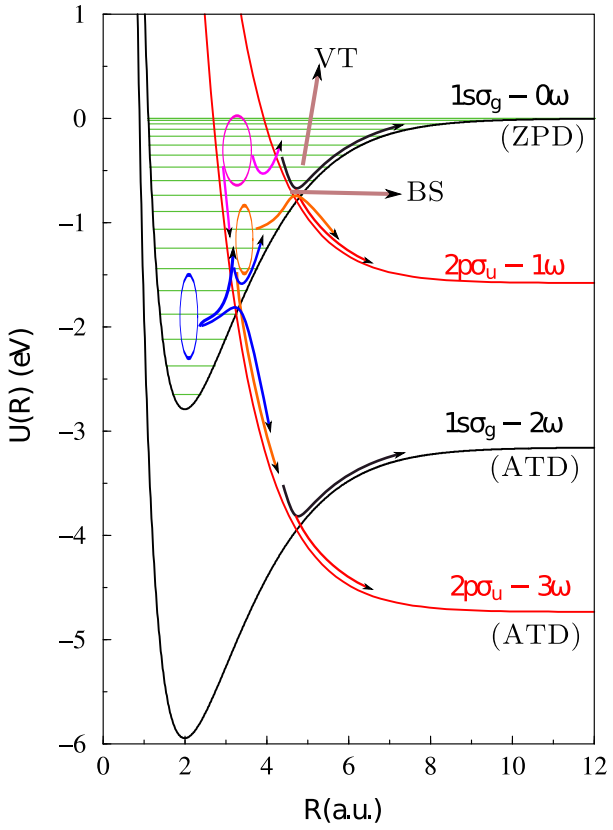

Figure 1.1 Diabatic Floquet picture; green horizontal lines are bound vibrational energy levels in $1s\sigma_g - 0\omega$ for zero total orbital angular momentum; Ellipses show the group of states dissociating with similar dissociation pathways indicated by the colored arrows. Dominant dissociation for all the states in the orange ellipse and above is 1ω.

and $2p\sigma_u - 1\omega$ as "one photon crossing". The crossing between $1s\sigma_g - 0\omega$ and $2p\sigma_u - 3\omega$ is "three photon crossing", and "two photon crossing" is the crossing between $1s\sigma_g - 2\omega$ and $2p\sigma_u - 3\omega$. Now, we define different dissociation processes by identifying the pathways and thresholds.

- Zero-photon dissociation is most likely for the vibrational states above the one-photon crossing. It occurs by a transition to $2p\sigma_u - 1\omega$ and then back to $1s\sigma_g - 0\omega$. The population can move back and forth between the $1s\sigma_g - 0\omega$ and $2p\sigma_u - 1\omega$ above the one-photon crossing and is equivalent to vibrational trapping. So, zero-photon dissociation occurs in the $1s\sigma_g - 0\omega$ channel and we will call it 0ω dissociation. Note that 0ω dissociation is a two photon process and the transitions described above cannot explain how it occurs. In Fig. 1.1, the curves are shifted by assuming negligible

bandwidth of the laser. The diabatic potentials should have blurry lines with widths given by the bandwidth of the laser. And the transition to $2p\sigma_u - 1\omega$ from a high edge of the bandwidth and to $1s\sigma_g - 0\omega$ by a lower frequency will cause 0ω dissociation.

- Dissociation by bond-softening is most likely for the vibrational states by an adiabatic transition at the one-photon crossing, which is $v = 9$ for 785 nm wavelength. The threshold for bond-softening is $2p\sigma_u - 1\omega$ and thus will be referred to as 1ω. Vibrational states lying above and below the one-photon crossing can also make adiabatic transitions to the $2p\sigma_u - 1\omega$ channel and therefore can dissociate by 1ω (vibrational states in magenta and orange ellipses in Fig. 1.1). However, the transition probability is larger for the states closer to the crossing.

- Below-threshold dissociation occurs for the vibrational states lying below the $2p\sigma_u - 1\omega$ threshold (most likely for states in blue ellipse in Fig. 1.1). Dissociation pathways involve transitions from $1s\sigma_g - 0\omega$ to $2p\sigma_u - 3\omega$, back to $1s\sigma_g - 0\omega$, and then to $2p\sigma_u - 1\omega$. To differentiate between multiple transitions to $2p\sigma_u - 1\omega$ and a single transition to $2p\sigma_u - 1\omega$, as in 1ω dissociation, we call the net-1ω dissociation below-threshold dissociation. Since net-1ω dissociation involves many transitions, it is less probable compared to 1ω dissociation.

- Above threshold dissociation refers to dissociation at n photon thresholds with $n \geq 2$ for 785 nm wavelength. It is most likely for the vibrational states at the three-photon crossing ($v = 3$ for 785 nm) and can occur for any vibrational state. The farther the state is from the crossing, the smaller the probability will be. We want to identify two pathways for above-threshold dissociation. After the transition at the three-photon crossing, the population can adopt the adiabatic pathway by a transition at the two-photon crossing to $1s\sigma_g - 2\omega$ or can follow the diabatic pathway to $2p\sigma_u - 3\omega$. So, instead of using above-threshold dissociation, we refer to adiabatic and diabatic pathways by 2ω and 3ω dissociation, respectively.

So, in this dissertation, 0ω represents zero-photon dissociation, 1ω represents bond-softening, net-1ω represents below-threshold dissociation, and 2ω and 3ω represent above-threshold dissociation. The kinetic energy of the dissociating fragments can be estimated by the difference between the vibrational energy level (green lines in Fig. 1.1) and the dissociation thresholds.

Chapter 2

Theoretical formulation to solve the time-dependent Schrödinger equation for H_2^+ in a laser field

2.1 Introduction

There are a limited number of problems for which the time-independent Schrödinger equation has analytic solutions. This number becomes really small for analytic solutions to the time-dependent Schödinger equations (TDSE) involving time-dependent coupling (only one and two free charged particles have an analytic solution in oscillating fields). This left as the only choice solving TDSE by numerical techniques. H_2^+ is the simplest molecule, consisting of only two protons and one electron, and yet state-of-the-art numerical schemes offer solutions to the TDSE of H_2^+ only for four dimensions (three spatial and one time), while the system has five spatial dimensions with azimuthal symmetry. If all the dimensions would be included, then the existing techniques are limited to the dissociation of H_2^+ and thus exclude ionization. For a review about H_2^+ ionization and dissociation see Ref. [20, 21]. For H_2^+ dissociation, most of the calculations are performed in the BO-representation and are limited to the lowest two electronic states of H_2^+, namely $1s\sigma_g$ and $2p\sigma_u$. Most of the recent calculations do not incude nuclear rotation and are also limited to two channels.

Pioneering work on solving H_2^+ numerically including nuclear vibration and rotation with primarily the two lowest electronic channels has been done mainly by Giusti-Suzor and co-

workers [73], Bandrauk and Chelkowski and co-workers [30, 74, 75], and O. Atabek and co-workers [31, 69, 76–78]. Their work dates back to the time when most of the short laser pulses had a duration of a few hundreds femtoseconds. Nuclear rotation was considered to be important as the pulse duration was comparable to the rotational period (556 fs for H_2^+). Two main approaches are used to include nuclear rotation in these calculations. In one approach, nuclear rotation is included as a partial wave expansion [30, 73–75] In a different method it is included by explicitly solving for the angular part of the wave function using a grid [31, 69, 76–78]. Grid solutions are used for the nuclear vibrational motion in all cases.

The angular distribution of the dissociating fragments produced by linearly polarized laser pulses of a few hundred femtoseconds (fs) duration, were found to be narrowly aligned along the laser polarization [20]. This shows that either the molecule becomes aligned during the pulse and then dissociates (dynamical alignment) or only the aligned molecules dissociate (geometric alignment). Both of these arguments suggest that aligned molecules dominate the dissociation in a linearly polarized laser field. This leads to the reduced-dimensional theoretical studies of H_2^+ by fixing the internuclear axis along the laser polarization and excluding nuclear rotation. Moreover, with advances in laser technology to generate ultrashort pulses with few femtoseconds duration, it has become customary to neglect nuclear rotation, which is extremely slow compared to the time scale of the pulse duration [20, 21, 30, 32, 79–82]. Nevertheless, we found it important to check the role of nuclear rotation on some of the theoretical predictions based on aligned model calculations for few or few tens of femtoseconds laser pulses.

2.2 Theory

We solved the time-dependent Schrödinger equation using the Born-Oppenheimer (BO) representation[1]. We first solved the field-free Hamiltonian to get the time-independent BO basis to later use to construct the total time-dependent wave function. The details of our

[1]Part of the work in this chapter has appeared in our previous publication [3].

solution of the field-free equations are given in a previous publication [83], but here we summarize it briefly for completeness. The field-free Hamiltonian for H_2^+ is (atomic units are used hereafter unless otherwise indicated)

$$H_0 = -\frac{1}{2\mu}\nabla_R^2 - \frac{1}{2}\nabla_r^2 - \frac{1}{r_A} - \frac{1}{r_B} + \frac{1}{R}, \tag{2.1}$$

where $\mu = m/2$ with m the nuclear mass, $\mathbf{r}_A$ and $\mathbf{r}_B$ are the position vectors of the electron relative to the two nuclei, and R is the inter nuclear distance. The adiabatic Hamiltonian is defined as follows:

$$H_{\text{ad}} = -\frac{1}{2}\nabla_r^2 - \frac{1}{r_A} - \frac{1}{r_B} + \frac{1}{R}. \tag{2.2}$$

We used prolate spheroidal coordinates to solve the resulting adiabatic equation

$$H_{\text{ad}}\phi_\beta(R;\xi,\eta) = U_\beta(R)\phi_\beta(R;\xi,\eta). \tag{2.3}$$

Note that in this work we have neglected all non-BO terms arising from the R-dependence of the spheroidal coordinates ξ and η and of the adiabatic solutions ϕ themselves. A detailed discussion of these terms can be found in [83]. We solve Eq. (2.3) directly using two-dimensional, direct product b-splines [83]. The label β in Eq. (2.3) represents the quantum numbers (n, Λ, σ_z)[2]. While convenient computationally, this notation is somewhat nonstandard, so we define them as follows: n is the separated atom principal quantum number, Λ is the magnitude of the projection of electronic orbital angular momentum along the internuclear axis in the body-fixed frame as usual, and σ_z is the reflection symmetry through the $z = 0$ plane in the body-fixed frame. These quantum numbers are related to the usual "gerade" and "ungerade" labels by $\sigma_z(-1)^\Lambda = +1$ or -1, respectively.

While the BO potential curves and electronic dipole coupling matrix elements are the same in all the methods used in the present work, the nuclear kinetic energy operator has been treated differently in each of our three methods. The following subsections describe these differences.

[2]The order here is slightly different than the one used in our published article Ref. [3], to link closely to the standard notation of the $1s\sigma_g(2p\sigma_u)$ channel for $\{n = 1, \Lambda = 0, \sigma_z = +(-)\}$.

2.2.1 Time-Dependent Born-Oppenheimer Representation with Nuclear Rotation (TDBOR)

We used this method for all the calculations in this dissertation, and compared the results to other methods occasionally. As mentioned above, our first task was to find the time-independent solutions of the field-free Hamiltonian Eq. (2.3). With nuclear rotation included, these solutions are eigenstates of the total orbital angular momentum. The laser field couples these angular momentum states together, so the total time-dependent wave function will necessarily be a linear combination of these states. This section first details our construction of the time-independent solutions, then outlines their use in the time-dependent Schrödinger equation.

Following the procedure described in [83], we rewrite the nuclear orbital angular momentum $\mathbf{L}$ in terms of the total orbital angular momentum $\mathbf{J}$ and the electronic orbital angular momentum $\mathbf{l}$ as $\mathbf{L} = \mathbf{J} - \mathbf{l}$. As usual, we will work in the body frame, giving

$$\mathbf{L}^2 = \mathbf{J}^2 + \mathbf{l}^2 - 2l_z^2 - l_+J_- - l_+J_-. \tag{2.4}$$

The last two terms account for the Coriolis coupling, with $J_\pm$ and $l_\pm$ the ladder operators for total and electronic orbital angular momentum, respectively. For our present calculations, we neglect both the Coriolis coupling terms and the electronic orbital angular momentum components l_x^2 and l_y^2. We expect the effect of the these terms to be small. Since, the Coriolis terms couple electronic channels with different Λ and there is a large energy gap between the lowest σ and π channels. The projection of the electronic orbital angular momentum along the internuclear axis has the biggest impact on the transition and thus we neglect l_x^2 and l_y^2. Nevertheless, one might check the validity of these approximations. These approximations let us write the field-free nuclear Hamiltonian in the simple form

$$H = -\frac{1}{2\mu}\frac{\partial^2}{\partial R^2} + \frac{\mathbf{J}^2 - l_z^2}{2\mu R^2} + H_{\text{ad}}. \tag{2.5}$$

After all of the approximations described above, we are left with six good quantum numbers $\alpha = \{J, M, \Pi, n, \Lambda, \sigma_z\}$ — the last three were defined previously, and we add total orbital

angular momentum J and its lab frame z-projection M, and the total parity Π. The total wave function is now

$$\Psi(\mathbf{R},\mathbf{r}) = F_\alpha(R)\Phi_\alpha(R;\mathbf{r},\theta,\phi). \tag{2.6}$$

The explicit form of the adiabatic basis functions Φ_α is

$$\Phi_\alpha = \phi_{n\sigma_z\Lambda}(R;\xi,\eta)\Omega^{J\Pi}_{M\Lambda}(\theta,\phi,\chi). \tag{2.7}$$

Equation (2.3) defines $\phi_{n\sigma_z\Lambda}(R;\xi,\eta)$, and the body-frame electronic azimuthal coordinate χ has been incorporated into the angular momentum function $\Omega^{J\Pi}_{M\Lambda}$, which depends on the two nuclear angles θ and ϕ as well. In addition to being an eigenstate of J^2, J_z, and l_z, $\Omega^{J\Pi}_{M\Lambda}$ is also an eigenfunction of the total parity (Π) and nuclear exchange symmetry $\hat{P}_{12}$, and is defined in terms of Wigner D-functions as

$$\Omega^{J\Pi}_{M\Lambda}(\theta,\phi,\chi) = \frac{1}{\sqrt{2(1+\delta_{\Lambda 0})}}\sqrt{\frac{2J+1}{8\pi^2}}\left[D^J_{-M-\Lambda}(\phi,\theta,\chi) + \Pi(-1)^{J+\Lambda}D^J_{-M\Lambda}(\phi,\theta,\chi)\right]. \tag{2.8}$$

This particular representation of the rotational degrees of freedom is not so standard in molecular physics, but is quite standard in few body physics [84]. Similar previous work [33, 73], for example, used the more standard expansion over spherical harmonics. To solve the TDSE numerically, we did not adopt existing techniques but generated the computer program by ourselves. Since we are calculating all quantities from scratch, however, we found it more convenient to use Wigner D-functions. Equation (2.8), in fact, reduces to spherical harmonics for $\Lambda = 0$ or $M = 0$, but is a somewhat more convenient representation for generalizing to higher Λ and M. Note that for $\Lambda = 0$, Π is not an independent quantum number, but instead is related to J by $\Pi = (-)^J$. Using Ψ from Eq. (2.6) in the time-independent Schrödinger equation with the Hamiltonian from Eq. (2.5), projecting out $\langle\Phi_\alpha|$, and neglecting non-BO terms leads to a set of uncoupled time-independent differential equations for the nuclear wave function $F(R)$ for each channel α of the form

$$\left(-\frac{1}{2\mu}\frac{\partial^2}{\partial R^2} + \frac{J(J+1)-\Lambda^2}{2\mu R^2}\right)F_\alpha(R) + U_{n\sigma_z\Lambda}(R)F_\alpha(R) = EF_\alpha(R). \tag{2.9}$$

	J	M	Π	Λ	σ_z
$M=0$	$J'=J\pm1$	$M'=M$	$\Pi'=-\Pi$	$\Lambda'=\Lambda,\Lambda\pm1$	$(-)^{\Lambda'}\sigma'_z=-(-)^{\Lambda}\sigma_z$
$M\neq0$	$J'=J,J\pm1$	$M'=M$	$\Pi'=-\Pi$	$\Lambda'=\Lambda,\Lambda\pm1$	$(-)^{\Lambda'}\sigma'_z=-(-)^{\Lambda}\sigma_z$

Table 2.1 Dipole selection rules. Transitions are possible within each n manifold and to all others that support a given Λ' channel. For example, transitions to $\Lambda=1$ are possible for all $n\geq2$.

We used the dipole approximation to include the laser field and wrote the interaction energy in the length gauge as $-\boldsymbol{\mathcal{E}}(t)\cdot\mathbf{d}$, where $\boldsymbol{\mathcal{E}}(t)$ is the electric field and $\mathbf{d}$ is the dipole operator. This term modifies Eq. (2.9) by coupling different adiabatic channels α. Consequently, the total time-dependent wave function takes the form

$$\Psi(\mathbf{R},\mathbf{r},t)=\sum_{\alpha}F_{\alpha}(R,t)\Phi_{\alpha}(R;\mathbf{r},\theta,\phi). \tag{2.10}$$

Using this Ψ, we obtain the following set of time-dependent coupled partial differential equations for the nuclear wave functions in a laser field:

$$i\frac{\partial}{\partial t}F_{\alpha}=\left(-\frac{1}{2\mu}\frac{\partial^2}{\partial R^2}+\frac{J(J+1)-\Lambda^2}{2\mu R^2}+U_{n\Lambda\sigma_z}(R)\right)F_{\alpha}-\boldsymbol{\mathcal{E}}(t)\cdot\sum_{\alpha'}\langle\Phi_{\alpha}|\mathbf{d}|\Phi_{\alpha'}\rangle F_{\alpha'}. \tag{2.11}$$

Since the laser polarization is defined in the lab frame and the electronic states are defined in the body frame, some care must be taken in evaluating the dipole interaction energy. All necessary details are given in App. A. For all calculations, we have used linearly polarized light and so only the lab frame z-component of the dipole operator is required. Without discussing the dipole matrix in detail, it would be useful to identify the selection rules for the transitions between different channels between α and α'. The selection rules are listed in Table. 2.1. The only difference between initial $M=0$, and initial $M\neq0$ seems to be in the allowed J transition. However, initial $M\neq0$ doubles the number of channels for all the electronic states with $\Lambda\geq1$. This can be explained by noting that all the electronic states with $\Lambda\geq1$ are doubly degenerate. Equation. (2.8) shows that the electronic states with $\Lambda\geq1$ will have even parity states. An initial $M=0$ allows only the parity favored transition and thus only half of the Λ states contribute, however, for higher M's all the states can be populated.

We solved Eq. (2.11) numerically, approximating the radial kinetic energy operator with a generalized three-point difference scheme [85, 86]. The time evolution combined split operator techniques with a Crank-Nicholson-like approximation. Similar propagation schemes have been successfully implemented in our previous work [1][15, 85]. I will provide a brief description of the numerical method here. For a small time step δ, the wave function evolves according to

$$\mathbf{F}(R, t+\delta) = e^{-i\delta\mathbf{H}(t+\delta/2)}\mathbf{F}(R, t), \tag{2.12}$$

where the elements of $\mathbf{F}$ are the radial functions F_α. For the purposes of deriving an algorithm to implement the discretized version of this expression, Eq. (2.11) can be regarded as two-dimensional in R and α. For our time-dependent Hamiltonian,

$$\mathbf{H}(t) = \mathbf{H}_0 + \mathcal{E}(t)\mathbf{D}_z, \tag{2.13}$$

the field-free part $\mathbf{H}_0$ is local in the channel space α but couples different R; the dipole interaction is local in R but couples different α through the dipole matrix $\mathbf{D}$. This behavior suggests the split operator scheme

$$e^{-i\delta\mathbf{H}(t+\delta/2)} \approx e^{-i\mathbf{H}_0\delta/2}e^{-i\mathcal{E}(t+\delta/2)\mathbf{D}_z\delta}e^{-i\mathbf{H}_0\delta/2}. \tag{2.14}$$

We approximated each of these exponentials using the Cayley form $e^{i\delta A} \approx (1 - \frac{i}{2}\delta A)^{-1}(1 + \frac{i}{2}\delta A)$. This form is a Padé approximant, is unitary, and is evaluated in practice by solving a system of linear equations. We checked that unitarity and energy are indeed preserved to machine precision in field-free propagation. Overall, this scheme is accurate through order δ^2 — a feature preserved by evaluating $\mathbf{H}(t)$ at the half-steps $t + \delta/2$. See App. C for some of the numerical convergence tests.

2.2.2 Time-Dependent Born-Oppenheimer Representation with Aligned Nuclei (TDBOA)

In this method, the nuclear motion is restricted to vibration along one direction only. So, the nuclear wave function does not have any angular dependence and the molecule does not

rotate. For this study, that fixed direction is along the linearly polarized electric field. Our implementation of this method is detailed in previous work [15]. Many other studies using this method have also been conducted and a wide selection are discussed in the reviews in Refs. [20] and [21].

For an aligned molecule, the expansion of the electronic degrees of freedom on the BO states leads to the following coupled time-dependent equations for the nuclear wave function:

$$i\frac{\partial}{\partial t}F_\beta = \left(-\frac{1}{2\mu}\frac{\partial^2}{\partial R^2} + U_\beta\right)F_\beta - \mathcal{E}(t)\sum_{\beta'}\langle\phi_\beta|z|\phi_{\beta'}\rangle F_{\beta'} \tag{2.15}$$

Here, β stands for n, Λ, and σ_z, as before. Since, we have assumed the molecule to be fixed in space parallel to the laser field, we need only the z-component of the dipole matrix element. The dipole selection rule then dictates that we need only include states with $\Lambda = 0$ and $\sigma_z = \pm 1$ — that is, σ_g and σ_u states — since the initial electronic state is $1s\sigma_g$.

Generally, we don't need to fix the internuclear axis along the laser polarization , but we can also fix it at some angle θ. This allows perpendicular transitions from initial $\Lambda = 0$ to $\Lambda = 1$ by the perpendicular component of the electric field. These transitions are, however, much less probable compared to the parallel transitions. Thus for a nonzero angle θ, calcuations can be performed by solving Eq. (2.15), and changing the electric field amplitude to $\mathcal{E}(t)\cos\theta$.

The numerical scheme implementing this method is the same as described in the last paragraph of Sec. 2.2.1 except that the channel index does not include J (see also Ref. [15]).

2.2.3 Time-Dependent Born-Oppenheimer Representation with Rotation on Lattice (TDBORL)

This approach included nuclear rotation just as the TDBOR in Sec. 2.2.1. The difference is that the angular degree of freedom is represented by direct discretization on a lattice [31, 69, 76] rather than by a basis expansion. As a consequence, we propagated a two-dimensional time-dependent nuclear wave function $F(R, \theta, t)$ for each channel. We eliminated the ϕ-dependence of the total wave function since the linearly polarized pulse conserves M (we

set M=0).

The purpose of performing calculations using TDBORL was to have an independent check of the TDBOR results and to test their accuracy. To this end, we included only two channels for simplicity, taking into account only the $1s\sigma_g$ and $2p\sigma_u$ states. With this restriction, we get the following time-dependent coupled equations:

$$\begin{aligned} i\frac{\partial}{\partial t}F_1 &= \left(H_{R1} + \frac{T_\theta}{R^2}\right) F_1 - \mathcal{E}(t)\cos\theta\langle\phi_1|z|\phi_2\rangle F_2 \\ i\frac{\partial}{\partial t}F_2 &= \left(H_{R2} + \frac{T_\theta}{R^2}\right) F_2 - \mathcal{E}(t)\cos\theta\langle\phi_2|z|\phi_1\rangle F_1 \end{aligned} \tag{2.16}$$

In the above equations, θ is the angle between the polarization direction and the internuclear axis, and the labels 1 and 2 correspond to $1s\sigma_g$ and $2p\sigma_u$, respectively. The radial part of the field-free Hamiltonian for each channel is defined as

$$H_{Ri} = -\frac{1}{2\mu}\frac{\partial^2}{\partial R^2} + U_i(R); \tag{2.17}$$

and the angular kinetic energy T_θ, as

$$T_\theta = \frac{\mathbf{J}^2}{2\mu} = -\frac{1}{2\mu}\frac{1}{\sin\theta}\frac{\partial}{\partial\theta}\left(\sin\theta\frac{\partial}{\partial\theta}\right), \tag{2.18}$$

since both Λ and M are zero.

To solve Eq. (2.16), both the radial and angular kinetic energy operators are approximated by a generalized three-point difference scheme [85, 86] as in the other methods above. We note that our differencing scheme easily handles coordinate systems other than Cartesian. In particular, the singularities at $\theta = 0$ and π in Eq. (2.18) pose no problems. Further, we accomplish this without the usual scaling of the wave function by a factor of $\sqrt{\sin\theta}$ — which is fortunate since the wave function after this scaling is non-analytic and thus cannot be differenced, strictly speaking.

The short time propagator is split into five terms

$$e^{-i\mathbf{H}(t+\delta/2)\delta} \approx e^{-i(\mathbf{T}_\theta/R^2)\delta/2}e^{-i\mathbf{H}_R\delta/2}e^{-i\mathcal{E}(t+\delta/2)\mathbf{D}_z\delta}e^{-i\mathbf{H}_R\delta/2}e^{-i(\mathbf{T}_\theta/R^2)\delta/2}. \tag{2.19}$$

Different numerical methods were used in previous two-dimensional (R, θ) lattice calculations [31, 69, 76].

2.3 Analysis

It was necessary to calculate many physical observables as we studied H_2^+ stabilization and vibrational trapping, field-free dynamics of dissociating and bound wave functions, and finally the kinetic-energy release, angular, and momentum distributions of p+H. Some of the calculated observables are used in multiple places. So, I gather the formulation of all the necessary analysis here to avoid inconsistent notation and confusion about the definition of different terms. For completeness, the most relevant equations will be reused in the following chapters.

2.3.1 Initial state for TDBOR

For all the results presented in this dissertation, we have performed calculations starting from the individual bound vibrational states v of the $1s\sigma_g$ channel. This is explicitly

$$F_{\alpha_i}(R, t_i) = \chi_{vJ}(R). \tag{2.20}$$

Here, $\alpha_i = \{J = J_i, M = M_i, \Pi = (-1)^{J_i}, n = 1, \Lambda = 0, \sigma_z = +1\}$ is the initial channel of H_2^+. So, I will use v to represent the initial vibrational state in all cases. In our study, the initial J_i and the initial M_i are mostly taken to be zero. The functions $\chi_{vJ}(R)$ are the rovibrational bound states of the $1s\sigma_g$ channel [solutions of Eq. (2.9) for the $\{J, 0, (-1)^J, 1, 0, +1\}$ channel].

2.3.2 Initial state for TDBOA

The procedure for TDBOA is nearly identical to TDBOR, except, of course, there is no rotation and thus no J or M. The initial state will be each individual bound vibrational state of the $1s\sigma_g$ channel, and will be identical to the other two methods for our case of initial $J = 0$.

2.3.3 Initial state for TDBORL

This method has only been used to test the accuracy of TDBOR. So, both the TDBOR and TDBORL have the same initial state. For TDBORL, angular dependence is explicitly included to define the nuclear wave function for the $1s\sigma_g$ ($F_1(R,\theta,t)$) channel as,

$$F_1(R,\theta,t_i) = \chi_{v0}(R)\Omega_{00}^{0+}(\theta). \tag{2.21}$$

For $\Lambda = 0$, $\Omega_{M\Lambda}^{J\Pi}$ does not have any χ dependence.

2.3.4 Dissociation probability

In this section, we will calculate the total dissociation probability $P_{\rm D}$ of H_2^+. By "dissociation", we specifically mean breakup of the system into p+H(nlm). In principle, the dissociation probability for each nlm atomic orbital can be measured. We, however, refer to the dissociation probability as the sum of all channels. We calculated $P_{\rm D}$ by projecting out the total bound state probability after the laser pulse. Bound states are possible in the $1s\sigma_g$ channel for Js from 0 to 35; $J > 35$ support no bound rovibrational states. We treat $1s\sigma_g$ as the only channel with bound states, and did not add find any contribution to the bound population from $2p\sigma_u$ bound states. We thus obtained $P_{\rm D}$ for initial $J = 0$ using the following expression:

$$P_{\rm D} = 1 - \sum_{J \text{ even},v'} |\langle \chi_{v'J} \mid F_{+1J010+1}(t)\rangle|^2. \tag{2.22}$$

For TDBOA, we calculated the dissociation probability using Eq. (2.22) without summation over J as there is no rotation.

The expression for $P_{\rm D}$ for TDBORL is

$$P_{\rm D} = 1 - \sum_{Jv'} |\langle \chi_{v'J}\Omega_{00}^{J+}|F_1(t)\rangle|^2. \tag{2.23}$$

In Eqs. (2.22) and (2.23), the sum represents the total bound probability. Thus, it was used whenever it was desirable to calculate the bound probability. Our notation $P_{\rm D}$

represents the incoherent Franck-Condon averaged total dissociation probability.

$$P_{\mathrm{D}} = \sum_{v} f_v P_{\mathrm{D}v} \tag{2.24}$$

with $P_{v\mathrm{D}}$ being the dissociation probability from each v, and f_v being the Franck-Condon factor previously defined in Sec. 1.2. Since for most of the calculations we have taken the initial $J = 0$, we refer to f_{v0} as f_v for smplicity. Similarly, for the bound probability, to do FC-averaging we calculate,

$$P_{\mathrm{B}} = \sum_{v} f_v P_{\mathrm{B}v}. \tag{2.25}$$

2.3.5 Calculating $\langle \cos^2\theta \rangle$ for bound wave function

The observables described in this and following sections are only calculated for the TDBOR method described in Sec. 2.2.1. Another observable in our study is the $\langle \cos^2\theta \rangle$ for the bound and dissociating part of the H_2^+ nuclear wave function. θ is the angle between the body-frame axis and the laser polarization direction in the lab-frame. To study the dynamics of the bound wave function of H_2^+ during and after the pulse, we want to calculate the FC-averaged $\langle \cos^2\theta \rangle$. We will call the FC-averaged $\langle \cos^2\theta \rangle$ simply $\langle \cos^2\theta \rangle$. For anything else different notation has been adopted. The initial state for individual vibrational states is defined in Eq. (2.20). The initial channel for the nuclear function $F_\alpha(R,t)$ at initial time t_i is $\alpha_i = \{J_i, M_i, (-1)^{J_i}, 1, 0, +1\}$[3]. Since we are using linearly polarized laser pulses, M will not change from its initial value (here M will refer to M_i). To perform the analysis during the pulse, the bound probability for individual vibrational states ($P_{\mathrm{B}v}$) is defined using field-free bound rovibrational states as

$$P_{\mathrm{B}v} = \sum_{Jv'} |a_{Jv'}(t)|^2, \tag{2.26}$$

where $a_{Jv'}(t) \equiv \langle \chi_{Jv'} \mid F_{JM\Pi 10+1}(R,t) \rangle$ are the complex amplitudes for populating each rovibrational state at any time during the pulse, and $F_{JM\Pi 10+1}(R,t)$ is the nuclear wave

[3] $1s\sigma_g$ with the J_iM_i rotational and v vibrational level. I will write the expression for the general initial J_i and M_i. The specialized case of $J_i = M_i = 0$ can be obtained from these expressions.

function of $1s\sigma_g$ for each J as a function of time. Note that for the $1s\sigma_g$ channel (as $\Lambda = 0$), the angular basis functions will be

$$\Omega^{J\Pi}_{M0} = \frac{1}{2}\sqrt{\frac{2J+1}{8\pi^2}} D^J_{-M0}[1 + \Pi(-1)^J], \tag{2.27}$$

and the angular part of the basis functions can simply be $\Omega^J_{0M} = \sqrt{2J+1/8\pi^2} D^J_{-M0}$ by dropping Π from the notation. Also, an initial even J means only even Js and an odd initial J corresponds to only odd Js in the bound $1s\sigma_g$ channel. In the case of H_2^+, even Js in $1s\sigma_g$ channels correspond to singlet nuclear spin states, which are anti-symmetric with respect to proton exchange. However, this will be different for D_2^+, where they correspond to symmetric singlet and quartet nuclear spin states. The bound part of the nuclear wave function at any time for each initial vibrational state v can be written as

$$\psi_{Bv}(\mathbf{R}, t) = \sum_J \Omega^J_{0M}(\hat{R}) \sum_{v'} a_{Jv'}(t)\chi_{Jv'}(R); \tag{2.28}$$

and for post-pulse propagation

$$\psi_{Bv}(\mathbf{R}, t > t_f) = \sum_J \Omega^J_{0M}(\hat{R}) \sum_{v'} a_{Jv'}(t_f) e^{-iE_{Jv'}(t-t_f)} \chi_{Jv'}(R). \tag{2.29}$$

Here, the final time t_f defines the end of the pulse , and E_{Jv} is the eigenenergy for the function χ_{Jv}. For $\Lambda = 0$, there is a χ-dependence in Ω^J_{0M}. Using Eq. (2.28), we calculated the expectation value of $\cos^2\theta$ for each v ($\langle\cos^2\theta\rangle_v$) by

$$\begin{aligned}\langle\cos^2\theta\rangle_v(t) \;=\; & \frac{1}{3P_{\mathrm{B}v}(t)}\Bigg[P_{Bv}(t) + 2(-1)^M \sum_J (2J+1) \sum_{v'} |a_{Jv'}(t)|^2 \\ & + 4(-1)^M \sum_J \sqrt{(2J+3)(2J+1)} \begin{pmatrix} J+2 & 2 & J \\ -M & 0 & M \end{pmatrix} \begin{pmatrix} J+2 & 2 & J \\ 0 & 0 & 0 \end{pmatrix} \\ & \times \sum_{v'v''} \langle\chi_{J+2v''}|\chi_{Jv'}\rangle \mathrm{Re}\left(a^*_{J+2v''}(t) a_{Jv'}(t)\right)\Bigg].\end{aligned} \tag{2.30}$$

It follows from Eq. (2.29) that for $t > t_f$, $a_{Jv}(t) = a_{Jv}(t_f)e^{E_{Jv}(t-t_f)}$. After calculating the $\langle\cos^2\theta\rangle_v$, we want to perform incoherent FC-averaging. Equation (2.32) gives a value of one third for an isotropic angular distribution for each v, and thus we would renormalize

$\langle\cos^2\theta\rangle_v$ to ensure the same value for the FC-averaged isotropic angular distribution. Thus $\langle\cos^2\theta\rangle$ is defined as

$$\langle\cos^2\theta\rangle(t) = \frac{1}{P_{\rm B}(t)}\sum_v f_v P_{{\rm B}v}(t)\langle\cos^2\theta\rangle_v(t) \tag{2.31}$$

where, similar to $P_{\rm D}$ in Eq. (2.24), $P_{\rm B}$ is the FC-averaged total bound probability given by $P_{\rm B}(t) = \sum_v f_v P_{{\rm B}v}(t)$.

2.3.6 Calculating $\langle\cos^2\theta\rangle$ for the dissociating wave function

Since I will discuss the dynamics of bound and dissociating H_2^+ in separate places, I will use the same notation of $\langle\cos^2\theta\rangle_v$ for individual v and $\langle\cos^2\theta\rangle$ for the FC-averaged expectation value of $\cos^2\theta$ for both bound and dissociating wave functions. Contrary to the bound wave function, which involves only the single electronic channel of $1s\sigma_g$, all the channels would contribute to the dissociating part of the H_2^+ wave function. Thus for each v

$$\langle\cos^2\theta\rangle_v(t) = \frac{1}{P_{{\rm D}v}}\sum_{\beta,\Pi}\langle\cos^2\theta\rangle_{v,\beta,\Pi}(t) \tag{2.32}$$

Now, $\langle\cos^2\theta\rangle_{v,\beta,\Pi}$ is the value for each electronic channel β, where $\beta = \{n, \Lambda, \sigma_z\}$, and parity Π for $\Lambda > 0$. Since $\cos^2\theta$ depends only on the nuclear coordinate, $\langle\cos^2\theta\rangle_v$ is equal to an incoherent sum of all electronic channels. For the dissociating wave function, it is not efficient to extract amplitudes for all the continuum states for all electronic channels and then use those to analytically calculate $\langle\cos^2\theta\rangle_v(t)$ for $t > t_f$. So, here we numerically propagated the continuum wave function after the pulse in the same way as during the pulse to extract information about the dynamics of $\langle\cos^2\theta\rangle_v(t)$. To get the dissociating wave function for the $1s\sigma_g$, we projected out all the rovibrational states from its nuclear function. Explicitly, for initial $M = 0$,

$$\langle\cos^2\theta\rangle_v(t) = \frac{1}{3P_{{\rm D}v}(t)}\Bigg[P_{{\rm D}v}(t) + 2\sum_\beta(-1)^\Lambda\sum_{JJ'}\langle F_{\beta J'}(t)|F_{\beta J}(t)\rangle \sqrt{(2J+1)(2J'+1)}\begin{pmatrix} J & 2 & J' \\ 0 & 0 & 0\end{pmatrix}\begin{pmatrix} J & 2 & J' \\ \Lambda & 0 & -\Lambda\end{pmatrix}\Bigg]. \tag{2.33}$$

Similar to Eq. (2.31), FC averaging was done by

$$\langle \cos^2\theta \rangle(t) = \frac{1}{P_{\mathrm{D}}(t)} \sum_v f_v P_{\mathrm{D}v}(t) \langle \cos^2\theta \rangle_v(t). \tag{2.34}$$

2.3.7 Theoretical formulation to obtain momentum distribution

A brief description of the steps taken to calculate momentum have been documented in this section, and the detailed description can be found in App. B. To obtain momentum or KER-$\cos\theta$ distributions similar to what has been observed in the experiment, the continuum wave for the dissociating fragments needs to be expressed in terms of the molecular basis defined in Eq. (2.7). Our formulation closely followed the steps described in Ref. [87]. For a particular example, see Ref. [88, 89].

Let us assume at this point that the two protons are distinguishable and are designated as A and B. The vectors $\mathbf{R}$ for internuclear distance and $\mathbf{K}$ for relative momentum are defined from A to B. Note that the scattering coordinate should really be between the proton and the center-of-mass of the atom. Neglecting this small difference is consistent with the Born-Oppenheimer approximation since it is of the same order, but it is an approximation. It also works better here because we are considering relatively small momenta. This issue leads in collisions to electron translation factors. If a molecule is dissociating with the electron localized on proton A then the continuum wavefunction as an expansion of molecular basis is

$$\Psi_A(\mathbf{K}, \mathbf{R}, \mathbf{r}) = \sum_\alpha C_\alpha(\mathbf{K}) F_{E\alpha}(R) \Phi_\alpha(R; \hat{R}, \mathbf{r}). \tag{2.35}$$

In Eq. (2.35), $C_\alpha(\mathbf{K})$ are scattering amplitudes and will be determined by applying the outgoing wave boundry conditions, and $F_{E\alpha}(R)$ are the energy normalized eigenfunctions. We calculated $F_{E\alpha}(R)$ numerically by solving $(\mathbf{H} - E)\mathbf{F}_E = 0$. Thus, nuclear energy normalized functions $F_{E\alpha}(R)$ and nuclear wave functions are expressed on the same grid and are calculated with the same finite differencing scheme.

Asymptotically, the continuum wave function will have the form of a plane wave for the nuclei times atomic orbitals for the hydrogen atom on one proton ($e^{i\mathbf{K}.\mathbf{R}}|nlm\rangle_A$). Using the partial wave expansion for a plane wave, we can write

$$e^{i\mathbf{K}.\mathbf{R}}|nlm\rangle_A = \frac{1}{KR}\sum_{Lm_L} i^L j_L(KR) Y^*_{Lm_L}(\hat{K}) Y_{Lm_L}(\hat{R})|nlm\rangle_A \tag{2.36}$$

In the above equation, L and m_L are the nuclear orbital angular momentum and its projection along the z-axis, respectively, $j_L(KR)$ are the spherical bessel functions and $|nlm\rangle_A$ are the hydrogen atom basis functions on proton A in the lab-frame. Asymptotically, the $\Psi_A(\mathbf{K},\mathbf{R},\mathbf{r})$ defined in Eq. (2.35) become the $e^{i\mathbf{K}.\mathbf{R}}|nlm\rangle_A$ defined in Eq. (2.36). The angular functions for the nuclei and electron in Eq. (2.35) are the total angular momentum basis in the body frame, but in Eq. (2.36) are the product basis in the lab-frame. We will express the product angular momentum basis in the lab-frame in terms of te total angular momentum basis in the body frame. By doing so, we can easily compare the two continuum wave functions in Eq. (2.35) and Eq. (2.36) to obtain scattering amplitudes $C_\alpha(\mathbf{K})$. Another thing to consider is that the electronic part of the BO molecular basis in Eq. (2.35) [$\phi_\beta(R;\xi,\eta)$ solutions of Eq. (2.3)] are defined in the body frame. However, $|nlm\rangle_A$ are the atomic basis in the lab-frame. So, we will also express the asymptotic body-frame molecular basis in terms of the lab-frame atomic basis.

These two tasks involve the following steps (see App. B for details):

- Combine the product asymptotic nuclear and atomic bases to construct the total orbital angular basis.
- In the molecular basis function (Φ_α defined in Eq. (2.7)), express the body frame molecular orbitals ϕ_β in terms of body-frame atomic orbitals and then express those in terms of lab-frame atomic orbitals.
- Simplify to get molecular basis function in terms of lab-frame total orbital angular momentum basis with $\mathbf{J} = \mathbf{L} + \mathbf{l}$.

- Use this relation to extract $e^{i\mathbf{K}.\mathbf{R}}|nlm\rangle_A$ in terms of $\Phi_\alpha(R;\hat{R},\mathbf{r})$.

These steps lead to Eq. (B.17) giving

$$e^{i\mathbf{K}.\mathbf{R}}|nlm\rangle_A = \frac{1}{KR}\sum_{Lm_L} i^L Y^*_{Lm_L}(\hat{K}) j_L(KR) \sum_{J\Pi\Lambda} (-)^{M+\Lambda}\sqrt{\frac{2L+1}{2J+1}}\langle Ll0\Lambda|J\Lambda\rangle\langle Llm_Lm|JM\rangle \\ \times \frac{(1+\Pi(-)^{L+l+\Lambda})}{\sqrt{2(1+\delta_{\Lambda 0})}}\frac{1}{\sqrt{2}}\{s_{\beta_+}|JM\Pi n\Lambda+\rangle + s_{\beta_-}|JM\Pi n\Lambda-\rangle\}. \tag{2.37}$$

In the above equation, the symbol $\alpha_{+(-)}$ is adopted to express $\{JM\Pi n\Lambda+(-)\}$, respectively. Moreover, in Eq. (2.37) $s_{\beta_{+(-)}}$[4] is the overall phase factor that appear in the relation between the molecular and atomic orbitals asymptotically (see Eq. (B.7)). In $s_{\beta_{+(-)}}$, $\beta_{+(-)}$ corresponds to $n,\Lambda,+(-)$.

For this half collision problem, the scattering solution is a linear combination of outgoing plane waves and incoming spherical waves as defined in Eq. (B.20). Scattering amplitudes for each molecular channel α are obtained by comparing the coefficients of e^{iKR}/R from the asymptotic behavior of $F_{E\alpha}(R)$ and from the scattering wave function. Finally, the continuum wave function satisfying the appropriate boundary condition is ($|\mathbf{K},nlm\rangle_A \equiv \Psi_A(\mathbf{K},\mathbf{R},\mathbf{r})$)

$$|\mathbf{K},nlm\rangle_A \xrightarrow[R\to\infty]{} \sum_{Lm_LJ\pi\Lambda} e^{i\frac{\kappa\pi}{2}} Y^*_{Lm_L}(\hat{K})(-)^{M+\Lambda}\sqrt{\frac{2L+1}{2J+1}} \\ \times \langle Ll0\Lambda|J\Lambda\rangle\langle Llm_Lm|LM\rangle\frac{(1+\Pi(-)^{L+l+\Lambda})}{\sqrt{2(1+\delta_{\Lambda 0})}} \\ \times \frac{1}{\sqrt{2}}\left\{ s_{\alpha_+}e^{-i\delta_{E\alpha_+}}|E\alpha_+\rangle + s_{\alpha_-}e^{-i\delta_{E\alpha_-}}|E\alpha_-\rangle \right\} \tag{2.38}$$

In the above equation, $\delta_{\alpha_{+(-)}}(E)$ is the scattering phase shift for each channel $\alpha_+(-)$, and κ satisfies the relation,

$$\kappa(\kappa+1) = \zeta^2. \tag{2.39}$$

[4] $\beta = \{n,\Lambda,\sigma_z\}$ the good quantum number for the solutions of adiabatic Hamiltonian in Eq. (2.3).

In Eq. (2.39), ζ^2 collectively represents the coefficient of the effective potential in Eq. (2.9) falling by $1/R^2$. It is a subtle point. For all n manifolds, $\kappa(\kappa+1) = J(J+1) - \Lambda^2$, with $\Lambda = n-1$. For all other channels, κ will be determined from $J(J+1)-\Lambda^2$ and BO potentials $U_{n\Lambda\sigma_z}(R)$, which will have a nonvanishing part falling by $1/R^2$. This can be explained from the fact that the $\phi_{n\Lambda\sigma_z}(R;\xi,\eta)$ are Stark states asymptotically with nonzero dipole coupling for each $n\Lambda$.

Since we are dealing with a homonuclear molecule, the above states need also to be properly symmetrized with respect to exchange of nuclei (previously distinctively labeled as A and B). Although nuclear spin has never showed up in the above derivation, implicitly a fixed value for the nuclear spin has been chosen depending on the initial state and kept fixed, as it will not change after applying the laser electric field. Our molecular basis Φ_α defined in Eq. (2.7) has been properly symmetrized with respect to nuclear exchange and follows

$$\hat{P}_{12}\Phi_\alpha(R;\hat{R};\mathbf{r}) = \Pi\sigma_z(-)^\Lambda\Phi_\alpha(R;\hat{R};\mathbf{r}) \tag{2.40}$$

So[5], symmetrizing would lead to the following continuum state:

$$|\mathbf{K},nlm\rangle_A^\pm \xrightarrow[R\to\infty]{} \frac{1}{\sqrt{2}}\left[|\mathbf{K},nlm\rangle_A \pm \hat{P}_{12}|\mathbf{K},nlm\rangle_A\right], \tag{2.41}$$

where $+(-)$ correspond to singlet and triplet spin states of the nuclei, respectively. The procedure to properly symmetrize the continuum wave function for H_2^+ was previously discussed in Refs. [90, 91]. If symmetrization is not done, that would be an inaccurate treatment of the problem and would only give half of the total dissociation probability [73]. The momentum distribution is obtained by projecting $|\mathbf{K},nlm\rangle_A^\pm$ onto the final wave function and taking the modulus squared.

Let us see the simplification of Eq. (2.41) for a given initial state and also assume that we have only the two lowest electronic channels of H_2^+. In our notation, this means that for the initial state $\alpha_i = \{+0010+\}$, the system can only dissociate either in $\{\Pi 0J10+\}$ $(1s\sigma_g)$

[5]Reminder $\alpha = \{JM\Pi n\Lambda\sigma_z\}$.

or $\{\Pi 0 J 1 0-\}$ $(2p\sigma_u)$ states. This choice restricts the allowed parity (Π), which is now given by $(-1)^J$. Also note that for an initial even J, only even Js can get populated in $1s\sigma_g$ and odd Js in $2p\sigma_u$ and vice versa. This means that for this particular case, Π is positive for $1s\sigma_g$ and negative for the $2p\sigma_u$ channel. Consider these simplifications in Eq. (2.38), $l = m = m_L = M = 0$, $n = 1$, $J = L$, $\kappa = L$, and $\alpha_{+(-)} = L + (L-)$, as all other quantum numbers (Π, M, Λ, and n) are fixed, to obtain

$$|\mathbf{K}, nlm\rangle_A \xrightarrow[R\to\infty]{} \sum_L i^L Y^*_{Lm_L}(\hat{K}) \frac{1}{\sqrt{2}} (s_+ e^{i\delta_{EL+}} |EL+\rangle + s_- e^{i\delta_{EL-}} |EL-\rangle). \tag{2.42}$$

For this case $\beta_{+(-)} = \{1, 0, +(-)\}$, and we use $s_{+(-)} \equiv s_{10+(-)}$ for simplicity. Using Eq. (2.40),

$$\hat{P}_{12}|\mathbf{K}, nlm\rangle_A \xrightarrow[R\to\infty]{} \sum_L (i)^L Y^*_{Lm_L}(\hat{K}) \frac{(-1)^L}{\sqrt{2}} \left(s_+ e^{i\delta_{EL+}} |EL+\rangle - s_- e^{i\delta_{EL-}} |EL-\rangle\right). \tag{2.43}$$

The above state is $|-\mathbf{K}, nlm\rangle_B$, i.e. the electron localized on B and A moving towards the $\mathbf{K}$ direction. Since initial $J = 0$ corresponds to the singlet spin state, finally

$$\begin{aligned} |\mathbf{K}, nlm\rangle^+_A \xrightarrow[R\to\infty]{} \frac{1}{2} \Bigg[\sum_L i^L Y^*_{Lm_L}(\hat{K}) \\ \times \left\{ s_+ e^{i\delta_{EL+}} |EL+\rangle (1 + (-)^L) + s_- e^{i\delta_{EL-}} |EL-\rangle (1 - (-)^L) \right\} \Bigg]. \end{aligned} \tag{2.44}$$

For the first(second) term in $\{\}$-brackets, only even(odd) L's are populated. This lets us write the following simple two-term expression,

$$\begin{aligned} |\mathbf{K}, nlm\rangle^+_A \xrightarrow[R\to\infty]{} s_+ \sum_{L \text{ even}} i^L Y^*_{Lm_L}(\hat{K}) e^{i\delta_{EL+}} |EL+\rangle + \\ s_- \sum_{L \text{ odd}} i^L Y^*_{Lm_L}(\hat{K}) e^{i\delta_{EL-}} |EL-\rangle. \end{aligned} \tag{2.45}$$

In the above expression, $|EL+\rangle$ and $|EL-\rangle$ are simply the energy normalized continuum states for $1s\sigma_g$ and $2p\sigma_u$, respectively. The total wave function at the conclusion of the pulse will be

$$\Psi(\mathbf{R}, \mathbf{r}, t_f) = \sum_{J \text{ even}} |F_{J+}(R, t_f)\rangle |J+\rangle + \sum_{J \text{ Odd}} |F_{J-}(R, t_f)\rangle |J-\rangle. \tag{2.46}$$

The differential probability density per unit energy per unit angle $\rho(E,\theta_K)$ (θ_K is angle between $\mathbf{K}$ and the laser polarization direction) is

$$\rho(E,\theta_K) \equiv \frac{\partial^2 P}{\partial\theta_K \partial E} = |{}^+_A\langle \mathbf{K}, nlm|\Psi(\mathbf{R},\mathbf{r},t_f)\rangle|^2. \tag{2.47}$$

$$= \Big| s_+ \sum_{L \text{ even}} (-i)^L Y_{Lm_L}(\hat{K}) e^{-i\delta_{EL+}} \langle EL + |F_{L+}(R,t_f)\rangle + s_- \sum_{L \text{ odd}} (-i)^L Y_{Lm_L}(\hat{K}) e^{-i\delta_{EL-}} \langle EL - |F_{L-}(R,t_f)\rangle \Big|^2. \tag{2.48}$$

In the above expression, ${}^+_A\langle \mathbf{K}, nlm|\Psi(\mathbf{R},\mathbf{r},t_f)\rangle|^2$ is equal to the energy distribution because we used energy normalized scattering states to define $|\mathbf{K}, nlm\rangle^+_A$. So, the momentum distribution $\rho(\mathbf{K})$ (integrated over ϕ_K) is related to $\rho(E,\theta_K)$ by

$$\rho(\mathbf{K}) = \rho(E,\theta_K)\frac{dE}{dK} = \rho(E,\theta_K)\sqrt{\frac{2E}{\mu}}. \tag{2.49}$$

The energy, or KER distribution (dP/dE) would then simply be, defining $a_{L+(-)}(E) = \langle EL + (-)|F_{L+(-)}(R,t_f)\rangle$,

$$\frac{dP}{dE} = \int \rho(E,\theta_K)\sin\theta_K d\theta_K = \sum_{L \text{ even}} |a_{L+}(E)|^2 + \sum_{L \text{ odd}} |a_{L-}(E)|^2, \tag{2.50}$$

the incoherent sum of the contributions from $1s\sigma_g$ and $2p\sigma_u$, respectively. The orthogonality property of spherical harmonics makes the contribution of two channels incoherent in KER distribution. The angular distribution $dP/d\theta_K$ is

$$\frac{dP}{d\theta_K} = \int \rho(E,\theta_K) dE. \tag{2.51}$$

The angular distribution does not get simplified much and would be the coherent sum of the two molecular channels. When two channels do not contribute to the same energy, $dP/d\theta_K$ can be written as an incoherent sum of $1s\sigma_g$ and $2p\sigma_u$ to a good approximation. Note that the total dissociation probability is equal to $\int \rho(E,\theta_K)\sin\theta_K d\theta_K dE$.

2.4 Description of the laser field

For all calculations in this dissertation, we used a Gaussian laser pulse of the form

$$\mathcal{E}(t) = \mathcal{E}_0 e^{-\frac{t^2}{\tau^2}} \cos(\omega t + \varphi), \tag{2.52}$$

where τ is related to the full width of the pulse at the half maximum of intensity (FWHM) as $\tau = \tau_{\text{FWHM}}/\sqrt{2\ln 2}$. The peak electric field in atomic units is $\mathcal{E}_0 = \sqrt{I/3.5 \times 10^{16}\ \text{W/cm}^2}$, with I the peak intensity in W/cm^2. The electric field is linearly polarized along the z-axis, and φ, the carrier-envelope phase, is taken to be zero unless otherwise specified. Finally, the carrier frequency ω is also chosen in almost all cases to correspond to the usual Ti:sapphire central wavelength of 785 nm unless otherwise specified. To be exact, propagation time in a Gaussian pulse should be inifinity. We have, however, found that the results converge for an initial time where the intensity of the pulse is 10^8 W/cm^2 and a final time t_f corresponding to a laser intensity of 10^6 W/cm^2.

2.5 Accuracy test: Comparison between TDBOR and TDBORL

As our target method is TDBOR, we wanted to verify that the computer code was, in fact, working correctly, especially since our formulation is a little nonstandard. Checking the TDBOR method was thus the real goal of our coding the TDBORL method, and we performed a series of tests for this purpose that we report here. For these tests, we used a peak intensity of 10^{13} W/cm^2 and a pulse length of 45 fs. The resulting dissociation probabilities are shown in Table 2.2. From the table, we see that the two codes agree very well — the relative difference in no case exceeds 0.2%. Given the very different representations of the rotation in these methods, we find this agreement convincing evidence that the TDBOR formulation and code are correct. We will thus report TDBOR results only in the remainder of this dissertation. There are two reasons for not performing all the calculations using TDBORL. Firstly, TDBOR will be more accurate than TDBORL. The reason is that to

v	TDBOR	TDBORL
6	0.0472	0.0472
7	0.7657	0.7658
8	0.9728	0.9729
9	0.9958	0.9958
10	0.9523	0.9520
11	0.8730	0.8742

Table 2.2 Comparison of total dissociation probabilities including rotation via basis expansion (TDBOR) and direct discretization on a lattice (TDBORL). The pulse parameters were $I = 10^{13}$ W/cm^2, $\tau_{\mathrm{FWHM}} = 45$ fs, and $\lambda = 785$ nm.

perform efficient time-integration in TDBORL, the short-propagator is split into five terms in Eq. (2.19), and the error is proportional to the commutator $[\mathbf{T}_\theta, \mathbf{H}_R]$. No such splitting was required in TDBOR. Secondly, TDBOR is more efficient than TDBORL. Occasionally, we compare results with the aligned model, TDBOA.

2.6 Considerations to improve accuracy and efficiency

Because we are using a generalized finite difference method [85], we can use a non-uniform radial grid to improve efficiency and accuracy. In particular, we use more points at small R to represent both the rapid change of the wave function near the classical turning point and the shorter wavelengths present in the potential well. Figure 2.1(a) shows the actual grid distribution we used[6] At large R, we used a linear grid appropriate for free particles, and slightly more than half of the points lie at $R \lesssim 20$ a.u. We verified for a typical case that this non-uniform grid gives the same answer as a converged calculation with a uniform grid. We also verified that the grid was large enough that reflections from the boundary at R_{max} were negligible and used no absorbing boundaries. We also checked the convergence of the results with respect to the number of partial waves in TDBOR and with respect to the number of θ grid points in TDBORL.

[6]Only recently we found that our grid is not optimal for the problem and a better grid can be obtained by requiring the accuracy of the local wavelength for the highest energy component in the wave function. See App. C for the detail and comparison.

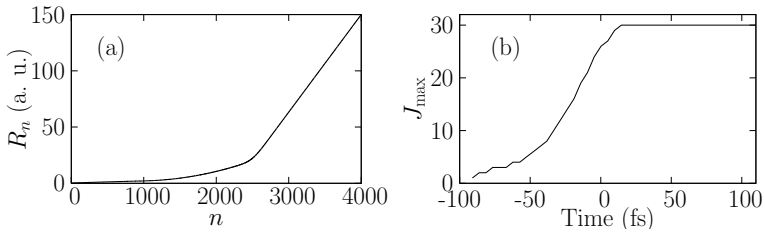

Figure 2.1 (a) The radial grid distribution used in all calculations — only the total number of points varied. (b) The dynamical change in $J_{\max}$ as a function of time for a typical calculation. For this particular case, $v = 9$, $I = 10^{13}$ W/cm^2, $\lambda = 785$ nm, and $\tau_{\text{FWHM}} = 45$ fs. Figure is adapted from Ref. [3].

In addition to the efficiencies afforded by our differencing method, we have built a few other features into our code aimed at efficiency. One of these other features is the ability to determine the necessary number of partial waves dynamically as the code runs. The idea is based on the fact that for roughly the first half of the calculation before the field reaches its maximum, only a small number of Js is required. The code can, therefore, be sped up considerably by including only this small number. Starting with some small $J_{\max}$, we monitor the total probability in the highest partial wave, $\sum_{\alpha'} \int |F_{\alpha' J_{\max}}|^2 dR$. When this probability grows beyond some threshold (10^{-7} in our calculations), we increase $J_{\max}$ for the next time step. We do not, however, allow $J_{\max}$ to decrease when the probability drops back below the threshold. The behavior of $J_{\max}$ for a typical calculation is shown in Fig. 2.1(b). Since the CPU time of our method scales roughly linearly in the number of partial waves, it is clear that this technique speeds the code up by about 25%.

Finally, we used a time step of 0.5 a.u. which is sufficient to give results converged to at least three digits for the slow nuclear dynamics. See App. C for a detailed description of the convergence criteria for different laser parameters with respect to box size, $J_{\max}$, and number of grid points and time step.

2.7 Limits of laser parameters and role of $n = 2$ manifold for 7 and 10 fs pulses

We have performed a systematic study of H_2^+ dissociation by laser pulses of duration 7, 10, 45, and 135 fs using our TDBOR method. There were two reasons for choosing these parameters. Firstly, in our group we had existing results from the TDBOA method for 10, 45, and 135 fs pulses, and we wanted to make a comparison with those results to learn about the limitations of TDBOA. Secondly, these pulses were commonly used in experimental studies and thus we could relate to the experiment. We later performed a systematic study for a 7 fs pulse as this short pulse became more available to perform experiments. For laser peak intensity I, we were limited to 10^{13} W/cm^2 for 45 fs and longer pulses, and we mostly limited the calculations to 10^{14} W/cm^2 for 10 fs and smaller durations. I will list the reasons for these choices:

- The maximum number of partial waves ($J_{\max}$) required to get converged results grows roughly linearly with pulse length (see App. C for details about $J_{\max}$ for different pulses).
- The range of internuclear distances or the box size grows with pulse duration
- The box size and hence the number of radial grid points and $J_{\max}$ also grow with peak intensity
- With an increase in intensity, multiphoton processes become large, and this can lead to a significant transition to highly excited electronic channels of H_2^+. Specifically, at least the $n = 2$ manifold (with p+H($2lm$) dissociation limit) should be included to test the convergence.

Computing technologies have advanced a lot since we started these studies. However, in the beginning it was not even possible to check the convergence of the calculations with respect to highly excited electronic channels for 45 fs and 135 fs pulses because of the

memory constraints and inefficient time propagation. So, we limited our studies to a low intensity of 10^{13} W/cm^2 and performed only two channel calculations for these pulses. Memory requirements and numerical propagation time grow linearly with number of grid points, $J_{\max}$, and number of electronic channels. Including the $n = 2$ manifold makes the calculation size four times bigger as the number of electronic channels becomes eight for initial $M = 0$.

Nevertheless, we included the $n = 2$ manifold and extended our highest peak intensity to 10^{14} W/cm^2 for 7 fs and 10 fs pulses as these pulses required a relatively smaller box size and $J_{\max}$. Here, I should mention again that memory constraints would not allow us to further raise the intensity and also hampered our efforts to get high precision results in the beginning with the $n = 2$ manifold included. We included the $n = 2$ manifold for all the intensities higher than 10^{13} W/cm^2. The convergence criterion with respect to electronic channels was five percent or less total probability in the $n = 2$ manifold. So, we limited the highest peak intensity to 10^{14} W/cm^2 to keep the population in the $n = 2$ manifold small and thus to minimize the population in higher manifolds and also ionization.

While to get converged probabilities in $1s\sigma_g$ and $2p\sigma_u$, it was important to include the $n = 2$ manifold, most of our analysis does not include contribution from these channels, particularly, momentum, energy, and angular distributions of the dissociating fragments (see Sec. 2.3.7 and App. B). I could only derive recently the formulation for the momentum distribution, and it is only implemented for the lowest two electronic channels. We believe the findings in this dissertation would not change as the total probability in these channels is less than five percent for all intensities and pulse lengths.

To elaborate why do include higher electronic channels in the calculations and believe their impact to be smaller in the analysis, the variation in FC-averaged dissociation probability in the $n = 2$ manifold is plotted in Fig. 2.2(d). Figure 2.2 also shows P_{D} in Fig. 2.2(b) and the FC-averaged contribution to P_{D} from $1s\sigma_g$ and $2p\sigma_u$ in Fig. 2.2(c). Thus, we see from Fig. 2.2(d) that the total population in the $n = 2$ manifold is four times smaller at

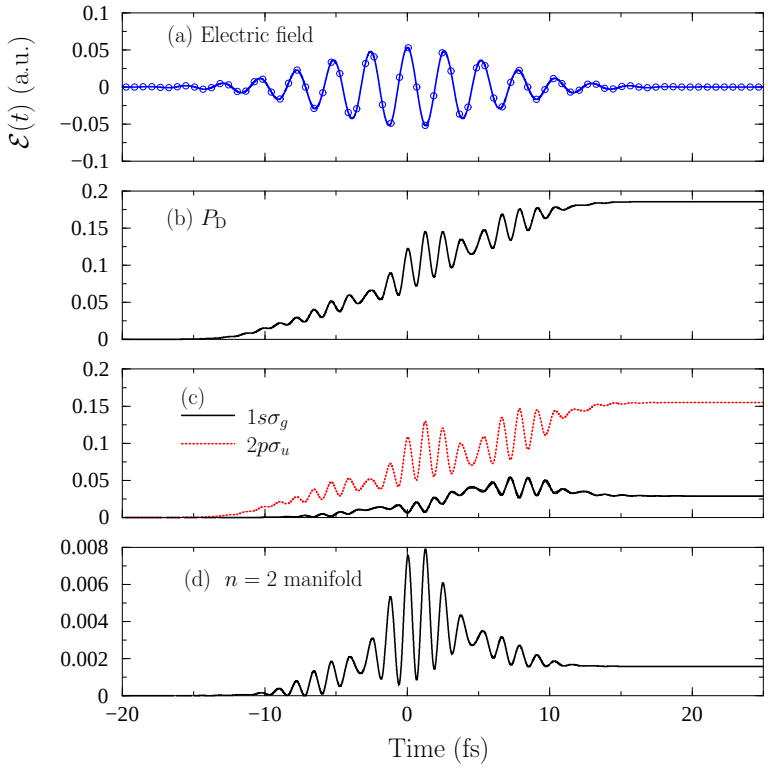

Figure 2.2 Variation wih time in (a) Electric field $\mathcal{E}(t)$; (b) $P_{\rm D}$; (c) FC-averaged dissociation probability from $1s\sigma_g$ (black solid line) and $2p\sigma_u$ (red dotted line); and (d) FC-averaged dissociation probability from $n = 2$ manifold (results from calculations were extracted at points in (a) and then the results were interpolated between points to obtain smooth cures in (b)–(d).); Laser parameters are $\tau_{\rm FWHM} = 10$ fs and $I = 10^{14}$ W/cm^2.

the end of the pulse compared to its maximum value during the time propagation. See Table C.2 for the final and maximum $n = 2$ manifold contribution at any time in the individual vibrational states. Since the peak intensity in Fig. 2.2 is the highest for most of the calculations, the $n = 2$ manifold is lower than the one shown in Fig. 2.2(d) for all the lower intensities.

2.8 Extension of the study to higher J's, higher M's and pulses with elliptical polarization

In all the studies, we use an initial $J = 0$ which corresponds to the singlet nuclear spin state in H_2^+. In Boltzmann's distribution, however, it is $J = 1$ which gets the highest

probability, as the degeneracy for $J = 1$ is 9 (it is 1 for $J = 0$). For room temperature, $J = 0$ accounts for only seven percent of the total probability, while $J = 1$ has the biggest contribution at 46 percent, and $J = 2$ and $J = 3$ have 14 and 25 percent contributions, respectively. So, for future studies, it would be preferable to either perform the calculations using the most probable initial orbital angular momentum state or do the thermal averaging. For a special case of a 10 fs laser pulse and fixed laser intensity, we compared thermal averaged momentum, KER, and angular distributions to those of $J = 0$ for temperatures ranging from 200 K to 600 K. The results are not presented in the dissertation, however, for this temperature range, since our preliminary results show that thermal averaging does not change our conclusions about these distributions. These findings are encouraging but surprising and we will do more investigation into the behavior of other initial rotational states and how these average to give results similar to $J = 0$. Post-pulse dynamics of FC-averaged $\langle \cos^2 \theta \rangle$ indeed change after thermal averaging, and I will discuss it briefly in Chap. 5.

Since, we have developed the method to include nuclear rotation,so the dipole matrix elements have been implemented for a generalized initial rotational state. One further step would be to allow transitions between different M states to study the interaction of H_2^+ with elliptical polarization. There are many interesting questions and also approximations which need answers and validation. I believe the current general structure of our theoretical formulation would allow the complete generalization of the method to perform full dimensional calculations for H_2^+ dissociation in elliptically polarized light.

Chapter 3

Dissociation probability

3.1 Introduction

In this chapter, we revisit the validity of the aligned molecule approximation for 10, 45, and 135 fs FWHM, 800 nm laser pulses by comparing the total dissociation probability calculated with and without nuclear rotation. The agreement, it turns out, is at best qualitative. Vibrational trapping (VT), for instance, appears quite differently in the two approximations. Physically, the picture often used to explain this phenomenon is the adiabatic Floquet representation [20]. Figure 3.1 shows both the diabatic and adiabatic Floquet Born-Oppenheimer potential curves for H_2^+. Vibrational trapping (or one-photon trapping) is said to occur when part of the vibrational wave function becomes trapped in the field-dressed adiabatic potential well (labeled "VT" in the figure) above the one-photon crossing. Similarly, three-photon trapping is trapping of the wave function in the field-dressed adiabatic potential well above the three-photon crossing.

Both one-photon and three-photon trapping have been discussed in previous studies [20, 30, 33]. These phenomena were seen to result in higher survival probabilities — also called "stabilization" — as a function of the peak laser intensity in aligned molecule calculations using laser pulses 100 fs or longer [30]. Already 15 years ago, it was found, however, that nuclear rotation destroys three-photon trapping and suppresses one-photon trapping, at least for the case of an initial state with high angular momentum [33]. This conclusion was

based on the fact that nuclear rotation eliminates the intensity-dependent stabilization for vibrational states lying just above the three-photon crossing, but not for those lying above the one-photon crossing [30, 33].

In the present study, we focus on one-photon trapping, which, for simplicity, we will call vibrational trapping (VT). Our results show that nuclear rotation eliminates the intensity-dependent stabilization for a zero angular momentum initial state. Studying the dynamics of the probability density, however, we have found that the presence or absence of intensity-dependent stabilization is not sufficient to answer the question of whether or not VT is present.

The mechanism of vibrational trapping has also been invoked to explain the higher survival probability of the vibrational states lying above the one-photon crossing compared to the state at the crossing for a given peak intensity [32]. Although these results were from aligned molecule calculations, the authors expected this behavior to persist even if nuclear rotation were included. Our results show that the qualitative behavior of the total dissociation probability (P_{D}) for these higher vibrational states is indeed similar from both the aligned molecule method and the method with nuclear rotation. However, we do not interpret the lower P_{D} of these states compared to the state at the crossing as evidence of vibrational trapping. Rather, we believe it is mostly a result of the fact that the high-lying states are not at the one-photon resonance. A detailed discussion of the behavior of P_{D} as a function of the initial vibrational state and the laser peak intensity will come in Sec. 3.3.

A closely related process to VT, first identified in aligned molecule calculations is known as dynamical dissociation quenching. It refers to the possibility of stabilization but in this case as a function of wavelength and for a coherent initial wave packet [34]. As with vibrational trapping, nuclear rotation makes dynamical dissociation quenching disappear except for particular initial ro-vibrational wave packets [76]. As we do not use a coherent wave packet for the initial state in the present work, however, we will not address the problem of dynamical dissociation quenching.

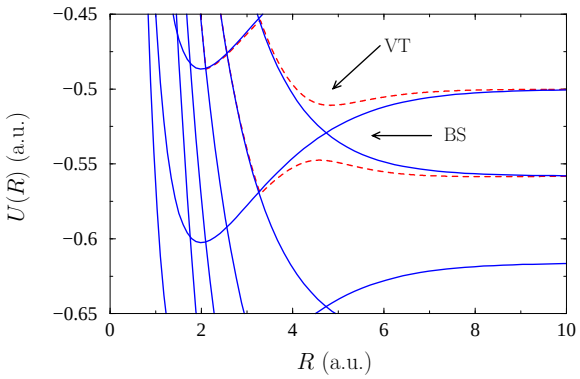

Figure 3.1 Field dressed $1s\sigma_g$ and $2p\sigma_u$ potential curves for H_2^+ aligned along the linearly polarized laser field for $I = 10^{13}$ W/cm^2 and $\lambda = 785$ nm. Solid blue lines show the diabatic curves and dashed red lines show the adiabatic curves near the one photon crossing. BS = bond softening, VT = vibrational trapping (see also Fig. 1.1). Figure is adapted from Ref. [3].

In a recent study [92], a control scheme based on the aligned model has been proposed to control the population of a given v taking advantage of the interplay between dynamical dissociation quenching and VT. Such control schemes are becoming increasingly important, providing further reason to better understand the limitations of the aligned method.

As mentioned in the introduction, our aim is to quantitatively compare P_D from TDBOR and TDBOA. That is, we want to see to what extent the aligned molecule approximation really captures the correct physics based on the physical observable P_D over a wide range of intensities rather than on the final angular distribution of the fragments at a few select intensities as has been a primary justification for this approach. Before making this comparison, we want to see if nuclear rotation has any impact on the dissociation by considering J-distribution and the number of partial waves populated in a calculation in the following section.

3.2 Significance of rotation

We have performed calculations for pulse lengths of 10, 45, and 135 fs. Our study of the intensity dependence for the 10 and 45 fs pulses was much more systematic than for 135 fs, for which results were obtained only at a few intensities. Using the initial state described in

Eq. (2.20), we performed calculations starting from each $J = 0$ bound state v. We chose the highest intensity to be 10^{13} W/cm^2 for 45 and 135 fs pulses and 10^{14} W/cm^2 for 10 fs pulse. This choice ensures minimal ionization of H_2^+ since our method does not include ionization. For 45 and 135 fs, lowest two electronic channels are included in the calculation, however, for 10 fs pulse, electronic states in $n = 2$ manifold are also included for $I > 10^{13}$ W/cm^2 for 3-digits covergence in P_D (see App. C for the details about convergence tests).

Figures 3.2(a) and 3.2(b) show J_{max} as a function of intensity for each v for 45 and 10 fs laser pulses, respectively. The J_{max} plotted in each case is the value at the final time as determined dynamically during the calculation using the technique described in Sec. 2.5. Figure 3.2 shows a monotonic increase in J_{max} with intensity for each v. We take the number of J_{max} required to get converged results to be a measure of the importance of nuclear rotation. The more partial waves required, the more important is nuclear rotation for short pulses like 10 and 45 fs. Moreover, for peak intensities much greater than 10^{13} W/cm^2 — which applies to most experiments — we expect that the effect of rotation should be even more pronounced. Figure 3.2 also shows a clear maximum around $v = 9, 10, 11$. These states lie near the 1ω crossing that leads to 1ω dissociation (see Fig. 3.1 marked as 1ω [15, 20, 21]). Since J must change by one with each photon absorbed or emitted, it is no surprise that states near the 1ω crossing have the largest J_{max}. For 10 fs pulse, Fig. 3.2(b) shows a sharp increase in J_{max} for $v \geq 15$ at intensities higher than 7×10^{13} W/cm^2. This behavior should be investigated as we do not understand this behavior. The largest J_{max} required for 45 fs was 35 and 18 for 10 fs pulse for 10^{13} W/cm^2 peak intensity. If the pulse length is extended to 135 fs at this intensity, however, then J_{max} must be increased to 42 to ensure convergence. This increase indicates that nuclear rotation becomes more important as the pulse length increases as one would expect from the simple fact that more time is available to drive transitions. Moreover, the J_{max} is 47 and therefore, is higher than all above cases, for 10 fs pulse when the peak intensity is increased to 10^{14} W/cm^2.

Further evidence of the importance of nuclear rotation is the fact that the J-distribution

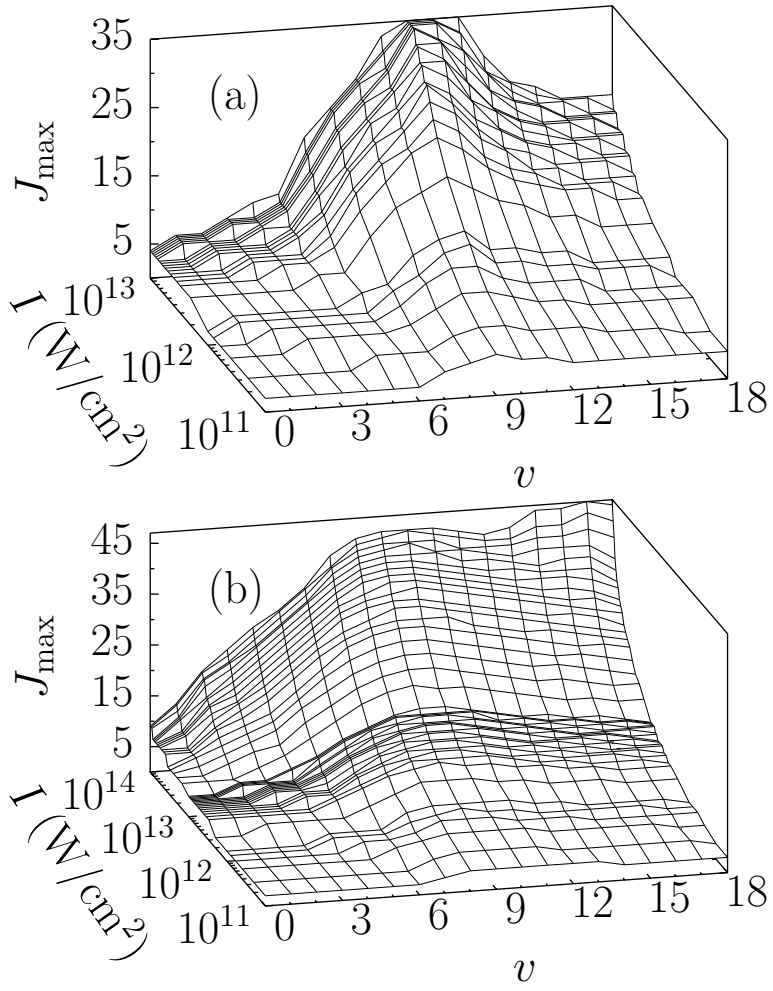

Figure 3.2 (a) $J_{\max}$ as function of laser peak intensity and initial v for $\tau_{\mathrm{FWHM}} = 45$ fs; (b) same as (a) for $\tau_{\mathrm{FWHM}} = 10$ fs.

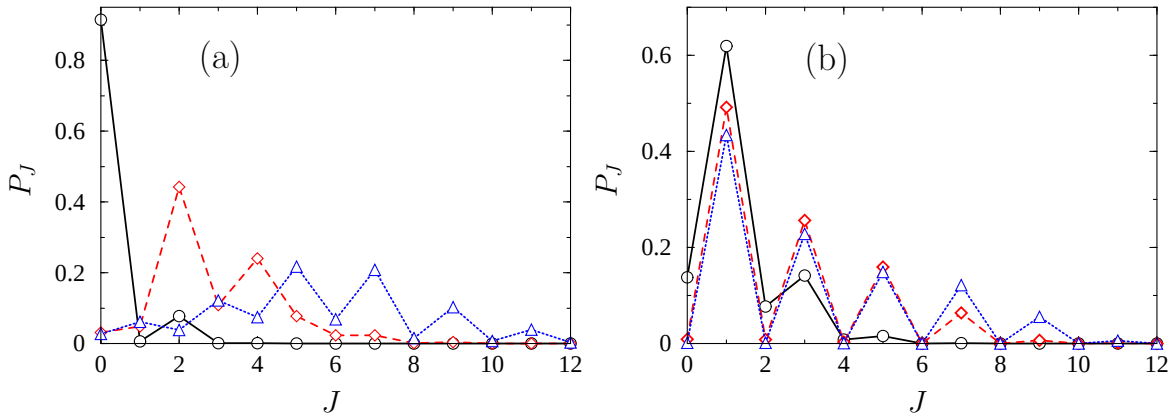

Figure 3.3 Angular momentum distribution for (a) $v = 7$ and (b) $v = 9$. The intensities shown are 10^{12} W/cm^2 (circles), 5×10^{12} W/cm^2 (diamonds), and 10^{13} W/cm^2 (triangles) for $\tau_{\mathrm{FWHM}} = 45$ fs and $\lambda = 785$ nm. Figure is adapted from Ref. [3].

becomes broader with increasing intensity for each v [see Figs. 3.3(a) and 3.3(b)]. For instance, at our highest peak intensity of 10^{13} W/cm^2, 97.26% of the population starting from v=7 and 99.83% starting from v=9 have J higher than zero at the end of the pulse.

So far, we have only discussed how the parameters of the calculations reflect the importance of including rotation. While these do provide important insights, the real test must come from the comparison of physical observables. We thus show in Fig. 3.4 the dissociation probabilities P_{D} calculated using both TDBOR and TDBOA. The calculations share some general qualitative features, but differ both quantitatively and in the qualitative details.

One similarity we find, for instance, is that in both cases the maximum P_{D} occurs when the system is initially in $v = 9$, which stands to reason since it lies closest to the 1ω crossing. The two methods also share the fact that the low vibrational states do not dissociate significantly in this intensity regime and that the high vibrational states $v > 12$ show substantial dissociation but do not saturate. Both calculations also show an interesting decrease in P_{D} for $v = 12$. This feature has been noted before [32], and as we will see below, can mostly be traced to the behavior of the bound-free nuclear dipole transition matrix element (see, for example, the first order perturbation theory results in Fig. 3.5).

While the two methods show some gross similarities, even a cursory examination shows

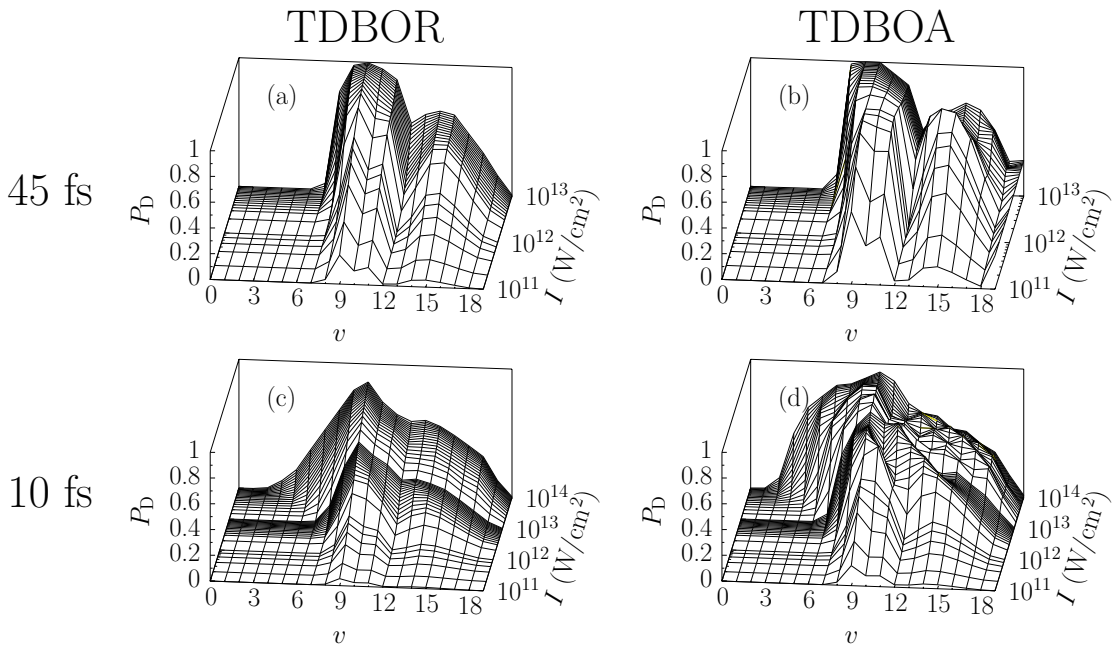

Figure 3.4 Total dissociation probability P_D as function of laser peak intensity (I) and initial v: (a) TDBOR and (b) TDBOA for $\tau_{FWHM} = 45$ fs; (c) same as (a), and (d) same as (b) for $\tau_{FWHM} = 10$ fs.

many differences in the details. For instance, P_D saturates much faster as a function of intensity in the TDBOA compared to the TDBOR for $v = 7, 8$, and 9. The reason might simply be due to geometrical alignment. "Geometrical alignment" refers to the preferential field-induced dissociation or ionization of the molecules initially aligned along the polarization of the field [93]. The reduced dimensionality of the TDBOA forces all of the molecules to be aligned with the field, giving the maximum likelihood of the dominant $1s\sigma_g \rightarrow 2p\sigma_u$ transition. In the case of the TDBOR, however, our initial $J = 0$ state is isotropic so that only a fraction of the initial population is initially aligned with the field. In the TDBOR, however, the field can also torque the molecule into alignment before dissociating it in a process referred to as dynamical alignment [93]. We expect that dynamical alignment will be more important for the 135 fs pulse than for the 45 fs pulse since it is closer to the free rotation period of 556 fs.

Whichever combination of these mechanisms is at work, it is clear that approximating

dissociation as coming only from molecules completely aligned with the laser polarization — as is usually done in the TDBOA — is quantitatively insufficient. The facts that all 10, 45, and 135 fs pulses populate a large number of partial waves for TDBOR and that there are clear differences between the TDBOA and TDBOR P_{D} imply that nuclear rotation is an important effect to include. Evidence that this holds even for qualitative conclusions is given in the next section.

3.3 Effect of rotation on vibrational trapping

Another clear difference between the TDBOR and TDBOA in Fig. 3.4 is the behavior of the high-lying vibrational states, $v > 9$, where vibrational trapping is conventionally understood to play a significant role. For the purpose of this discussion, it is useful to carefully distinguish between the terms vibrational trapping and stabilization. The term vibrational, or population, trapping commonly refers to the trapping of part of the wave function in the potential well above an avoided crossing of the field-dressed adiabatic Floquet potential curves (see Fig. 3.1). Most often, the crossing in question is the one-photon crossing [30, 32], although vibrational trapping above the three-photon crossing has also been studied [32]. In either case, these phenomena have primarily been observed and studied using TDBOA, as has been the similar phenomenon of dynamical dissociation quenching [34].

The term "vibrational trapping" has been applied for higher survival probability of the high-lying vibrational states either as a function of v [32] or as a function of intensity [30]. The term "stabilization" has also been used to describe the higher survival probability in each case [30, 32, 34] in analogy to the suppression of ionization as a function of intensity found previously for atoms [94]. We will use stabilization to describe any case in which the dissociation probability decreases with intensity. Unfortunately, we cannot identify a similarly clean definition of vibrational trapping. We will thus use this term more qualitatively. Clearly the two effects are related, and we regard vibrational trapping to be one mechanism that can give stabilization. It is also possible to have vibrational trapping without stabi-

lization. For instance, the slope of P_{D} with I may only decrease rather than change sign as it would for stabilization.

Figure 3.4 shows the stabilization studied in Ref. [32], namely that P_{D} for $v > 9$ is lower than P_{D} for $v = 9$. In particular, they cited the fact that P_{D} is not unity as evidence for stabilization based, presumably, upon the expectation that these vibrational states should dissociate as readily as $v = 9$. It is not obvious, though, that these states should indeed dissociate so readily since they are not at the one-photon resonance. To gain some insight into this question, recall that the usual explanation of vibrational trapping relies on the adiabatic Floquet potentials of Fig. 3.1. These necessarily include multiphoton transitions. It follows that stabilization must be a multiphoton phenomenon. In other words, it should not appear in a simple first-order perturbation theory calculation. Figure 3.5 shows that P_{D} from such a calculation, however, reproduces this "stabilization" quite well. The perturba-

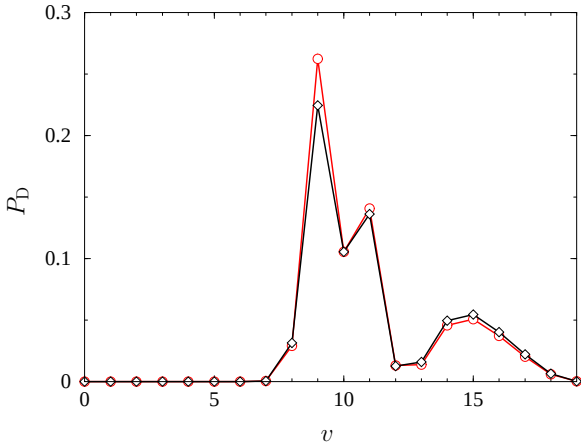

Figure 3.5 Total dissociation probability P_{D} from first order time-dependent perturbation theory (red circles) and from TDBOR (black diamond). The laser parameters are $I = 10^{11}$ W/cm^2, $\lambda = 785$ nm, and $\tau_{\mathrm{FWHM}} = 45$ fs. Figure is adapted from Ref. [3].

tive results were integrated over the same laser pulse as the numerical results and included nuclear rotation. That is, the final nuclear wave function had $J = 1$ to satisfy the dipole selection rules for a transition from the initial $J = 0$ state. The dissociation probability for each v is the result of integrating over all final continuum energies to obtain the total P_{D}.

Figure 3.5 also compares P_D from the full TDBOR calculations, showing good agreement at the perturbative intensity of 10^{11} W/cm^2. Inspecting the first-order results, we find that the overlap between the initial and final vibrational states in the dipole matrix element largely controls the transition probability. We expect this behavior will persist for both TDBOA and TDBOR calculations for different wavelengths and higher intensities until P_D saturates. We conclude that the lower P_D for high v states is thus not a good indicator of vibrational trapping.

The difference in the behavior of P_D for higher vibrational states can be more clearly seen in Fig. 3.6. It is evident from Fig. 3.6(b), for instance, that P_D is lower at $I = 10^{13}$ W/cm^2 for $v = 10$, 11, 14, and 15 than at $I = 10^{12}$ W/cm^2 for TDBOA. This decrease in P_D is precisely the intensity-dependent stabilization discussed in [30]. Examining Fig. 3.6(a), however, we find that P_D does not decrease for any vibrational state with increasing intensity over the range of intensities we have considered.

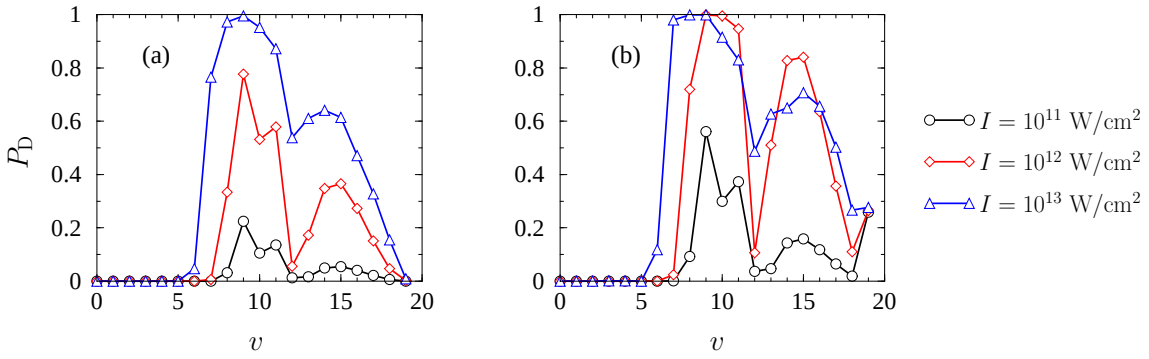

Figure 3.6 Total dissociation probability P_D as a function of initial vibrational state v using (a) TDBOR and (b) TDBOA. The laser parameters are $\lambda = 785$ nm, $\tau_{FWHM} = 45$ fs. Figure is adapted from Ref. [3].

Figure 3.7 gives another cut of Figs. 3.4(a) and 3.4(b) — this time, for a fixed v — and shows the intensity-dependent stabilization discussed in Ref. [30]. In fact, all of the states shown with $v > 9$ clearly show a decrease in P_D with increasing intensity for TDBOA which is the definition of stabilization. None of the TDBOR calculations, however, show any stabilization. The figure also shows that there are not only these qualitative differences

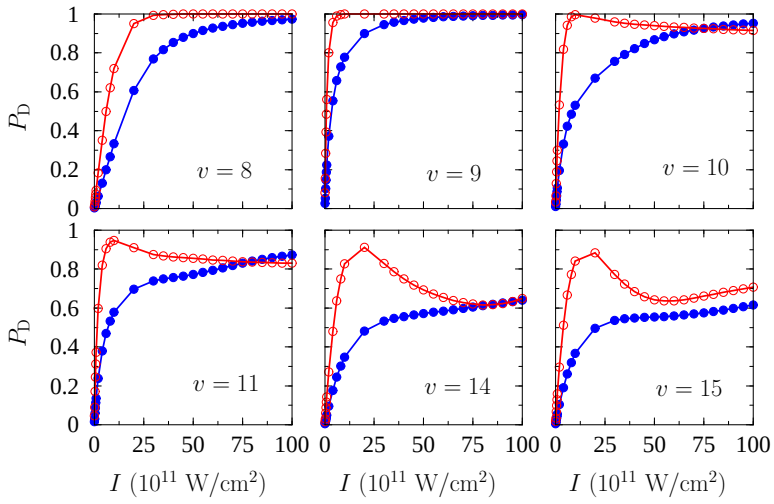

Figure 3.7 Total dissociation probability P_D as a function of the peak laser intensity. The blue curve (filled circles) indicates the results of TDBOR; and the red curve (open circles), the results of TDBOA. The laser pulse parameters are $\tau_{FWHM} = 45$ fs and $\lambda = 785$ nm. Figure is adapted from Ref. [3].

between the two methods, but also quantitative ones. For instance, TDBOA consistently predicts higher dissociation, except for $v = 10$ and 11 above $\approx 8 \times 10^{12}$ W/cm^2 where the TDBOR prediction is larger. Figure 3.7 thus illustrates that comparisons at a single intensity do not tell the whole story. Figure 3.7 also shows that the intensity dependence of P_D is very different for different vibrational states in TDBOA. By comparison, the more complete results including rotation show that, although P_D is not the same for different vibrational states, its dependence on peak intensity behaves in a similar way for all vibrational states over the range of intensities we have studied. From these results, we conclude that intensity-dependent stabilization of H_2^+ initially in $J = 0$ does not occur in an intense laser pulse for the vibrational states lying above the one photon crossing of field-dressed potentials. Previous studies [30, 33], when started from an initial state with higher angular momentum, however, have suggested that one-photon stabilization may persist even after including the nuclear rotation.

For comparison, we show in Fig. 3.8 the results for a pulse with τ_{FWHM}=135 fs. The figure shows the results for vibrational states with significant P_D lying above the one-photon

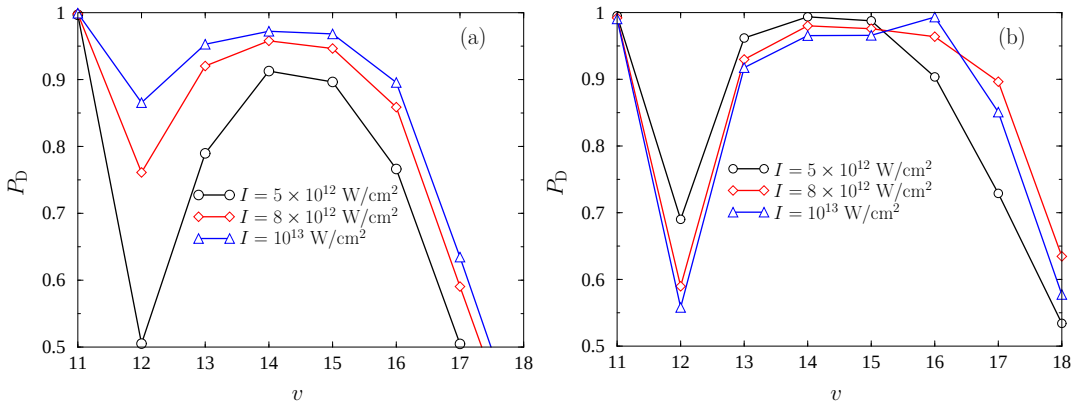

Figure 3.8 Total dissociation probability P_D as a function of initial vibrational state v using (a) TDBOR and (b) TDBOA. The laser parameters are $\lambda = 785$ nm, $\tau_{FWHM} = 135$ fs. Figure is adapted from Ref. [3].

crossing between $1s\sigma_g$ and $2p\sigma_u$. It is clear from the figure that the trends discussed above for a 45 fs pulse hold also for the 135 fs pulse. In particular, we emphasize that TDBOA shows stabilization while TDBOR still does not.

An alternative way to uncover the presence of VT is to study the dynamics of the wave function during the pulse [20]. Figures 3.9(c) and 3.9(d), calculated with the TDBOA, show a clear localization of the wave function in the adiabatic potential well (marked as VT in Fig. 3.1) during the peak of the pulse near $t = 0$. This trapping of the wave function is, of course, what is meant by VT [20, 30, 32, 33]. In Figs. 3.9(a) and (b), however, we see that VT is much weaker, but not entirely absent, when the molecule is allowed to rotate — even though the total dissociation probability shows no intensity-dependent stabilization. This discussion illustrates that vibrational trapping and stabilization are different, but related, phenomena given our definition of stabilization. It also illustrates the difficulty in trying to quantitatively define vibrational trapping. Nevertheless, we conclude from above discussion that the effect of nuclear rotation for a 45 fs pulse is sufficient to eliminate the intensity-dependent stabilization that is present in TDBOA.

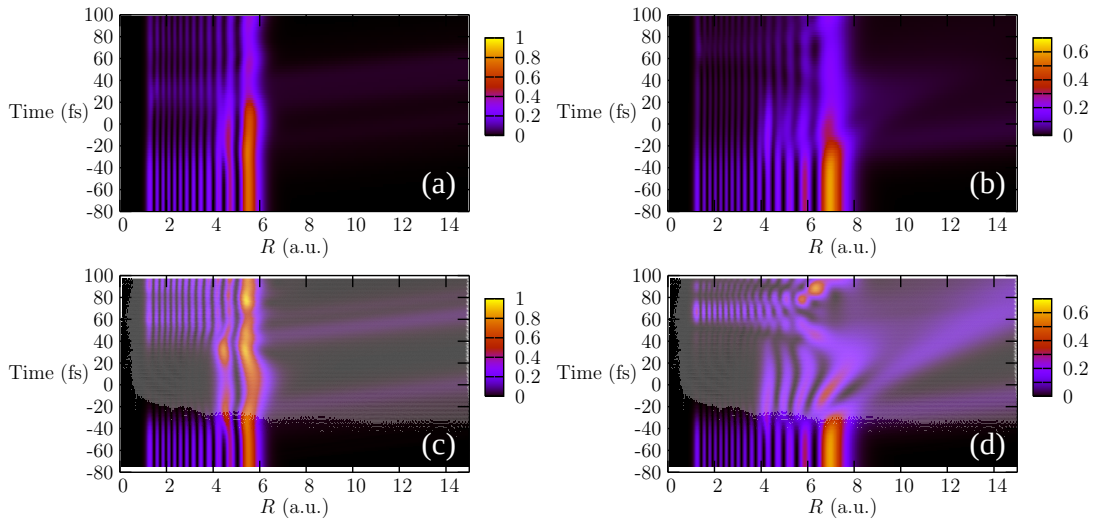

Figure 3.9 Projection of the probability density onto R as a function of time from TDBOR for (a) $v = 12$ and (b) $v = 15$. (c) and (d) show the probability density from TDBOA for $v = 12$ and $v = 15$, respectively. The laser parameters in this case are $\tau_{\mathrm{FWHM}} = 45$ fs, $\lambda = 785$ nm, and I$= 10^{13}$ W/cm^2. Figure is adapted from Ref. [3].

3.4 Curious behavior of $v = 12$

Dissociation probability for $v = 12$ shows "suppression" compared to adjacent vibrational states for all the pulse lengths and peak intensities presented in this chapter. As stated earlier, based on 1st-order perturbation theory results, dipole matrix elemnets for $v = 12$ would be responsible for this suppression. To understand how the dipole matrix elements[1] cause a suppression in H_2^+, we plot the square of their amplitude, $|\mathcal{D}_v(E)|^2$, for each vibrational state v as a function of the dissociation kinetic energy release (KER) in Fig. 3.10(b). The dipole matrix elements can be written as $\mathcal{D}_v(E)=\langle F_E^{\alpha\prime}|D_{\alpha\,\alpha\prime}|F_v^{\alpha}\rangle$, where F are the nuclear wavefunctions as a function of internuclear distance; E is the energy of the final continuum state (KER=E+13.6 eV); v, the initial vibrational state; α and $\alpha\prime$[2] defined in Sec. 2.2.1, the initial ($1s\sigma_g$) and final ($2p\sigma_u$) electronic states; and $D_{\alpha\,\alpha\prime}(R) = \langle\Phi_{\alpha\prime}(R)|z|\Phi_{\alpha}(R)\rangle\sim R/2$,

[1] This is bound-free dipole coupling between initial vibrational state in $1s\sigma_g$ and continuum states in $2p\sigma_u$.

[2] To remind α represents the set of all quantum number $\alpha = \{JM\Pi n\Lambda\sigma_z\}$.

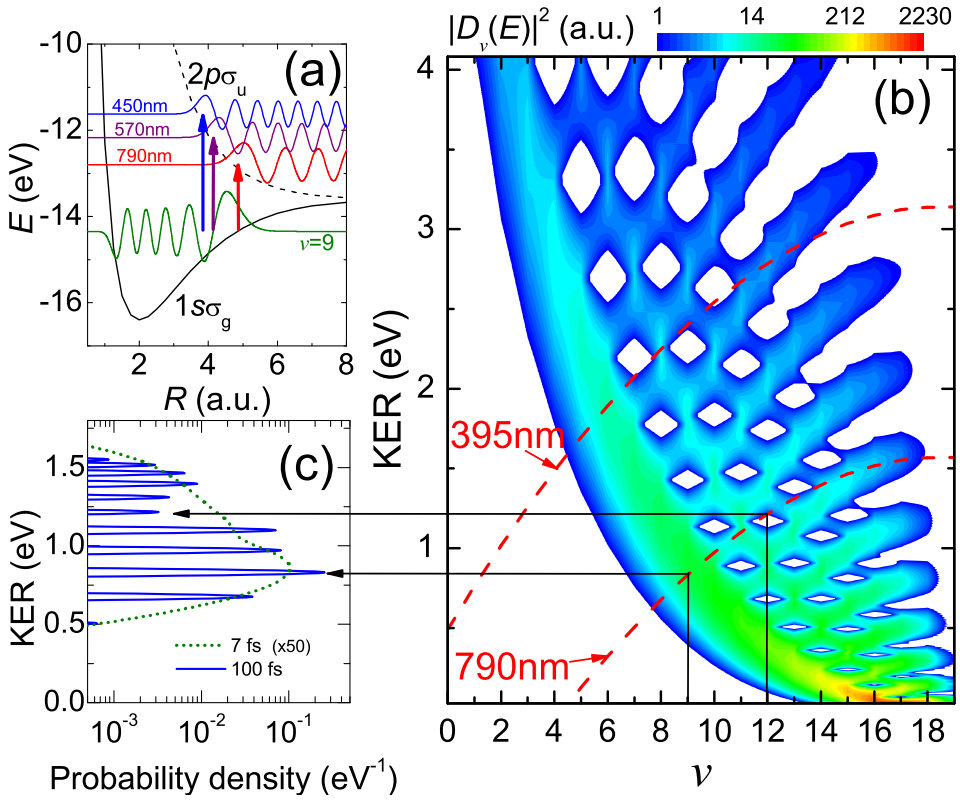

Figure 3.10 (a) H_2^+ potentials and wavefunctions, see text. (b) Square of the amplitude of the H_2^+ dipole matrix elements ($|\mathcal{D}_v(E)|^2$) as a function of v and KER. Curves shown for 790 nm and 395 nm are defined by KER=$E_v+\hbar\omega$+13.6 eV. (c) H_2^+ dissociation probability density using perturbation theory (4×10^{10} W/cm^2) for 7 fs and 100 fs, 790 nm pulses, after Franck-Condon averaging. Figure is adopted from Ref. [12].

where Φ is the Born-Oppenheimer electronic basis defined in Eq. (2.7)[3]. In this case, $\alpha = \{0, 0, +1, 1, 0, +1\}$ and it couples to $\alpha\prime = \{1, 0, -1, 1, 0, -1\}$. The structured dips in $|\mathcal{D}_v(E)|^2$ in Fig. 3.10(b) result from poor overlap of the continuum wavefunction with the bound wavefunction as a function of ω, as pictorially shown for v=9 in Fig. 3.10(a) — the overlap is better for 790 and 450 nm than for 570 nm. Comparison with Fig. 3.10(b) shows that for v=9 the dipole matrix element is maximal at about 790 nm and oscillates under a decaying envelope with decreasing wavelength. The dips cause the dissociation suppression that we observe.

[3]For explicit expression of dipole coupling, see Eq. (A.3).

The dissociation probability P_D from first-order time-dependent perturbation theory is related to the dipole matrix elements by $P_D = \int \frac{dP}{dE} dE$, where in the rotating wave approximation (in atomic units)

$$\frac{dP_v}{dE} = \pi \frac{2\ln 2}{(\Delta\omega)^2} I |\mathcal{D}_v(E)|^2 \exp\left[-\left(\frac{2\sqrt{\ln 2}(\omega - \omega_{fi})}{\Delta\omega} \right)^2 \right]. \tag{3.1}$$

In this expression, I is the laser peak intensity, $\omega_{fi} = E - E_v$, and $\Delta\omega = 4\ln 2/\tau_{\mathrm{FWHM}}$ is the laser bandwidth for the Gaussian pulse. Thus, the choice of ω acts as a filter on $\mathcal{D}_v(E)$ as demonstrated in Fig. 3.10(b) for 395 and 790 nm.

From Fig. 3.10(b) we can make several predictions. For example, at 790 nm we expect P_D to be suppressed for v=12 and 13 due to the minima in $|\mathcal{D}_v(E)|^2$. Similarly, at 395 nm we expect suppression for v=7, 9, and 10. The laser bandwidth (pulse duration) determines the width of the frequency filter, hence, for very short pulses ($\lesssim$10 fs) we expect the vibrational peaks to merge in KER and smear to reduce the suppression while for long pulses ($\gtrsim$100 fs) the suppressions will be well-defined.

Using Eq. (3.1) and $|\mathcal{D}_v(E)|^2$ from Fig. 3.10(b), we check these predictions by plotting the KER spectrum from perturbation theory for 100 fs and 7 fs, 790 nm pulses in Fig. 3.10(c). The expected dips in probability for v=12 and 13 are visible, reducing in contrast from 100 fs to 7 fs. For higher peak intensities, signature of the vibrational suppression in KER-distribution from theoretical results and its experimental evidence will be presented in a later chapter (see Sec. 6.6.4)

3.5 Concluding remarks

We have performed calculations for the dissociation of H_2^+ in an intense laser pulse using two schemes: TDBOR and TDBOA, including and excluding nuclear rotation, respectively. The calculations systematically covered the intensity range 10^{10} W/cm^2 to 10^{14} W/cm^2 for all possible $J = 0$ initial vibrational states in 10 fs pulse, and 10^{10} W/cm^2 to 10^{13} W/cm^2 in a 45 fs laser pulse. Even though 45 fs pulse is roughly twelve times shorter than the

free rotation period, we found that rotation still plays an important role as judged by its impact on the total dissociation probability. Our study was more compreensive for 45 fs pulse, however, the brief discussion of 10 fs indicates nuclear rotation significantly change the behavior of dissociation probability for this pulse as well. We also found that including rotation completely inhibited intensity-dependent stabilization for laser parameters that the aligned molecule approximation predicted strong suppression of the dissociation probability for all 10, 45, and 135 fs pulses. It is important to note, however, that our initial state had $J = 0$. Other calculations that have started from higher J have reported that stabilization persists, although still weaker than for the aligned molecule calculation. Our results may thus be more applicable to experiments on H_2^+ beam targets than to experiments starting from H_2 targets. In the former, the molecules are expected to be in a roughly Boltzmann rotational distribution. In the latter, H_2^+ only appears in the laser pulse after H_2 is ionized, which might give more weight to higher J states. In any case, any control scheme based on these phenomena should therefore be careful to consider the effects of rotation. As discussed in Sec. 2.8, for the room temperature, $J = 0$ account for only seven percent of the total probability in Boltzmann distribution and $J = 1$ gets the highest weight. Our preliminary results for thermal averaging show that the findings presented here would not change, for initial $J = 1$ after averaging over initial $M = 0, \pm 1$.

Finally, this work has shown that intensity-dependent stabilization and vibrational trapping are not the same. While the former can be given a quantitative definition, the decrease in dissociation probability with increasing intensity, the latter is more difficult to give a similarly quantitative definition. In the aligned molecule calculation, one reasonable approach would be to project the wave function onto the adiabatic Floquet basis and extract the portion corresponding to the well above the one-photon crossing. Unfortunately, this approach is not so straightforward for the calculations including rotation as the corresponding adiabatic Floquet potentials are extremely complicated. So, while vibrational trapping is easy to identify qualitatively, for any discussion of vibrational trapping beyond this it seems

necessary to develop a quantitative definition.

Chapter 4

Rotational dynamics of dissociating H_2^+

4.1 Introduction

Here, we examine the dynamics of the angular distribution of H_2^+ dissociating to p+H using our fully quantum mechanical approach described in Sec. 2.2.1 and has previously appear in [3]. In particular, we study the relative importance of dynamic and geometric alignment as a function of the pulse length. Dynamic alignment is the process in which the laser's electric field torques the molecules into alignment along the laser polarization direction before dissociating or ionizing them [21]. Being a light molecule, H_2^+ undergoes greater dynamic alignment than, for instance, I_2 in the same laser pulse [21]. Dynamically aligned dissociating fragments exhibit a narrow angular distribution along the polarization direction [20]. At the opposite end of the dynamical spectrum, geometric alignment refers to the preferential dissociation or ionization of the molecules aligned with the laser polarization. Thus, geometric alignment implies the lack of angular dynamics.

Both dynamic and geometric alignment occur during the laser pulse. The physical observable in experiments, however, is the angular distribution at the detector — in other words, at infinite times[1]. When interpreting their findings, experimentalists often assume these infinite-time angular distributions are the same as at the moment that the molecule

[1]The work in this chapter has appeared in our previous publication [5].

breaks, neglecting any post-pulse rotation of the recoiling fragments [95, 96]. The experimental data analysis does not typically rely on this "axial recoil approximation" as it is only an interpretive assumption. Nevertheless, this assumption has shaped many people's physical picture of the dynamics of diatomic molecules in intense laser pulses.

Since, it does not appear to be a straightforward proposition to experimentally measure post-pulse alignment, even using pump-probe techniques, we must study it theoretically. Thus, another of our goals for this chapter is to check the validity of the axial recoil approximation. While its validity has been addressed in previous studies using a classical model [97] and using a semi-classical model combined with rigid rotor quantum mechanical calculations [98–100], a fully quantum mechanical examination has not previously been undertaken.

To address our goals, we performed a comprehensive study of the dynamics of the angular distribution of H_2^+ dissociating in an intense laser pulse for peak intensities from 10^{10} W/cm^2 to 10^{14} W/cm^2. and pulse lengths ranging from 135 fs to 5 fs. Although all of the pulses in this range are very short compared to the free rotational period of H_2^+ (≈ 556 fs), the angular dynamics both during and after the pulse changes character significantly. We illustrate the importance of nuclear rotation in all cases by comparing the results of our calculations with and without nuclear rotation. We conclude, perhaps surprisingly, that even for pulses as short as 5 fs it is important to include nuclear rotation in order to obtain accurate angular distributions.

4.2 Dynamics during the pulse

As mentioned in Sec. 4.1, the dynamics of the angular distribution is generally described by the limits: geometric and dynamic alignment. Defining these phenomena quantitatively within the TDBOR (or experimentally) is not a simple task. Fortunately, comparing the TDBOA and TDBOR results for the total dissociation probability P_{D} has proven to be a useful way to quantify dynamic alignment (see Secs. 2.2.1 and 2.2.2 for details of the

methods). This usefulness follows from the fact that the molecule is not allowed to rotate in TDBOA and thus displays purely geometric alignment. The magnitude of the dynamic alignment is thus given by the difference in P_{D} between the two calculations. Care must be taken when performing this comparison, however, to ensure that the initial angular distribution in the two methods match.

The TDBOR results presented here start from the J=0 state, where J is the total orbital angular momentum. To mimic this initial angular distribution, the TDBOA results must be averaged over the initial angle θ between the internuclear axis and the laser polarization as follows:

$$\bar{P}_{\mathrm{D}}(I) = \frac{\int_0^{\pi} P_{\mathrm{D}}(I,\theta)\sin\theta d\theta}{\int_0^{\pi}\sin\theta d\theta}, \tag{4.1}$$

where I is peak intensity. Since we consider comparatively low intensities in the TDBOA, the above integral can easily be converted to an intensity integral using the fact that the $1s\sigma_g$ to $2p\sigma_u$ transition provides the dominant contribution to H_2^+ dissociation [20, 21]. This is a parallel, $\Delta\Lambda$=0, transition that depends only on the component of laser field along the internuclear axis. We verified that the contribution of perpendicular transitions is indeed negligible by including higher excited electronic states. We can therefore define an effective intensity, $I_{\mathrm{eff}} = I\cos^2\theta$, so that $P_{\mathrm{D}}(I,\theta) = P_{\mathrm{D}}(I_{\mathrm{eff}},0)$. This transforms the above equation to

$$\bar{P}_{\mathrm{D}}(I) = \frac{1}{2}\int_0^{I} P_{\mathrm{D}}(I_{\mathrm{eff}},0)\frac{dI_{\mathrm{eff}}}{\sqrt{I_{\mathrm{eff}}I}}. \tag{4.2}$$

We have calculated and analyzed P_{D} as a function of peak laser intensity for three pulse lengths — 10 fs, 45 fs and 135 fs. For the 45 fs and 135 fs pulses, we used a maximum peak intensity of 10^{13} W/cm^2, while for the 10 fs pulse this has been extended to 10^{14} W/cm^2. Figure 4.1 shows the results for initial vibrational states v=7, 9, and 12. Dissociation is dominated by the 1ω from v=9. The figure also includes P_{D} obtained by averaging over the initial vibrational states, each weighted by their Franck-Condon factor from the H_2 ground vibrational state as is appropriate for comparison with ion-beam H_2^+ targets [79].

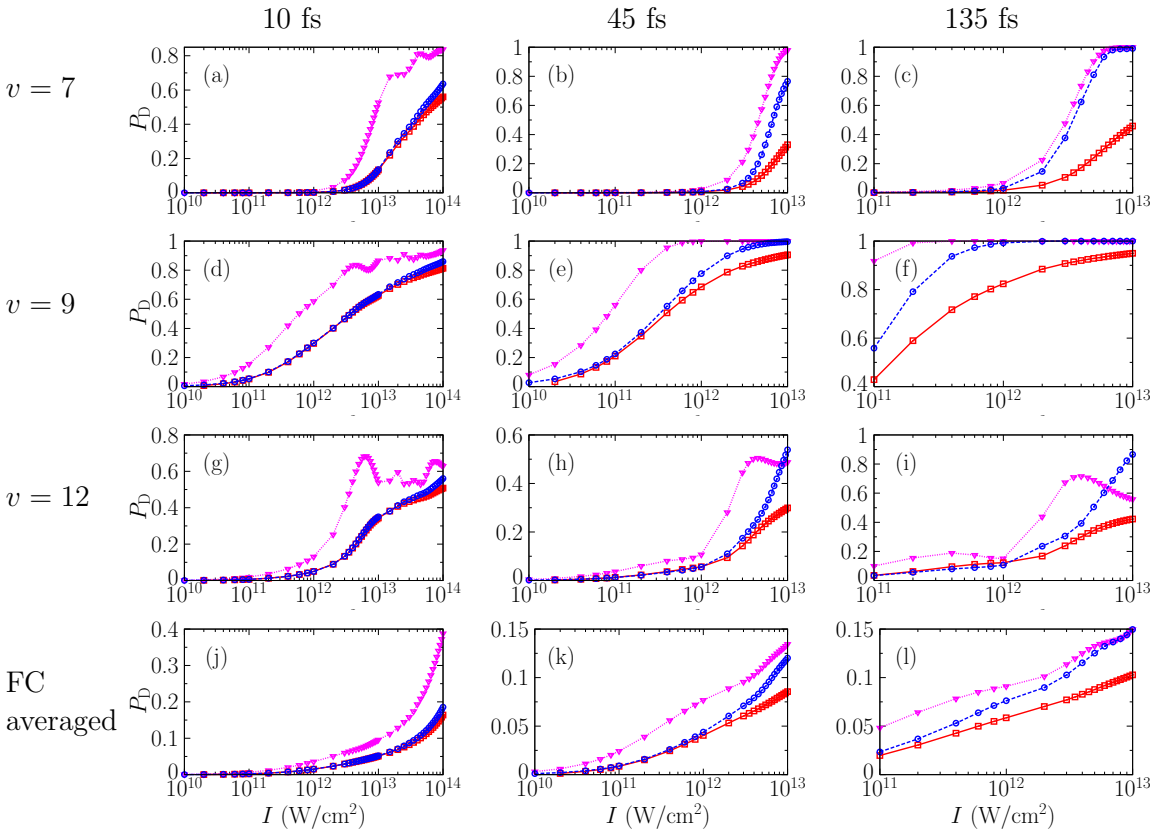

Figure 4.1 The total dissociation probability in different approximations for pulse lengths 10, 45, and 135 fs and initial vibrational states v=7,9,12. The last row presents the dissociation probability averaged over the initial Franck-Condon (FC) vibrational distribution. The red solid lines (□) show the angle-averaged $\bar{P}_D(I)$ from TDBOA; the blue dashed lines (◯), the TDBOR $P_D(I)$; and the magenta dotted lines (▽), the TDBOA $P_D(I, \theta = 0)$. Note that the panels have different scales for clarity. Figure is adapted from Ref. [5].

Figure 4.1 shows that the disagreement between the TDBOA and TDBOR results grows with laser peak intensity in every case, indicating the increasing importance of dynamic alignment with intensity — which is expected. What may not have been expected is that dynamic alignment can be significant even for 10 fs pulses, leading to a roughly 10% increase in P_{D} at 10^{14} W/cm^2 compared to purely geometric alignment. This result can be understood from the fact that at higher peak intensities, the pulse spends a much longer time at non-perturbative intensities. A 10 fs, 10^{14} W/cm^2 pulse spends roughly 25 fs at intensities above 10^{12} W/cm^2. Such exposure is sufficient to drive transitions to the higher angular momentum states needed for the molecule to align, and the time is long enough for some rotation to occur.

Figure 4.1 also shows that the difference between the TDBOR and TDBOA results grows with pulse length. As the pulse length gets longer in the TDBOR calculations, the field acts for a longer time, allowing for greater dynamic alignment. As the molecule becomes more aligned, it experiences a higher effective intensity and consequently dissociates with greater probability. In the TDBOA, the molecule cannot rotate and the molecule experiences only a fixed effective intensity throughout the pulse. By this argument, the angle-averaged TDBOA results should always underestimate the exact dissociation probability. This conclusion is supported by Fig. 4.1 except for v=12 in Fig. 4.1(i) at low intensities where the TDBOA results are slightly higher.

Another dependence of the difference between TDBOR and angle-averaged TDBOA dissociation probabilities is on the initial vibrational state. Figure 4.2(a) describes the behavior of P_{D} as a function of initial vibrational state for each pulse length. Note from Fig. 4.2(a) that $v = 7$ is the lowest state that dissociates significantly for the peak intensity of 5×10^{12} W/cm^2 for each pulse length. Moreover, P_{D} has a minimum at $v = 12$. The above mentioned two features are qualitatively same for TDBOA calculations. In Fig. 4.2(b), maximum of the difference between TDBOR intensity dependent P_{D} ($P_{\mathrm{D}}^{\mathrm{TDBOR}}(I)$) and angle-averaged TDBOA intensity dependent P_{D} ($\overline{P}_{\mathrm{D}}^{\mathrm{TDBOA}}(I)$) is plotted for peak intensity up to

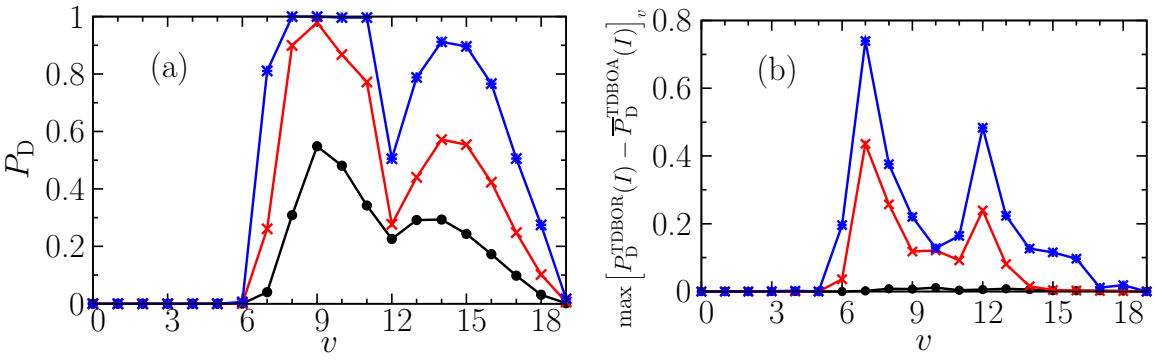

Figure 4.2 Both (a) and (b) show 10 fs (black •), 45 fs (red ×) and 135 fs (blue ∗) results; (a) shows P_D from TDBOR calculations at the peak intensity of 5×10^{12} W/cm^2; (b) shows the maximum of the difference between TDBOR and angle-averaged TDBOA intensity dependent P_D up to peak intensity of 10^{13} W/cm^2 for each initial vibrational state; $\lambda = 785$ nm.

10^{13} W/cm^2 for all pulse lengths[2]. Figure 4.2(b) shows clear peaks at $v = 7$ and $v = 12$ for 45 fs and 135 fs laser pulses. Dynamical alignment of the population during the pulse explains this behavior. Ninth vibrational state lies at 1ω crossing and very weak field can start its dissociation. So, the leading edge of the pulse will dissociate most of the population for $v = 9$ and there will not be much population left to get aligned and then dissociate. But for 7th and 12th vibrational states, the scenario is different. These vibrational states do not lie at one photon resonance and, therefore, the dissociation probability is small. The part of the population which is more aligned with laser polarization has better chance to dissociate as it experience higher effective field. In this case, leading edge of the field aligns the molecule and then it dissociates experiencing higher effective field. This dynamical alignment has been the source for the maximum difference between TDBOR and angle averaged TDBOA results as there is no rotation included in TDBOA. The magnitude of the peak at $v = 7$ is higher than the the peak at $v = 12$ because the earlier state is relatively deeply bound and easiear to rotate. In classical analogy, we can say that moment of inertia is smaller for $v = 7$ than for 12. Generally, a state requiring high field to dissociate will tend to undergo

[2]Maximum of the difference between red curves (▽) and blue curves (□) in Fig. 4.1 is plotted as a function for initial vibrational state up to peak intensity of 10^{13} W/cm^2.

more dynamical alignment.

Since the vast majority of calculations in the literature for H_2^+ in intense laser pulses are performed for molecules aligned with the laser field without angle-averaging or nuclear rotation [20, 21, 30, 32, 79–82], we have also included in Fig. 4.1 P_D for θ=0 from the TDBOA, i.e. without any angle averaging. Because they represent completely aligned molecules, these results should provide an upper limit on P_D since all molecules experience the maximum possible intensity throughout the laser pulse. As such, these θ=0 TDBOA results can also be regarded as the extreme of dynamic alignment. Fig. 4.1 again bears out these expectations with the exceptions coming now at higher intensities for v=12. The TDBOR results more-or-less interpolate between the angle-averaged TDBOA and the θ=0 TDBOA results as intensity increases from low to high.

For 10 fs pulses, the angle-averaged TDBOA provides reasonably good quantitative results over much of this intensity range, indicating that dynamic alignment is not playing a substantial role except at the highest intensities. This conclusion is, of course, consistent with the common assumption of no nuclear rotation in a pulse so much shorter than the free rotation period (556 fs for H_2^+). The θ=0 TDBOA results, however, do not agree with TDBOR for any intensities in this range, and only give reasonable qualitative agreement for the Franck-Condon averaged P_D.

The angle-averaged TDBOA also gives reasonably good quantitative results for 45 fs pulses, although over a smaller range of intensities than for 10 fs pulses. Moreover, the θ=0 TDBOA results give a better qualitative answer than for 10 fs, but little better quantitative agreement where the probability is not saturated. The Franck-Condon averaged TDBOR results, however, do appear to be headed for more quantitative agreement with the θ=0 TDBOA at higher intensities than can be reliably treated without including ionization.

For 135 fs pulses, the angle-averaged TDBOA is no longer in quantitative agreement with TDBOR for the intensity range studied. In fact, the TDBOR results are in much better quantitative agreement with the θ=0 TDBOA results, especially at higher intensities for

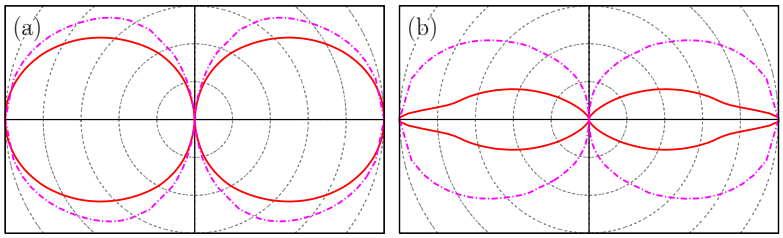

Figure 4.3 The angular distribution of p+H fragments at t_f for a 10 fs pulse: (a) I=10^{13} W/cm^2 and (b) I=10^{14} W/cm^2. The magenta dot-dashed lines show TDBOA results; and the red solid line, TDBOR. The two distributions in each panel have been normalized to have the same maximum value to better show the qualitative comparison. The laser polarization lies along the horizontal axis in these figures. Figure is adapted from Ref. [5].

the Franck-Condon averaged $P_{\rm D}$. We conclude, then, that dynamic alignment can be quite important already for 135 fs pulses — which are still shorter than the free rotation period. In fact, it was calculations at long pulse lengths similar to these that were originally used to justify using the θ=0 TDBOA calculations to *qualitatively* understand the dynamics of H_2^+ in an intense field [20]. We see from Fig. 4.1, though, that the θ=0 TDBOA calculations fail to provide a good qualitative description for most of the cases shown. The greatest discrepancies appear for the initial vibrational states at the shortest pulse lengths. Incidentally, we note that angle-averaging the TDBOA results eliminates the stabilization (decrease in $P_{\rm D}$ with intensity) seen in the θ=0 TDBOA curves for v=12. It has already been noted that inclusion of nuclear rotation largely eliminates this vibrational trapping [3][30, 32, 33], but it is interesting that angle-averaging does as well.

The comparison in Fig. 4.1 between the TDBOR and the angle-averaged TDBOA $P_{\rm D}$ shows that for moderate intensities, the angle-averaged TDBOA calculations actually give fairly accurate results for the shorter laser pulses. This finding is attractive as the TDBOA calculations are much faster than the TDBOR, even when several intensities need to be calculated to carry out the angle averaging via Eq. (4.2). On the other hand, if more detailed information such as the angular distribution is desired, then the predictive power of the TDBOA degrades quickly. Fig. 4.3 shows the Franck-Condon averaged $P_{\rm D}(I,\theta)$ for a 10 fs pulse from both calculations at the end of the laser pulse t_f (defined as the time at

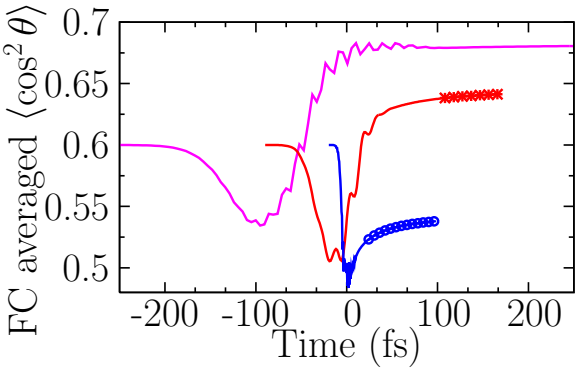

Figure 4.4 Franck-Condon averaged $\langle\cos^2\theta\rangle$ during the pulse (no symbols) and after the pulse (symbols) for 10 fs (blue $\circ$), 45 fs (red $*$), and 135 fs (magenta) pulses at I=10^{13} W/cm^2. Figure is adapted from Ref. [5].

which the intensity decays to 10^6 W/cm^2). The distributions in Fig. 4.3(a) for 10^{13} W/cm^2, where the total dissociation probabilities in Fig. 4.1 agree quite well, are similar, although not in quantitative agreement. Those in Fig. 4.3(b) for 10^{14} W/cm^2, however, show distinct differences even though the total dissociation probabilities show only about a 25% relative difference.

4.3 Dynamics after the pulse

We have already shown surprising consequences of nuclear rotation on the dissociation probability and the angular distribution at the end of the laser pulse for pulses much shorter than the free roation period. But, as mentioned previously, this distribution is not physically observable. To obtain the observable, we must extract the angular distribution from the calculations at infinite time. Since the discussion here will focus on the role of nuclear rotation in the system's evolution from the end of the pulse to infinity — and thus on the validity of the axial recoil approximation — the remainder of this chapter will be based only on the TDBOR results.

In addition to the angular distribution itself, one quantity commonly used to parametrize the alignment of a molecule is $\langle\cos^2\theta\rangle$, which is related to the width of the angular distribution for a molecule. Normally, it is the alignment of the bound molecule that is characterized

by $\langle\cos^2\theta\rangle$, but we will use it here to help understand the angular evolution of the dissociating fragments. Fig. 4.4 shows the Franck-Condon averaged $\langle\cos^2\theta\rangle$ for only the dissociating part of the wave function. The averaging is defined as

$$\langle\cos^2\theta\rangle = \frac{\sum_v f_v \langle\cos^2\theta\rangle_v}{\sum_v f_v P_{\mathrm{D}v}} \tag{4.3}$$

where the subscript v indicates the initial vibrational state, $P_{\mathrm{D}v}$ the total dissociation probability for v, and f_v is the Franck-Condon factor. The quantity $\langle\cos^2\theta\rangle_v$ in Eq. (4.3) is calculated with the time-dependent wave function that has had all of the time-independent, bound rovibrational states projected out. The initial value of $\langle\cos^2\theta\rangle$ for all three pulses is 0.6 — a consequence of the fact that dissociation from J=0 requires absorption of at least one photon and $\langle\cos^2\theta\rangle$=0.6 for J=1. This result holds for low intensity calculations with only two channels, and may change after including the π states for high laser intensities. We note that this figure also supports the discussion of the previous section, showing that the angular distribution of the fragments starts changing at times early compared to the pulse length. For instance, $\langle\cos^2\theta\rangle$ for 45 fs has reached its first extreme already at about 20 fs before the peak intensity.

Key to the present discussion is the post-pulse behavior of $\langle\cos^2\theta\rangle$. We define the time t_f at which the pulse intensity decays to 10^6 W/cm^2 as the end of the pulse, so that all subsequent evolution is effectively field-free and considered post-pulse. We note that by this definition, the time range in Fig. 4.4 spans times up to t_f for the 135 fs pulse. Towards the end of the pulse, $\langle\cos^2\theta\rangle$ for the 135 fs pulse has already obtained its asymptotic value, implying that the axial recoil approximation works quite well for 135 fs or longer pulses. In contrast, $\langle\cos^2\theta\rangle$ for both 45 and 10 fs pulses continues to change towards the end of pulse and after.

We can understand the behavior displayed in Fig. 4.4 in exactly the same way that the alignment of bound states by intense laser pulses is understood [101]. In that case, there are two limits: impulsive alignment when the pulse is much shorter than the free rotation period, and adiabatic alignment when the pulse is much longer. The mechanism of impulsive

alignment is the generation of a distribution of angular momentum states by the laser pulse that do not have time to evolve during the short pulse. There is thus no alignment during the pulse, but the distribution continues to evolve freely after the pulse ends, leading to periodic revivals during which the molecules are maximally aligned. In a long laser pulse, molecules adiabatically align because the field-free states adiabatically correlate to pendular states in the field — the lowest of which is strongly aligned. The pendular states also involve a broad distribution of angular momentum states, but in a long pulse, they have time to evolve into a narrow angular distribution.

Given these two alignment mechanisms, we see from the behavior in Fig. 4.4 that the 10 fs and 45 fs data are explained by impulsive alignment, demonstrating that this mechanism works for the dissociating fragments as well as for the bound components. Because the dissociating component has acquired a broad angular momentum distribution similar to the bound component, it continues to evolve after the pulse, becoming more aligned on the way to the detector. There are no revivals for the dissociating component since its moment of inertia grows as the fragments separate, effectively freezing the angular distribution as the fragments fly to the detector. The 135 fs data, on the other hand, is explained by adiabatic alignment. When the molecule becomes aligned near the peak intensity of the pulse, it dissociates. Because it was in a pendular (or near-pendular) state, its angular distribution did not evolve further.

To quantify the post-pulse alignment, we have calculated $\langle \cos^2 \theta \rangle$ at infinite time. Two ways to do this are to continue propagating the dissociating part of the wave function to very large times, or by writing the wave function at the end of the pulse in terms of the exact scattering states, superposed to give outgoing plane waves at large internuclear distances as described in Sec. 2.3.7. The former scheme is not very practical and involves extensive computational work. Therefore, we adopted the latter scheme, but double checked it for one pulse length with the former to confirm that they converged to the same answer at very large times. Table 4.1 shows the results for the three pulses of Fig. 4.4, and the results are

FWHM (fs)	$\langle\cos^2\theta\rangle$ at t_f	$\langle\cos^2\theta\rangle$ at $t\to\infty$	Relative change (%)
135	0.681	0.683	0.3
45	0.640	0.648	1.2
10	0.523	0.545	4.2

Table 4.1 Franck-Condon averaged $\langle\cos^2\theta\rangle$ from TDBOR for I=10^{13} W/cm^2.

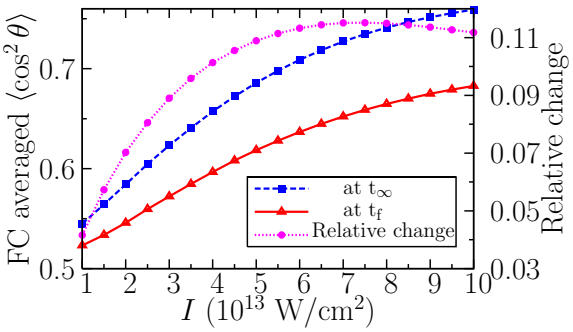

Figure 4.5 Franck-Condon averaged $\langle\cos^2\theta\rangle$ from TDBOR at the end of the pulse (t_f) and at the detector ($t\to\infty$) for a 10 fs pulse. Figure is adapted from Ref. [5].

consistent with that figure. For the 135 fs pulse, the angular distribution is more aligned than both the 45 and 10 fs pulses, but it barely changes on its way to the detector. The shorter pulses are less aligned, but have much larger relative change in $\langle\cos^2\theta\rangle$ after the pulse.

One natural question is: can the relative change in $\langle\cos^2\theta\rangle$ after the pulse be larger than the 4% found for the 10 fs pulse? To answer this question, we studied the dependence of the post-pulse alignment on laser peak intensity for the 10 fs laser pulse. Fig. 4.5 shows the results. In fact, the relative change grows by about a factor of three to a maximum of about 11% as the peak intensity is raised from 10^{13} W/cm^2. From Fig. 4.5, we see that the values of $\langle\cos^2\theta\rangle$ at t_f and $t\to\infty$ both increase monotonically with intensity. It has already been mentioned, however, in previous section that higher intensities mean longer pulse duration above perturbative intensities and consequently large dynamic alignment during the pulse, implying that relative change of $\langle\cos^2\theta\rangle$ should therefore have a maximum and become gradually smaller with increasing intensity. It appears that we have located this

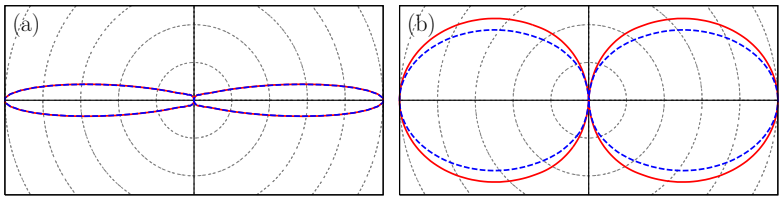

Figure 4.6 Franck-Condon averaged TDBOR angular distribution for dissociation in (a) 135 and (b) 10 fs pulses at I=10^{13} W/cm^2. Red solid lines denote distribution at t_f; and blue dashed lines, at $t\rightarrow\infty$. Figure is adapted from Ref. [5].

maximum value at laser peak intensity of 7×10^{13} W/cm^2. Of course, at higher intensities, the competing process of ionization will become increasingly important, and we do not know what its impact will be. We can conclude, though, that the axial recoil approximation is breaking down for dissociation of H_2^+ in 10 fs laser pulses.

To better visualize the post-pulse alignment, it helps to study the full angular distributions rather than just their width via $\langle\cos^2\theta\rangle$. So, we show in Fig. 4.6 angular distributions at t_f and $t\rightarrow\infty$ for 10^{13} W/cm^2. It is evident from Fig. 4.6(a) that the fragments from dissociating H_2^+ in a 135 fs laser come out very aligned and do not rotate appreciably as they head towards the detector. The 10 fs distribution in Fig. 4.6(b), whose $\langle\cos^2\theta\rangle$ increased by 4% after the pulse, does show visible post-pulse narrowing.

Qualitatively, the t_f and $t\rightarrow\infty$ distributions in Fig. 4.6 are similar, even for the 10 fs pulse. Is it possible, then, to find qualitatively different t_f and $t\rightarrow\infty$ angular distributions? The answer is yes, and a few examples are shown in Fig. 4.7. Fig. 4.7(a) and 4.7(b) compare the distributions for a 10 fs pulse at these two times for higher intensities where the effect is more dramatic as is suggested by Fig. 4.5. If the t_f and $t\rightarrow\infty$ angular distributions were both experimentally measurable, it would certainly be possible to distinguish them. Even more dramatic is the comparison between Fig. 4.7(b) and Fig. 4.3(b). The red curve in both cases is the same, showing that the TDBOA calculations certainly cannot be used to predict the angular distributions at the detector for 10^{14} W/cm^2.

We also compare in Fig. 4.7 the results for a 5 fs laser pulse to see if nuclear rotation could possibly be important for such a short pulses. Note that although the physical observables

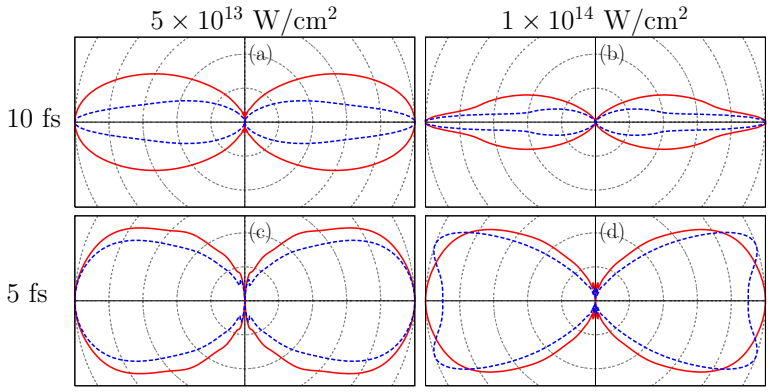

Figure 4.7 Franck-Condon averaged TDBOR angular distribution for dissociation. Red solid lines denote distribution at t_f; and blue dashed lines, at $t \to \infty$. Figure is adapted from Ref. [5].

generally show some dependence on the carrier-envelope phase for such short pulses [44], we show results only for zero carrier-envelope phase. For comparison, $\langle \cos^2 \theta \rangle$ for Fig. 4.7(c) and 4.7(d) at t_f is 0.531 and 0.576, respectively. While these values are smaller than for the corresponding 10 fs angular distributions, the relative post-pulse changes in $\langle \cos^2 \theta \rangle$ of 10.5% and 12.3%, respectively, are higher than for the 10 fs pulse, continuing the trend already observed. Fig. 4.7 shows, however, that their post-pulse evolution is quite different and that the angular distribution does not look as sharply aligned. Moreover, structure has developed in the angular distribution in Fig. 4.7(d).

4.4 Summary

We have studied the dynamics of the angular distribution of p+H fragments following intense field dissociation of H_2^+ both during and after the laser pulse. We found significant dynamic alignment during 135 fs pulses, but little rotation after the pulse. We also found that geometric alignment dominates during 10 fs pulses of moderate intensity, but the molecules can rotate considerably after the pulse. Consequently, the axial recoil approximation appears to hold best for pulses on the order of 135 fs or longer. Also consequently — and contrary to the assumptions in most work in this field — nuclear rotation must be included to correctly predict even qualitatively the angular distribution of H_2^+ dissociation in short pulses.

Chapter 5

Ro-vibrational revival structure of H_2^+ in short laser pulses

5.1 Introduction

Ongoing advancements in laser technology have enabled experimentalists to uncover dynamics of chemical reactions involving atoms and molecules. Some molecular phenomena, such as high-harmonic generation and above threshold ionization, depend strongly on molecular alignment and orientation [67, 69, 102, 103]. These findings have led to a greater interest in studying laser induced alignment and orientation of molecules. Recently, alignment has become an important first step in different experimental schemes, e.g. tomographic imaging of molecules using high harmonic generation [104, 105].

Alignment of molecules can mostly be obtained using two methods, namely adiabatic or non-adiabatic alignment. Adiabatic alignment is obtained by slowly ramping up the laser field followed by a slow turn-off with pulse durations greatly exceeding the rotational period. Maximum alignment can only be obtained at the peak of the field. Despite the drawback of the presence of the field for some alignment experiments, a much higher degree of alignment can be achieved adiabatically [106]. In contrast, for non-adiabatic alignment, a laser pulse shorter than the rotational period of the molecule creates a coherent rotational wave packet towards the peak of the field, which then evolves and revives at multiples of $1/2B$, where $B = 1/2\mu R_0^2$ is the rotational constant, μ is the reduced mass of the molecule,

and R_0 is the equilibrium distance between nuclei [21, 107, 108]. Non-adiabatic alignment is a useful way to get a field-free aligned distribution of the molecules, although the degree of alignment can be smaller than in the adiabatic case. Numerous experimental and theoretical studies have been conducted for rotational revivals of the neutral molecules and references there in [101]. A comprehensive review about revivals in general can be found in Ref. [109]. There is also a renewed interest in using both adiabatic and non-adiabatic methods to align molecules [110–117]. Many studies cover the topic of optimally controlling and enhancing the alignment by the combination of pulses, pulse shaping or thermally cooling the target molecules [111, 118, 119]. Alignment of molecules is a commonly studied area of research and almost a separate sub-field, thus it is difficult to overview many previous studies.

Alignment in heteronuclear molecules occurs due to the interaction of the permanent dipole moment and induced polarizability which results from the change in electronic distribution caused by the field. For homonuclear molecules, it is mostly the induced polarizability that causes alignment. Induced polarizability is small for the simplest H_2 molecule (2.8 a.u.) compared to other molecules such as N_2 (7.43 a.u.). H_2 is difficult to align because of its small induced polarizability. Only recently some experimental studies have observed non-adiabatic alignment of H_2 and D_2 [120, 121]. Revival structure has not been reported for H_2^+.

While revival structure has been studied and widely understood for neutral molecules, little is known about the rotational revivals of molecular ions. We don't expect neutral ionic rotational revivals to behave differently for a single vibrational state of molecules. However, in molecules like H_2^+, a broad initial vibrational state distribution can change the behavior because of the correlated vibrational and rotation motion. H_2^+ produced in an ion-source has broad initial vibrational and rotational distributions with typical thermal temperature up to 400 K. Our discussion will be focused on the rotational revival structure of H_2^+, and thus rovibrational correlation is important. The role of correlation between rotational and vibrational motion has previously been studied for rotational revivals of Na_2 molecules [122].

The findings here are somewhat different from Ref. [122]. No half- or quarter-revivals were predicted for rotational revivals of Na_2 molecules in Ref. [122]. In our results, both quarter- and half-revivals can be observed in some cases along with full revivals at about 4 ps. The revival time of 4 ps is much longer than the expected revival time of $1/2B$. It was also shown in Ref. [122] that the correlation between rotational and vibrational motion makes the revival time much longer than $1/2B$, however their method to estimate revival time does not reproduce 4 ps for H_2^+.

Our focus for this work was to present an understanding of the rotational dynamics of the H_2^+ bound wave function during and after its interaction with the short laser pulses by studying $\langle \cos^2\theta \rangle$. For this purpose, a systematic study has been conducted with laser peak intensities for 10 and 135 fs pulses. The results are only Franck-Condon averaged over incoherent initial vibrational states distribution. The results show a clear signature of rotational revivals in $\langle \cos^2\theta \rangle$ with time. Experimentally observing revivals for molecular ions is challenging. A pump-probe study would be necessary to observe the rotational revivals, first by launching a coherent angular wave packet by the pump pulse which later on is monitored by the probe. Starting from H_2^+ ion-beam experiment [15], would be a clean experiment to observe these revivals. A neutral target as in a gas-jet experiment makes it difficult to observe H_2^+ revivals. Fragments from double ionization of H_2 and single ionization of the H_2^+ have the same kinetic energy, and the signal for the former would be much bigger than the latter. Because of this overlap in the kinetic energy, it becomes very difficult to separately observe H_2^+ rotational dynamics [121]. Pump-probe studies, however, have never been performed in an ion beam experiment.

While discussing rotational revivals of H_2^+, we can also address some questions by looking into the dynamics $\langle \cos^2\theta(t) \rangle$ for bound wave functions. One question is "does only the aligned part of the bound distribution dissociate", thus burning a hole in the initial angular distribution. Another question about the angular distribution of the molecule is "Is the angular distribution always aligned along the laser polarization at the end of the pulse".

Since, thermal averaging affects the revival structure, I will briefly discuss it in this chapter.

In this chapter, all the calculations are performed using the TDBOR method described in Sec. 2.2.1. The major analysis we performed is the calculation of $\langle\cos^2\theta\rangle$. For the discussion presented in this chapter, we calculate FC-averaged $\langle\cos^2\theta\rangle$. We will call FC averaged $\langle\cos^2\theta\rangle$ simply $\langle\cos^2\theta\rangle$, and will use $\langle\cos^2\theta\rangle_v$ for each initial vibrational state v. Detailed derivations of $\langle\cos^2\rangle_v$ and $\langle\cos^2\theta\rangle$ have already appeared in Sec. 2.3.5. For the results presented in this chapter, we have used zero initial J and M and performed calculations for all the bound vibrational states in the $1s\sigma_g$ channel to do FC-averaging.

5.2 Origin of rotational revival structure

Figure 5.1 shows rotational revival structure (RRS) for H_2^+. Rotational revival appears at $\sim$ 4 ps measured from the peak of the laser pulse. The effect of correlated rotational and vibrational motion on the RRS has been studied in Ref. [122]. The revival time ($T_{\rm rev}$) was predicted for a rovibrationally hot wave-packet in an excited state of the Na_2 molecule. The prediction for $T_{\rm rev}$ in Ref. [122] is based on a model Morse potential for the Na_2 molecule. We, however, could not reproduce the RRS time for H_2^+ using this model. We see from Fig. 5.1 that $\langle\cos^2\theta\rangle(t)$ has a fast oscillation under a slowly varying envelop and after two significant clean revivals the slow envelope starts damping. This is a typical behavior of quantum mechanical revivals since the phase relation between different states in wave function becomes random at very long times and then loses coherence making the revivals smaller [109].

How does the rotational revival originate? To answer this question, it is important to look to each vibrational component separately. In Fig. 5.2, the left panel shows $\langle\cos^2\theta\rangle_v(t)$, defined in Eq. (2.32), for every other v, together making up more than 90% of the FC wave packet. The right panel of Fig. 5.2 shows $Q_{v(t)}$, defined as

$$Q_v(t) = \frac{\sum_{v'=0}^{v} f_v P_{v'B}(t)\langle\cos^2\rangle_{v'}(t)}{\sum_{v'=0}^{v} f_{v'} P_{v'B}(t)} \tag{5.1}$$

We see from Fig. 5.2(a)-(c) the beating of a single frequency that corresponds to the energy

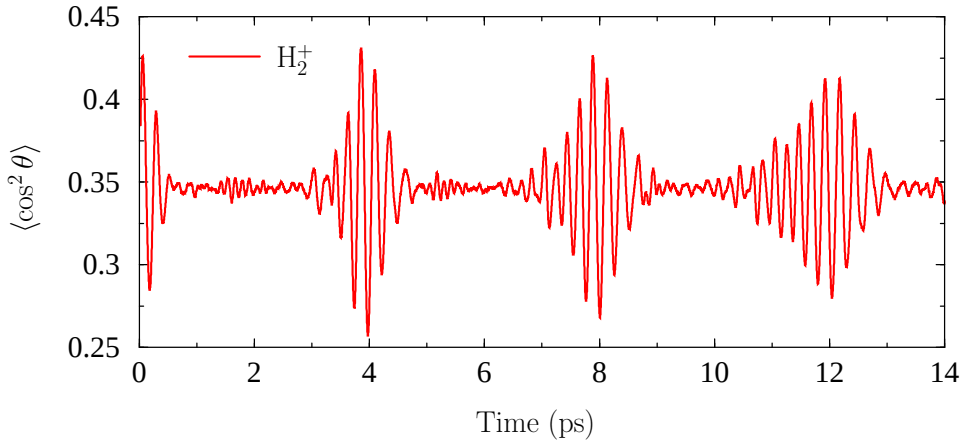

Figure 5.1 Rotational revival structure for H_2^+ ; I= 10^{13} W/cm^2; $\tau_{\rm FWHM}$ = 10 fs; λ = 785 nm.

difference between $J = 0$ and $J = 2$ rotational states for the corresponding vibrational states. If we picture populating many J's as climbing a ladder, from $J = 0$ to 1, from 1 to 0 and 2, from 2 to 1 and 3, and so on, then the states close to one photon resonance can have broader angular momentum distributions than the ones far from it. To climb up the ladder of J in the $1s\sigma_g$ channel, electronic transitions in many Js in $2p\sigma_u$ are necessary. For the laser parameters in Fig. 5.2, we used only two electronic channels in the calculations, namely $1s\sigma_g$ and $2p\sigma_u$. For initial $J = 0$, $1s\sigma_g$ has only even and $2p\sigma_u$ has only odd partial waves. Vibrational states $v = 0$, 2, and 4 are deeply bound, thus a short weak laser pulse seems to populate a single excited rotational level and its population grows with v, making the amplitude of the beating frequency larger as v increases. However, as the v becomes closer to the one photon channel opening, more frequencies start contributing, and we can see the distorted beating pattern of the single frequency as in the case of Figs. 5.2(d) and (e). We see noisy structure in $\langle\cos^2\theta\rangle$(t) for $v = 10$, as shown in Fig. 5.2(f) as the J-distribution becomes broad with many high Js having comparable contributions.

The right panel of Fig. 5.2 shows the development of RRS for a FC wave packet of H_2^+ as we keep accumulating vibrational states starting from $v = 0$ to $v = 10$. Figures 5.2(a) and 5.2(g) are the same. We can explain the RRS of H_2^+ as the cumulative sum of beating frequencies from all individual vibrational states as evident from Figs. 5.2(h-l). The addition

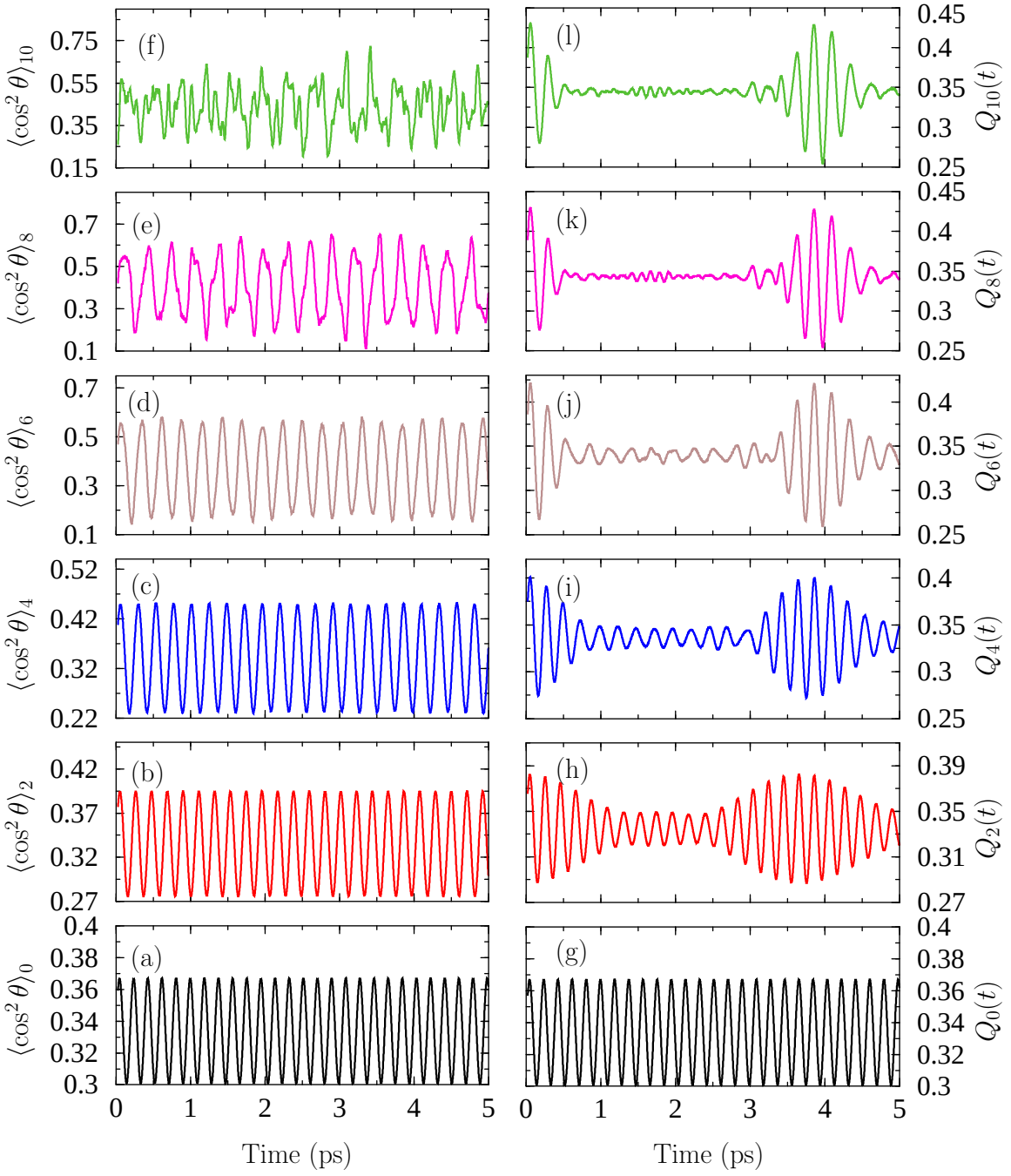

Figure 5.2 Left panel shows Eq. (5.2) for $v = 0$, 2, 4, 6, 8 and 10. Right panel shows Eq. (5.1). I= 10^{13} W/cm^2, $\tau_{\mathrm{FWHM}} = 10$ fs, and $\lambda = 785$ nm.

of different frequencies results in a revival period of about 4 ps for H_2^+. Even though the vibrational state results are added incoherently, the fact that each result is a sinusoidal oscillation leads to the interference. While eliminating all the vibrational states except the lowest three right panels will not change this time significantly (see Fig. 5.2(h)), the RRS will not be very clear. If the bound wave function of H_2^+ contains only lower vibrational states (in particular 0–5), the RRS will have a beating frequency closer to that of the lowest v with some modulation between revivals. The rotational revival structure will also not have any fractional revivals, which can be seen in Figs. 5.2(k) and 5.2(l) after including v up to 10. Moreover, large amplitudes for high-lying individual vs of $\langle \cos^2\theta \rangle_v$ translate into the large amplitude of RRS after performing FC averaging and also increase the averaged alignment. So, we can clearly state two significant features of RRS as, (i) for moderate intensities, low lying vibrational states (0-5) give a RRS with relatively small amplitude and no fractional revivals, and (ii) vibrational states from 6 to 12 contribute significantly to the RRS amplitude, making it localized in time and also giving fractional revivals.

5.3 Effect of laser peak intensity on rotational revivals

For observing any physical phenomenon involving atoms and molecules with intense laser pulses, it is always crucial to see the effect of laser peak intensity on that process. To be an observable the effect should survive focal volume averaging of the laser spatial distribution in an experiment [69]. Thus, the question arises, how can laser peak intensity effect RRS?. Moreover, as some physical phenomena can change dramatically with pulse duration e.g. carrier-envelope phase effects, the axial recoil approximation, and above-threshold dissociation [4, 5][44], it would be useful to discuss the intensity dependence of RRS for two distinct pulse lengths, namely 10 fs and 135 fs.

5.3.1 Rotational revival structure for 10 fs pulse

To study the intensity dependence of RRS for a 10 fs pulse, in Fig. 5.3, it is plotted for many intensities. Figure 5.3 shows that the RRS amplitude increases with laser peak intensity I and the averaged alignment shifts slightly to higher values. The first two terms of

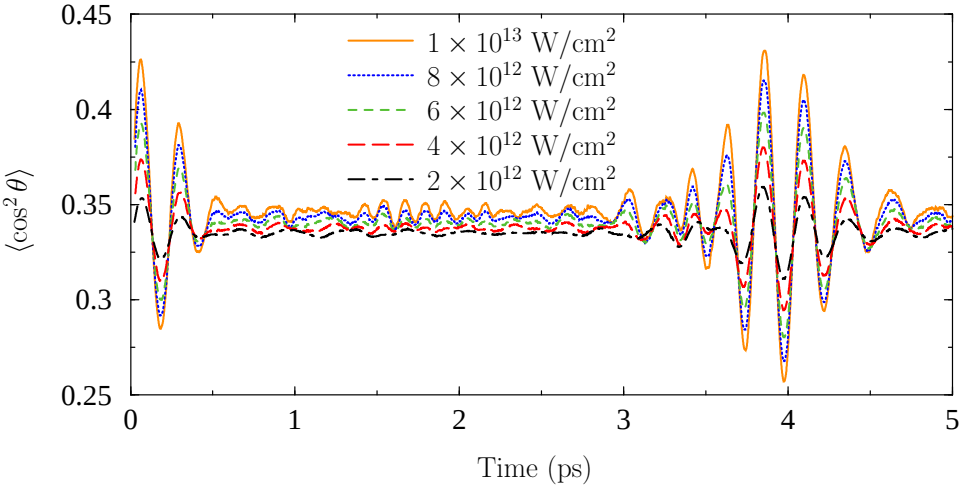

Figure 5.3 RRS for different intensities. Intensity ranges from 2×10^{13} to 10^{13} W/cm^2 with each line representing a single I in an ascending order from down with lowest I to up. $\tau_{\mathrm{FWHM}} = 10$ fs, $\lambda = 785$ nm.

Eq. (2.32) the averaged alignment, and the last term is responsible for the RRS amplitude. For completeness I rewrite Eq. (2.32) here

$$\begin{aligned}\langle\cos^2\theta\rangle_v(t) \;=\; & \frac{1}{3P_{\mathrm{B}v}(t)}\Bigg[P_{Bv}(t) + 2(-1)^M \sum_J (2J+1) \sum_{v'} |a_{Jv'}(t)|^2 \\ & + 4(-1)^M \sum_J \sqrt{(2J+3)(2J+1)} \begin{pmatrix} J+2 & 2 & J \\ -M & 0 & M \end{pmatrix} \begin{pmatrix} J+2 & 2 & J \\ 0 & 0 & 0 \end{pmatrix} \\ & \times \sum_{v'v''} \langle\chi_{J+2v''}|\chi_{Jv'}\rangle \mathrm{Re}\left(a^*_{J+2v''}(t) a_{Jv'}(t)\right)\Bigg] \end{aligned} \tag{5.2}$$

and $\langle\cos^2\theta\rangle$ from Eq. (2.31)

$$\langle\cos^2\theta\rangle(t) = \frac{1}{P_{\mathrm{B}}(t)} \sum_v f_v P_{\mathrm{B}v}(t) \langle\cos^2\theta\rangle_v(t). \tag{5.3}$$

It follows from Eq. (5.2) that a higher $P_{\mathrm{B}v}$ and/or a broader J-distribution will result in a larger averaged alignment and a large RSS amplitude. Note that $P_{\mathrm{B}v}$ in the denominator of

Eq. (5.2) will be cancelled when we renormalize it to calculate $\langle \cos^2\theta \rangle$. Figures 5.4(a) and 5.4(b) show the distribution of highest J with population probability $\geq 10^{-7}$ ($J_{\max}$) and $P_{\rm B}$ as a function of v and I for a 10 fs pulse, respectively. Figures 5.4(a) and 5.4(b) show that both $J_{\max}$ and $P_{\rm B}$ for low lying v (0–5) are not affected significantly for the range of intensities considered. This implies that high lying v (mostly 6–12) are responsible for the dependence of RRS on I in Fig. 5.3.

We should be careful about our interpretation of the phenomenon because we notice from Figs. 5.4(a) and 5.4(b) that while $J_{\max}$ increases with I for $v = 6$ to $v = 12$, $P_{\rm Bv}$ decreases for these vibrational states. To have a significant effect on RRS, $P_{\rm B}$ should not decrease faster than the increase in $J_{\max}$. There is a competition between populating more J's and becoming depleted. This has been discussed in Sec. 4.2, that dynamical alignment (alignment of the bound wave function during the pulse) is large for the vibrational states away from the maximum of the one photon channel opening, i.e. all the states from $v = 6$ to 12 except $v = 9$ will first align in the field and then dissociate. This dissociation probability depends on the pulse duration. So, for a pulse significantly shorter than the rotational period, a certain v will become more aligned compared to being depleted. This is the reason that we see an increase in RRS amplitude and averaged alignment for a 10 fs pulse.

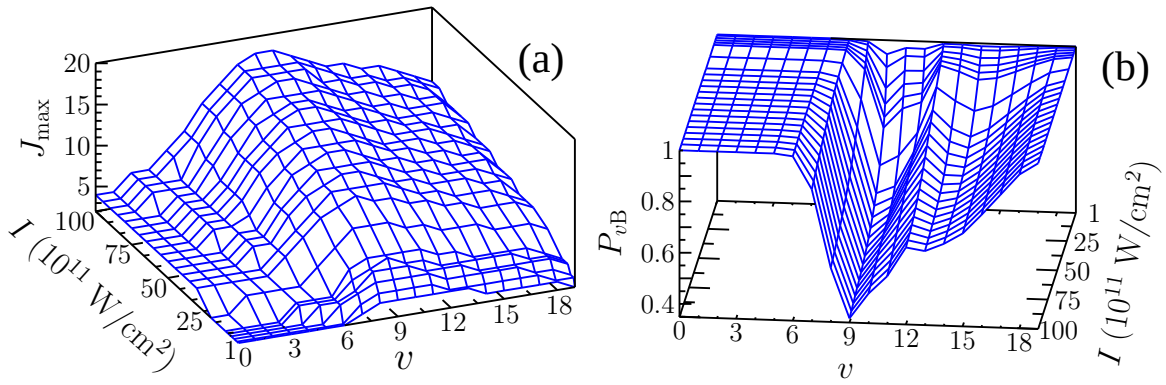

Figure 5.4 (a) Distribution of $J_{\max}$ (highest occupied J with probability $\geq 10^{-7}$) vs v and I; (b) $P_{\rm B}$ for 10 fs for each v and as a function of I.

Another important question is whether the individual peaks shift with I in RRS. The peak shift, however, is negligible with I as shown in Fig. 5.3. This is somewhat surprising. to

see a very small. The origin of the intensity dependent shift in RRS peaks can be explained as follows. Rotational revival structure appears as a result of constructive interference in $\langle \cos^2 \theta \rangle$ between different rovibrational states contributing to the bound population of the molecule. Thus the phase of the amplitude for each rovibrational state is important. The phase accumulated depends upon the time during the laser pulse that a certain level becomes populated. For example, a certain component of the bound wave function can only become populated at 10^{12} W/cm^2 which occurs at $t = 0$ for $I = 10^{12}$ W/cm^2. However, the same component would become populated at a much earlier time for $I = 10^{13}$ W/cm^2 and hence the time for constructive interference for the component with other components will change. In addition, the shift in peak positions of RRS can depend on the FWHM of the laser pulse. As for a 10 fs pulse, while the time is different to populate a certain state for different I's, it may be just 3 to 7 fs which is not big compared to the fast oscillation in RRS with a frequency of about 200 fs. Since the field envelope varies slowly, a long pulse might make a larger shift. To this end, we have performed calculations using 135 fs pulses and the results will be discussed in the following section.

5.3.2 Rotational revival structure for a 135 fs pulse

We have performed several calculations using a 135 fs laser pulse for the range of intensities as in the case of 10 fs. The RRS's for a 135 fs pulse for several I's have been shown in Fig. 5.5. I will first complete the discussion of drift in peak positions of RRS with I and then will return to comment on general features of RRS for a long pulse of 135 fs. Figure 5.5 shows that peak positions, indeed, drift away from each other as a function of I. This can be seen for the peak at about 0.4 ps for 10^{13} W/cm^2. More clearly, the drift can be observed in Fig. 5.6(a). Figures 5.5 and 5.6(a) show that the RRS peaks drift towards longer time as a function of I. This can be explained again considering the fact that to be able to interfere constructively, a certain amount of phase has to be accumulated for the amplitude of each rovibrational state. The later in the pulse a state gets populated, the longer it will take

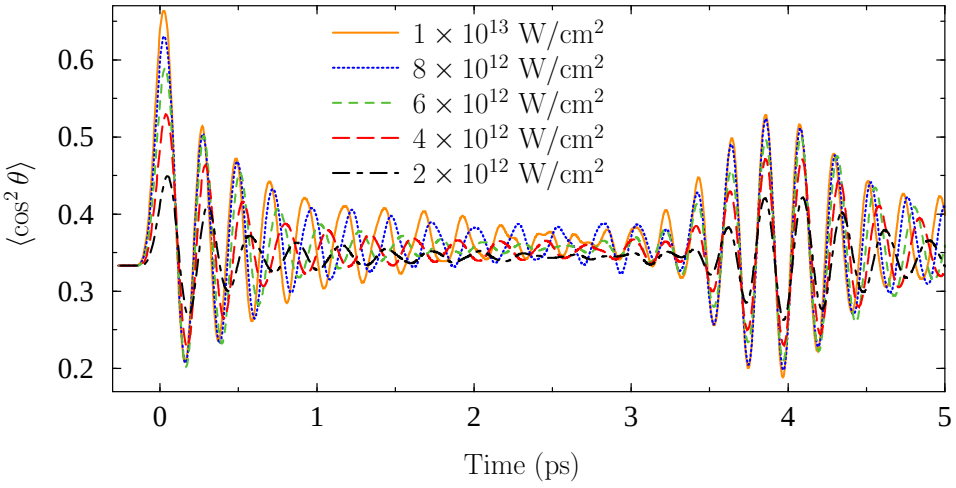

Figure 5.5 Same as Fig. 5.3 for $\tau_{\mathrm{FWHM}} = 135$ fs and $\lambda = 785$ nm.

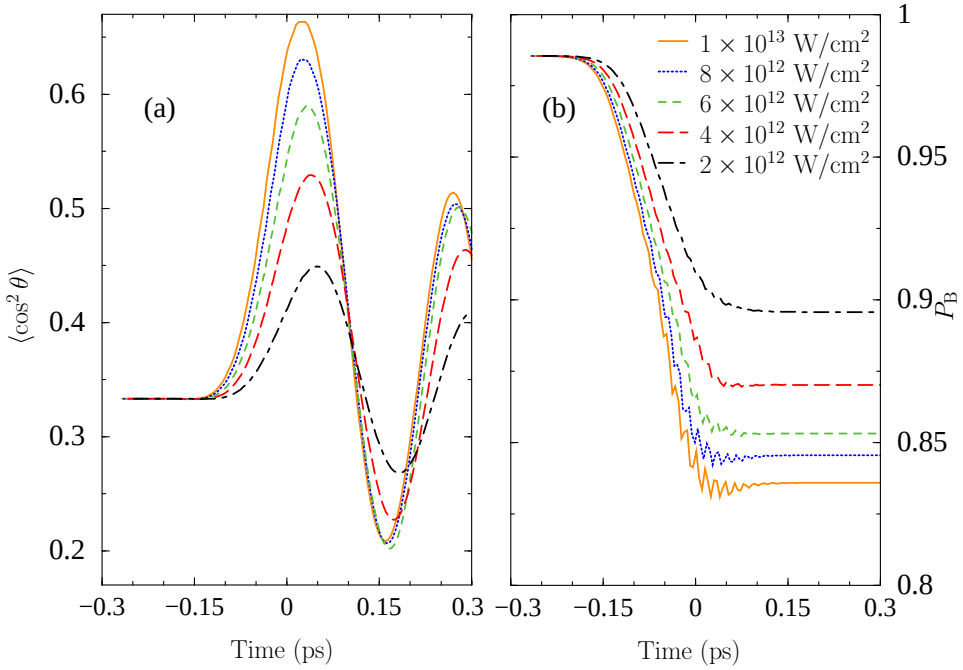

Figure 5.6 (a) shows RRS and (b) P_{B} as a function of time when the pulse is on ($t \leq t_f$). $\tau_{\mathrm{FWHM}} = 135$ fs, $\lambda = 785$ nm.

to accumulate the phase required to interfere constructively. It is remarkable that after becoming completely off in position from each other, the RRS peaks reappear at about 3.9 ps with negligible difference in positions with intensity. We can summarize the main features

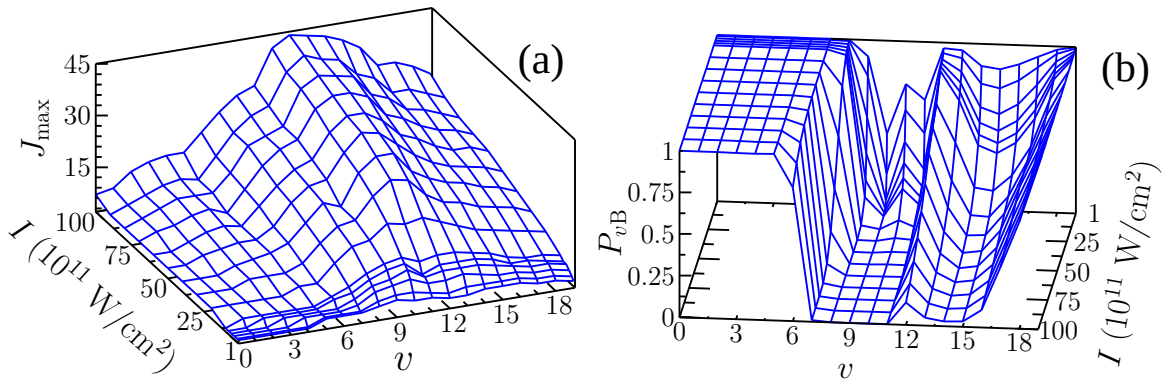

Figure 5.7 (a) same as Fig. 5.4(a) and (b) same as Fig. 5.4(b) for $\tau_{\mathrm{FWHM}} = 135$ fs.

of RRS for 135 fs pulse as follows. Averaged alignment and amplitude for RRS increase with I indicating broader J-distribution. The distribution of $J_{\max}$ vs. v and I is shown in Fig. 5.7(a). Figure 5.7 shows that a 135 fs pulse can populate many J's for low lying $v's$ (from 0 to 5) as well compared to 10 fs pulse. For even the lowest I plotted, the RRS looks similar to Fig. 5.2(j), i.e. no half revivals and $< \cos^2\theta >$ oscillates with smaller amplitudes between RRS. For higher intensities, the RRS becomes more like Fig. 5.2(i) which does not contain any component from $v > 4$, and thus indicates small P_{B} for $v > 5$. Figure 5.7(b) shows $P_{\mathrm{B}v}$ and supports the evidence.

There is another interesting feature of the RRS that can be seen clearly for 135 fs. Figures 5.5 and 5.6(a) show that the amplitude for the first peak of the RRS is significantly larger than the second peak and the peaks at the revival time. The first two peaks of the RRS (see Fig. 5.5) appear during the pulse fora 135 fs laser pulse. The question arises, what is the origin of this dramatic decrease in amplitude from the first to the second peak and later peaks? The reason is rather simple and quite intuitive. The states become aligned at about $t = 0$, and then dissociate leaving behind less aligned states. The depletion of the aligned states makes RRS amplitude small and also lowers the contrast in $\langle\cos^2\theta\rangle$ between the RRS and when the population becomes dephased. Figure 5.6(b) shows the survival probability of the molecule, $P_{\mathrm{B}}(t)$. We see from Figs. 5.6(a) and 5.6(b) that as P_B becomes small with I, the contrast between the amplitudes of the first two peaks becomes large.

Comparing Figs. 5.3 and 5.5, we find that the RRS features do not change significantly over the range of I plotted for 10 fs compared to 135 fs pulse. The reason is that $P_{\mathrm{B}v}$ does not change dramatically for 10 fs with I, while for 135 fs high lying v's change from almost bound to completely depleted for the same range of peak intensity. To clarify this point, we plot the relative population of these states to the total bound probability P_{B} for a FC wave packet as a function I for both 10 and 135 fs laser pulses in Fig. 5.8. Figure 5.8 shows that

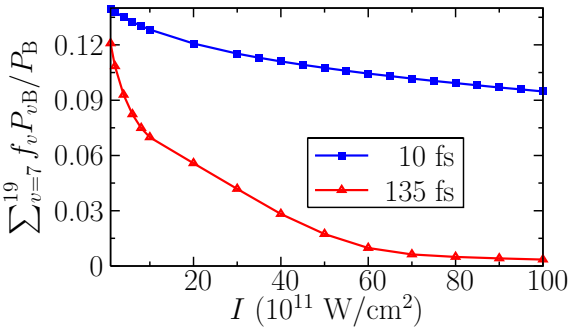

Figure 5.8 Ratio of bound probability for $v = 7$ to $v = 19$ to P_{B} for 10 fs and 135 fs laser pulses.

while the ratio is not very different at the lowest I (12% for 135 fs and 13.5% for 10 fs), it decreases to less than 1% for 135 fs, while staying still quite large about 9% for 10 fs at the highest I. Therefore, the RRS for the 10 fs pulse remains unaffected compared to that of 135 fs for intensities ranging from 10^{12} to 10^{13} W/cm^2.

5.4 Pulse length effect

Mostly, intensity and pulse length dependencies of RRS features have already been covered in previous sections. It will, however, be interesting to see the crossover of the RRS from being like Fig. 5.2(l) to Fig. 5.2(i) as the pulse length increases. Moreover, we can also try to estimate at approximately which pulse duration the amplitude at the first peak of the RRS becomes significantly larger than the subsequent peaks indicating the depletion of high lying vibrational states in the trailing part of the pulse. To observe this behavior, we have performed many calculations for pulse lengths ranging from 10 fs to 135 fs. Figure 5.9 shows fractional (half) revivals for both 45 and 60 fs pulses. As the pulse length becomes 90 fs,

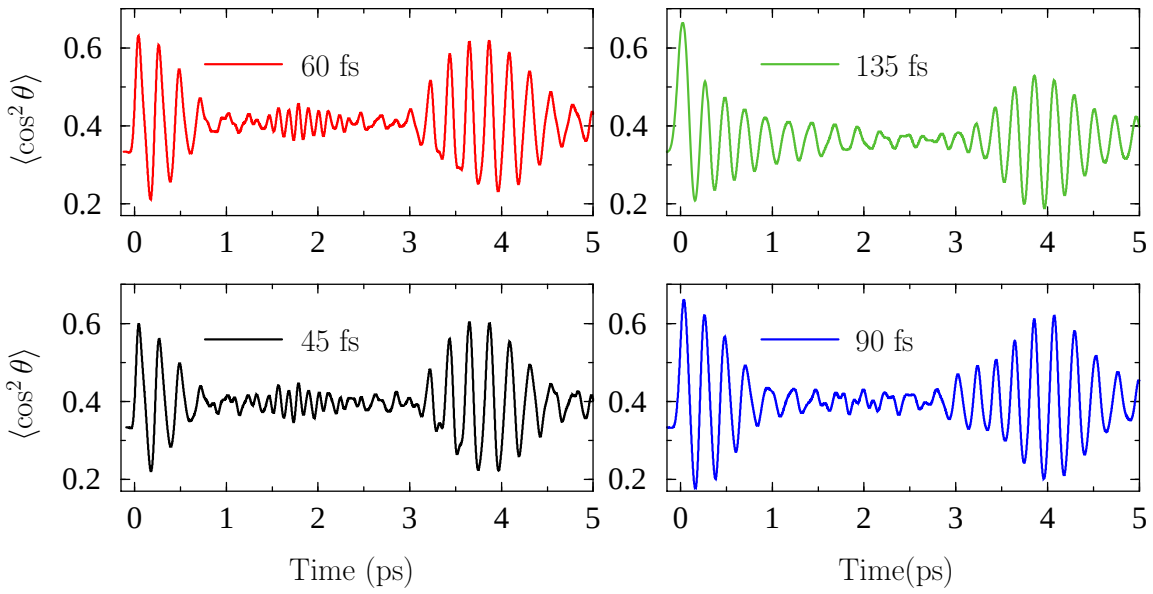

Figure 5.9 Rotational revival structure for four different pulse lengths as indicated at fixed $I = 10^{13}$ W/cm^2.

however, the RRS looks more like Fig. 5.2(j). So, the crossover between the two behaviors of the RRS will lie between 60 and 90 fs pulses for $I = 10^{13}$ W/cm^2. Moreover, the J-distribution becomes broader with pulse length, giving higher alignment at the RRS peaks as the pulse length increases from 45 fs to 90 fs. The depletion, however, also increases with pulse length, which finally results in a smaller RRS amplitude for 135 fs at the revival time. So, the depletion overrides alignment for pulses between 90 and 135 fs.

5.5 Concluding remarks

We have presented rotational revival structures for a range of laser peak intensities and pulse lengths for an initial incoherent vibrational wave packet with $J = 0$ of H_2^+. We found that for a broad range of I and pulse lengths, rotational revivals occur more or less at the same time of 4 ps. This time is characteristic of the molecule. We interpret the RRS for H_2^+ as the cumulative sum of frequencies from each v, and it gets affected by the depletion of high lying $v's$. Individual $v's$ will exhibit rotational revival similar to neutral molecules if placed

in an intense laser pulse producing broad J-distribution. Long weak pulses can be useful to obtain a high degree of field-free alignment at rotational revivals by a broad J-distribution and to prohibit depletion of high lying vibrational states. Our study shows that intensity-averaging will not washout revivals. Field-free alignment at revivals is maximum for a 60 fs pulse.

Chapter 6

Kinetic-energy release and angular distributions

6.1 Introduction

After examining the limitations of the aligned model calculations in detail in chapters 3 and 4, we are convinced that to study the behavior of H_2^+ dissociation by laser pulses of any pulse duration, it would be better to perform all the necessary calculations including nuclear rotation. Apart from comparing results with existing models, another more important aspect to theoretical study is to make connections with experimental results. An experimental observable for H_2^+ dissociation is the momentum distribution of p+H. Other observables like angular and kinetic energy release (KER) distributions can be extracted from the momentum distribution. Our study closely relates to an ion-beam experiment performed by Prof. I. Ben-Itzhak and coworkers [15]. A few other groups have also performed experiments involving the interaction of an H_2^+ ion-beam with laser pulses [35, 123–125]. A majority of the experiments, however, start from a neutral H_2 target in a gas jet [126, 127]. Only recently, while using enormous computing resources, theoretical studies have become possible for the H_2 molecule including nuclear vibration and single ionization that would lead to the dissociation of H_2^+ [128]. In most studies, in order to mimic H_2 ionization, a coherent Franck-Condon wavepacket is launched onto the H_2^+ $1s\sigma_g$ channel using the sudden approximation close to the peak of the laser field. This, however, is only an approximation, and thus there is an

ambiguity about preparing the initial state in H_2^+ from single ionization of H_2 in a gas jet experiment. Despite the difficulty in performing an accurate theoretical study, and hence making a direct comparison with the experiment, a neutral target offers a high density target, and all the charged fragments and electron can be detected efficiently using cold-target recoil ion momentum spectroscopy [127, 129]. Gas jet experiments also have additional drawbacks compared to ion beam experiments. There is a clear two-fold advantage of an ion-beam experiment over a gas jet experiment when it comes to getting complete information for H_2^+ dissociation by laser pulses. First, it starts with H_2^+ rather than H_2 and, therefore, removes ambiguity about the ionization time of H_2 in a pulse. Second, in contrast to a gas jet experiment where only the proton can be detected, here both neutrals (H) and ions (p) can be detected in coincidence giving complete information about the dissociation.

So, we take advantage of the availability of experimental results and make a comparison with our results. This leads to a better interpretation and understating of the physics behind different dissociation processes. Specifically, we have performed an extensive study of H_2^+ dissociation in short laser pulses ranging from 5 to 135 fs and compared our results with the experiment for a number of phenomena such as vibrational suppression, zero-photon dissociation (0ω), bond-softening (1ω), and above-threshold dissociation (2ω and 3ω)[1]. It is, however, not always trivial to obtain an experimental observable in a theoretical study. For that, we have developed a careful analysis to obtain the momentum distribution of p+H as explained in Sec. 2.3.7.

6.2 H_2^+ dissociation: Diabatic Floquet-representation to understand KER distribution

Before looking into the specific details of the KER distribution of H_2^+ dissociation for different laser parameters, its behavior can be predicted by looking at the lowest two potential curves of H_2^+ in the diabatic Floquet-representation as described in Sec. 1.3. Many dissociation

[1]The terminology developed for different dissociation processes in Sec. 1.3 will be used.

processes contribute to the KER distribution. From Eq. (2.50), dP/dE is

$$\frac{dP}{dE} = \sum_{L \text{ even}} |a_{L+}(E)|^2 + \sum_{L \text{ odd}} |a_{L-}(E)|^2. \tag{6.1}$$

Using the above expression, we can calculate dP/dE for each initial vibrational state v ($(dP/dE)_v$), and the FC-averaged KER distribution will be :

$$\frac{dP}{dE} = \sum_v f_v \left(\frac{dP}{dE}\right)_v. \tag{6.2}$$

Thus, the total KER-distribution is an incoherent sum of all channels for each v and then a coherent sum of all initial vibrational states.

We have categorized different dissociation processes from their final states as 0ω, 1ω, net-1ω, 2ω and 3ω[2]. Figure 6.1(a) shows the location of 0ω, 1ω, net- 1ω, 2ω and 3ω FC-averaged KER peaks relative to the thresholds. The individual peaks are then combined into the total KER-distribution in Fig. 6.1(b). The widths of individual KER peaks in Fig. 6.1 roughly indicate the v-range contributing to different dissociation processes. For example, $v = 9$ is at the one-photon crossing and dissociates by 1ω, however, $v = 7$–11 can also contribute significantly to 1ω dissociation. The net-1ω peak, however, comes from lower vibrational states such as $v = 2, 3, 4$. Since 1ω and net-1ω contribute to the same energy, it is hard to distinguish between them in the FC-averaged KER-distribution. However, by looking into the individual channels for each v, the net-1ω KER peak can be identified.

Similar to $v = 7$—11 for 1ω, $v = 2, 3, 4$ are most likely to contribute to 2ω and 3ω KER peaks. Finally, for 0ω, $v > 12$ can make the transition to $2p\sigma_u - 1\omega$ and then to $1s\sigma_g - 0\omega$, which should make all the population bound again. However, the bandwidth of the laser can put the tail of this distribution into the continuum. So, there are two reasons for the broadening of each peak: the contribution of many vibrational states, and the bandwidth of the laser.

The peak positions, obtained from the difference of field-free vibrational energy levels and thresholds, are only approximate as the oscillating electric field causes AC Stark shifts

[2] For their correspondence to commonly used terms see Sec. 1.3

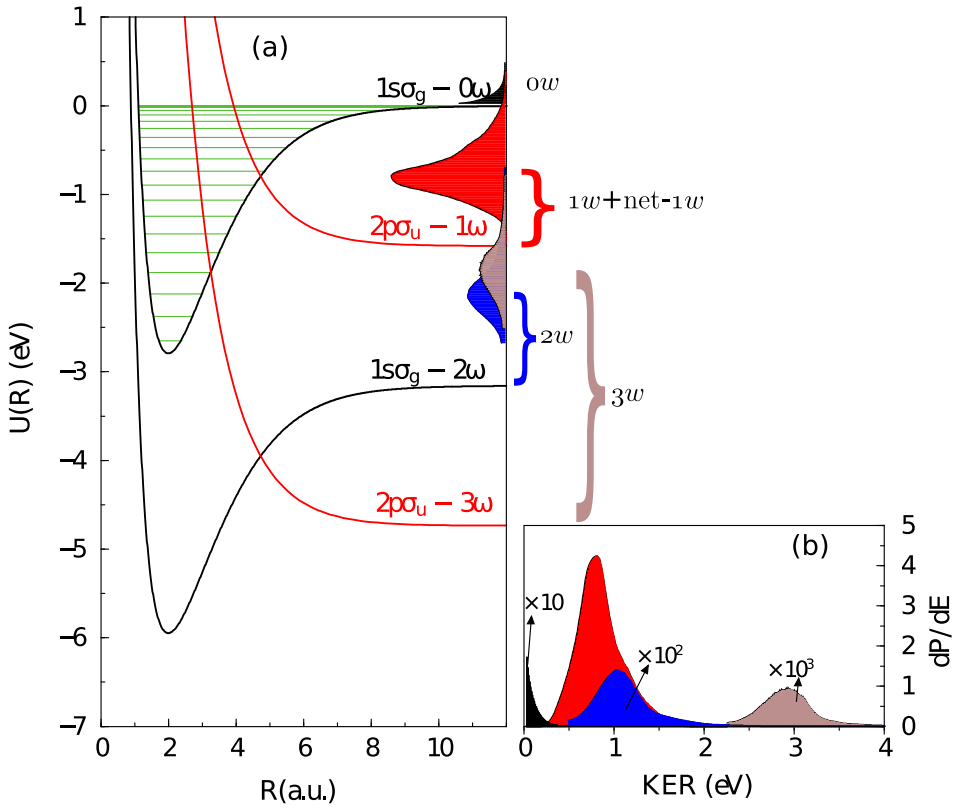

Figure 6.1 (a) Diabatic Floquet potentials with individual FC-averaged 0ω to 1ω KER peaks plotted relative to their respective thresholds. (b) The FC-averaged KER distribution as it will appear on a detector to emphasize the overlap of different dissociation processes from different initial vibrational states overlapping in energy. $I = 3 \times 10^{13}$ W/cm^2 and τ_{FWHM} =10 fs.

of the levels and alters their positions. For example, the energy difference between the 2ω and 3ω peaks is not equal to ω, and this can be attributed to the AC Stark shift. This will become clearer in the following sections. According to perturbation theory, peak heights for different above-threshold ionization peaks in the photoelectron spectrum are proportional to I^n, where n represents the photon number. Figure 6.1 shows, however, a somewhat complicated trend for many photon peaks in H_2^+ dissociation. We see from Fig. 6.1 that 0ω (a two-photon process as it occurs by absorbing and emitting one photon) is an oder of magnitude larger than 2ω. The reason is that the latter is not a direct two-photon process, but depends on the initiation of 3ω, which makes it a higher-order process. Moreover, once the 3ω can occur, strong coupling between $1s\sigma_g$ and $2p\sigma_u$ forces the transition at the two-photon crossing back to the $1s\sigma_g - 2\omega$ channel, further decreasing the 3ω peak by an order of magnitude.

In the following subsections, I will briefly describe the behavior of different photon processes with peak intensity and pulse duration. My focus is to look at some of the individual vibrational states in each case.

6.3 1ω dissociation

For a Ti:Sapphire laser with a 785 nm wavelength, the dominant contribution to the dissociation of H_2^+ would be from 1ω dissociation. All the states with $E_v + \omega - U(R \to \infty) > 0$ will contribute to 1ω dissociation. Here, I will describe the behavior of the KER and angular distributions for $v = 8$, 9, and 10, which lie closer to the one-photon crossing than all other vibrational states.

6.3.1 Kinetic-energy release distribution

The ninth vibrational state of H_2^+ is at the 1ω resonance with the Ti:Sapphire laser frequency, giving the dominant contribution to 1ω dissociation. One-photon resonance means $v = 9$ lies at the 1ω crossing of the field-dressed $1s\sigma_g$ and $2p\sigma_u$ potential curves. The coupling

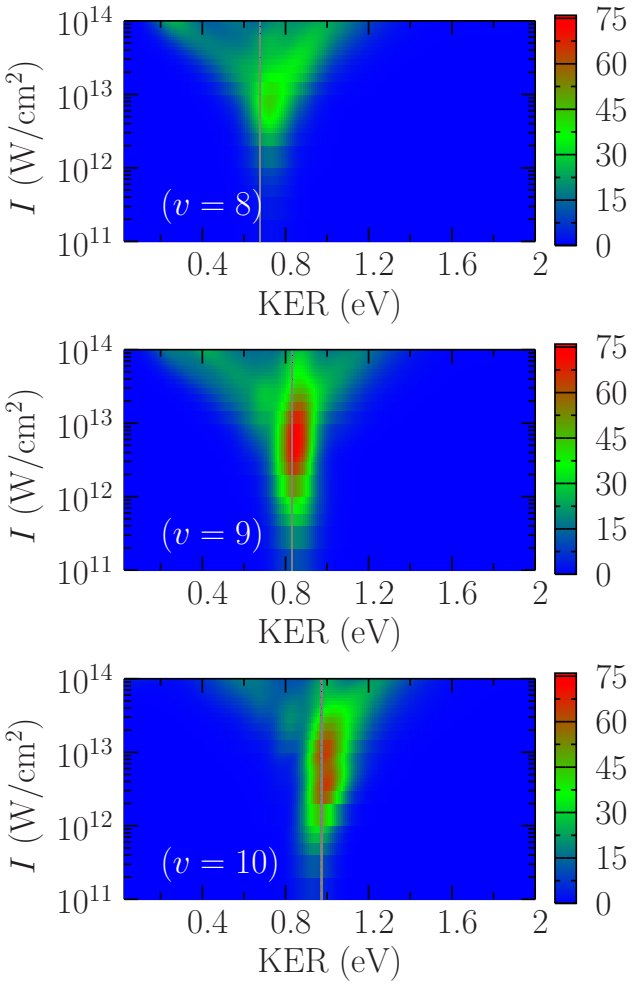

Figure 6.2 Density plots for dP/dE vs I for $v = 8$, 9, and 10 from top to bottom. The gray vertical line in each panel indicates the 1ω peak position calculated from the field-free energy level (E_v). $\tau_{\mathrm{FWHM}} = 10$ fs.

between two channels is strongest at their crossing. The estimated values for the KER peak positions for $v = 8$, 9, 10 are 0.68, 0.83, and 0.97 eV respectively. From Fig. 6.2, we can clearly see that $v = 9$, 10 start dissociating with the expected KER and show a nice single peak without much deviation from the expected KER up to $I \sim 10^{13}$ W/cm^2. In contrast, $v = 8$ always dissociates with higher KER. This is somewhat surprising, because even in the adiabatic representation of field-dressed potentials, vibrational levels would only shift to lower energies for energy levels below the one-photon crossing and thus give smaller energy

for $v = 8$. For all vibrational states, the KER distribution shows rich complicated structure for higher intensities, as the single peak fans out into several peaks distributed in high and low KER. The dominant peaks for $v = 8$ and 9 move towards higher KER, but for $v = 9$ the shift is not very large.

6.3.2 Angular distribution (AD)

Another interesting question is "Can we predict the angular distribution (AD) of 1ω dissociation?" A common answer is that the parallel component of the field for a linearly polarized laser is responsible for the dissociation. So, for short pulses, the molecule at an angle θ sees an effective peak intensity $I_{\text{eff}} = I\cos^2\theta$, giving a $\cos^2\theta$ AD[3]. Some discussion about AD has already been included in Chap.4 to check the validity of the axial-recoil approximation, and also a comparison was done with an effective-field model for the FC-averaged AD. Here, the main focus is to study AD for individual v's, as the total AD contains contributions from multiphoton dissociative pathways from all vibrational states, which are not expected to behave like $\cos^2\theta$.

According to perturbation theory, $dP/d\theta \propto \cos^{2n}\theta$, in an analogy to multiphoton ionization of atoms, where the ionization probability is $\propto I^n$ for an n-photon ionization [36]. In our theoretical formulation in Sec. 2.3.7, we expect the AD to be a linear combination of all populated partial waves after the field is off. This is valid independent of the laser parameters. For example, an initial $J = 0$ in $1s\sigma_g$, within first-order perturbation theory, can only populate $J = 1$ in $2p\sigma_u$ to give dissociation (1ω), giving a $\cos^2\theta$ AD, thus all models predict $\cos^2\theta$ AD for 1ω at lower intensities. Figure 6.3 shows the AD for $v = 8$, 9, 10 for three I's[4]. All vibrational states clearly show a $\cos^2\theta$-distribution for $I = 10^{11}$ W/cm^2. However, as the I grows the AD significantly deviates from $\cos^2\theta$ and especially for $I = 10^{13}$ W/cm^2 the interference of many partial waves gives a very complicated AD structure. I should mention that these v's populate up to 18 J's for $I = 10^{13}$ W/cm^2. It would be hard to interpret

[3] In this chapter $\theta \equiv \theta_K$

[4] All angular distributions shownd are renormalized to unit peak position

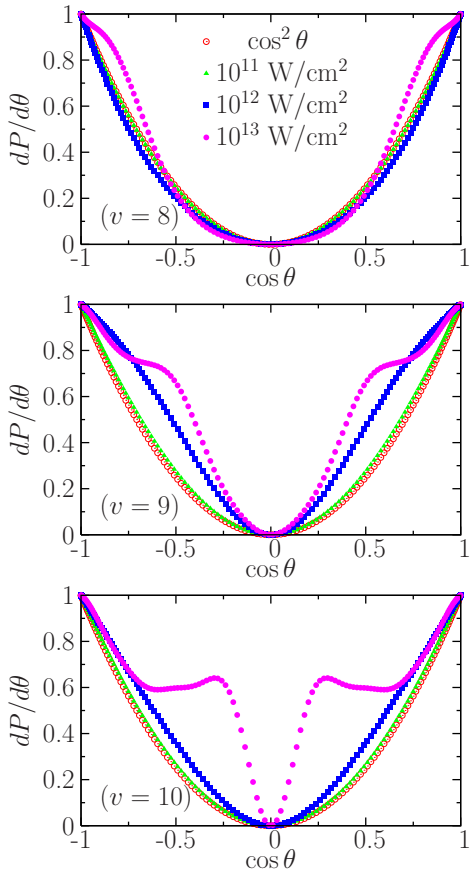

Figure 6.3 $dP/d\theta$ for selected I for $v = 8$, 9, and 10 from top to bottom. $\tau_{\mathrm{FWHM}} = 10$ fs.

the AD for higher intensities, given that it already shows complexity for $I = 10^{13}$ W/cm^2, where these v's have well-defined 1ω peaks in KER (see Fig. 6.2). For well-defined 1ω peaks in KER, we can expect a simple angular distribution, but it is evident from Fig. 6.3 that this is not the case.

6.4 Net-1ω, 2ω and 3ω dissociation

Contrary to 1ω dissociation, net-1ω, 2ω and 3ω dissociation offer complexity in KER and angular distributions by being not only multiphoton processes but also because these occur through complex pathways in H_2^+ potential curves. Similar to the previous section, to get some insight, we will discuss the KER and angular distributions of $v = 2$, 3, and 4.

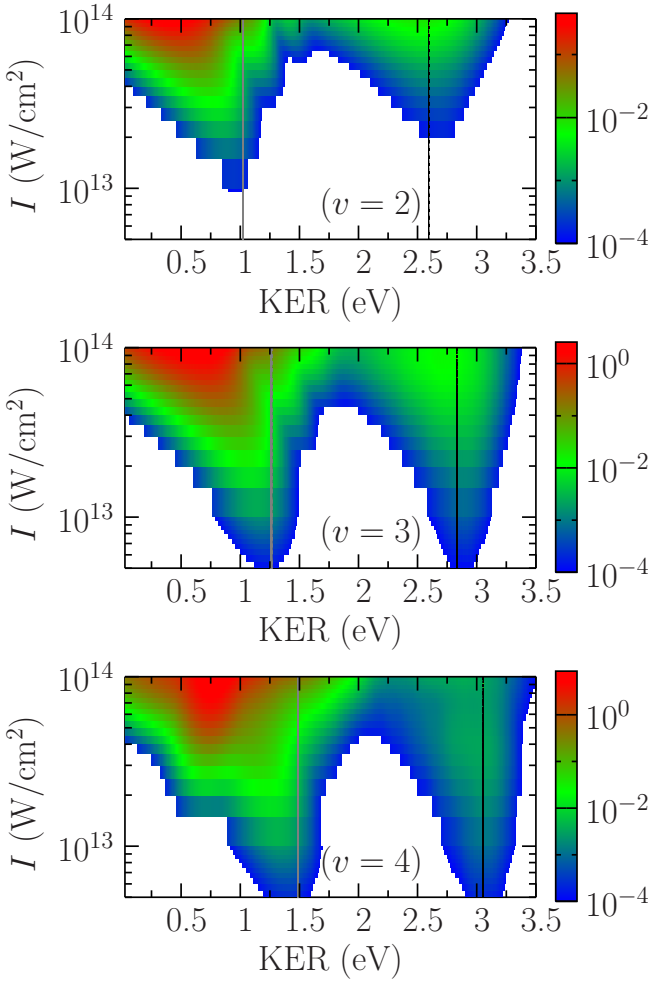

Figure 6.4 Density plots for dP/dE vs I on log-scale for $v = 2$, 3, and 4 from top to bottom. In each panel, a gray vertical line indicates 2ω and a black vertical line indicates 3ω peak positions calculated from field-free energy levels (E_v). $\tau_{\mathrm{FWHM}} = 10$ fs.

6.4.1 Kinetic-energy release distribution

For all the intensities in our theoretical study, net-1ω, 2ω and 3ω dissociation remains small in absolute numbers as evident from Fig. 6.4. At very low intensity, the 2ω and 3ω peaks emerge with KER close to the expected value calculated using field-free E_v. However, we see a curious large shift in the 2ω peak towards low KER with I as compared to the 3ω peak. Figure 6.4 shows that the 3ω peak has a negligible shift with I. Similar to 1ω dissociation, 2ω also becomes broader with I. In this case, however, the spread in the low KER peak is

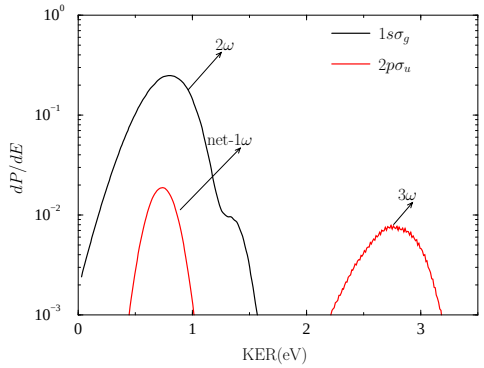

Figure 6.5 KER distribution with for $v = 3$ from each channel; $I = 5 \times^1 0^{13}$ W/cm^2, $\tau_{\mathrm{FWHM}} =$ 10 fs.

only partly from 2ω, as net-1ω also occurs with low KER (see Fig. 6.5)[5]. Net-1ω dissociation emerges at very low KER and then shifts towards high KER with I. It becomes comparable to the 2ω peak for $I > 4 \times 10^{13}$ W/cm^2 for $v = 4$ making the low KER peak significantly broader in this intensity range. Comparing Figs. 6.2 and 6.4, we find that the 2ω peak shift with intensity is much larger than 1ω, and the peaks shift towards low KER, while the 1ω peak shift is towards higher KER. This suggests that the emergence of low energy contribution for a given I in the KER-cos θ plots would be because of the contribution from 2ω and does not represent a shift in the $v = 8$ 1ω peak as described in Ref. [15].

Observing clear peaks in KER for 3ω dissociation of H_2^+ is a non-trivial problem, in contrast to above-threshold ionization peaks in the photoelectron spectrum for atomic ionization. The major problem that prohibits this observation is the broad vibrational state distribution, which can dissociate by different photon processes with similar KER, making it impossible to distinguish between different peaks. Even for individual vibrational states, 2ω cannot be separated from net-1ω in an experiment[6]. The other important reason is the dipole coupling between $1s\sigma_g$ and $2p\sigma_u$ channels at the two-photon crossing, which causes a transition from the higher order 3ω dissociation to the lower order 2ω dissociation, thus

[5] Wiggles on the 3ω peaks are numerical and due to the choice of our grid as briefly mentioned in Sec. 2.5. Using a more optimal grid removes these wiggles without changing the peak position and height significantly (see Fig. C.2 for comparison).

[6] In a theoretical study, this is possible as the two processes occur in different electronic channels.

suppressing the former. We can enhance 3ω dissociation by using either pulses shorter than 10 fs, or D_2^+ [4]. Figure 6.6 shows clear enhancement of 3ω dissociation (from 2.5 to 3 eV) with pulse duration.

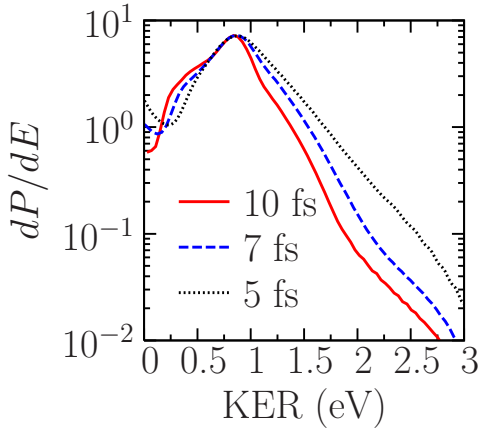

Figure 6.6 FC-averaged dP/dE for three different pulse lengths. $I = 10^{14}$ W/cm^2.

6.4.2 Angular distribution

Now, we will check whether or not the AD for 2ω and 3ω peaks follow a $\cos^{2n}\theta$-distribution. The AD for only the 2ω peak, however, cannot be obtained because it overlaps with the net-1ω peak. From Eq. (2.49), we see that integration over energy does not eliminate the coherence of different channels in the angular distribution. If there is no net-1ω, then $\rho(E,\theta)$ can be regarded as an incoherent sum of $1s\sigma_g$ and $2p\sigma_u$ to a good approximation, and the AD for both 2ω and 3ω peaks can be obtained from each channel respectively. The presence of net-1ω makes $\rho(E,\theta)$ a coherent sum of the two channel's contributions and thus prohibits calculating AD for 2ω [see Eq. (2.49)]. It is this interference between 2ω and net-1ω that leads to an up-down asymmetry (along the laser polarization) of the p+H momentum distribution. This will be discussed in detail in Chap. 7. Angular distributions for 3ω peaks are calculated by integrating $\rho(E,\theta)$ over E from 1.8, 2.0, and 2.2 eV to 4 eV for $v = 2$, 3, and 4 respectively.

We do not see $\cos^6\theta$ behavior for any AD plotted in Fig. 6.7. However, a surprising

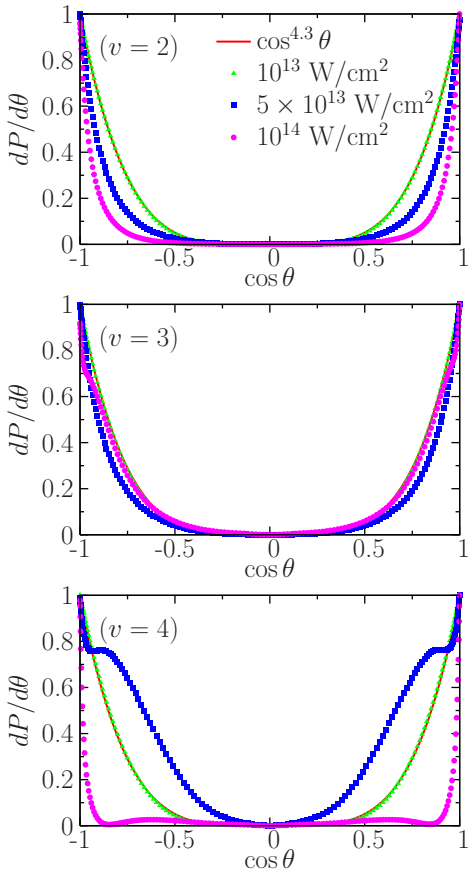

Figure 6.7 $dP/d\theta$ for selected I for $v = 2$, 3, and 4 from top to bottom; $\tau_{\mathrm{FWHM}} = 10$ fs.

$\cos^{4.3}\theta$ fits the AD very well for $I = 10^{13}$ W/cm^2 for all v's in Fig. 6.7. The angular distribution for $v = 2$ becomes sharply aligned with increasing I, however it shows complicated behavior with I for the other two cases. Besides the curious behavior of $\cos^{4.3}\theta$ at $I = 10^{13}$ W/cm^2, there is no simple interpretation of the shape of the AD for $v = 2$, 3, and 4. We can only say it is a linear combination of many partial waves contributing to the dissociation. Our calculations show 19, 23, and 27 J's are populated for $v = 2$, 3, and 4, respectively, for the highest I shown in Fig. 6.7.

6.5 0ω dissociation

Historically, Posthumus *et al.* used the phenomenon of 0ω dissociation to explain fragments which dissociate with very low kinetic energy [58]. The interpretation was based on the

vibrational trapping of the population in the well created in field-dressed adiabatic potential curves, and then tipping over the population nonadiabatically on the rising edge of the pulse (see Sec. 1.3 for more detail). In a recent study by Posthumus *et al.* [130], however, the phenomenon known as resonance-enhanced multiphoton ionization is proposed instead for the creation of low energy fragments. Note that both of these experiments start from the neutral H_2 molecule, and hence the dissociation of H_2^+ takes place essentially after the single ionization of H_2 into H_2^+ by the leading edge of the field. So, in their first study [58], the possibility of multiphoton transitions to H_2 excited states was not considered, however, in the more recent experiment, it has been shown that transition of excited electronic states of neutral H_2 occurs and later the molecule can stretch and absorb another photon to dissociate directly into the $2p\sigma_u$ channel of H_2^+ with low KER [130].

Now, the question arises: "Does 0ω dissociation exist in H_2^+ and how does it happen?" To answer this question, a first important step would be to start the experiment from H_2^+ rather than H_2 to eliminate resonance-enhanced multiphoton ionization, that is, perform an ion-beam experiment. The signature of 0ω dissociation would be the existence of very low energy fragments. Experimental evidence for 0ω dissociation will come in Sec. 6.6.2. Here I will briefly describe the behavior of individual vibrational states contributing to 0ω specifically, the discussion will include $v = 13$, 14, and 15.

6.5.1 Kinetic-energy release distribution

Near 0 eV, a peak starts emerging first for $v = 15$ at about $I = 5 \times 10^{12}$ W/cm^2, as this vibrational state lies closer to the dissociation threshold. The other two vibrational states contribute to 0ω at a relatively higher intensity of about $I = 3 \times 10^{13}$ W/cm^2 (see Fig. 6.8). So, theoretical results show a clear signature of the presence of 0ω in H_2^+ dissociation by short laser pulses. Figure 6.8 also shows the 1ω peak for $v = 13$, 14, and 15. The One photon peak for these vibrational states show similar behavior to that of $v = 8$, 9, and 10. Pulse-length dependence of 0ω can be seen from Fig. 6.6. Because of the large bandwidth,

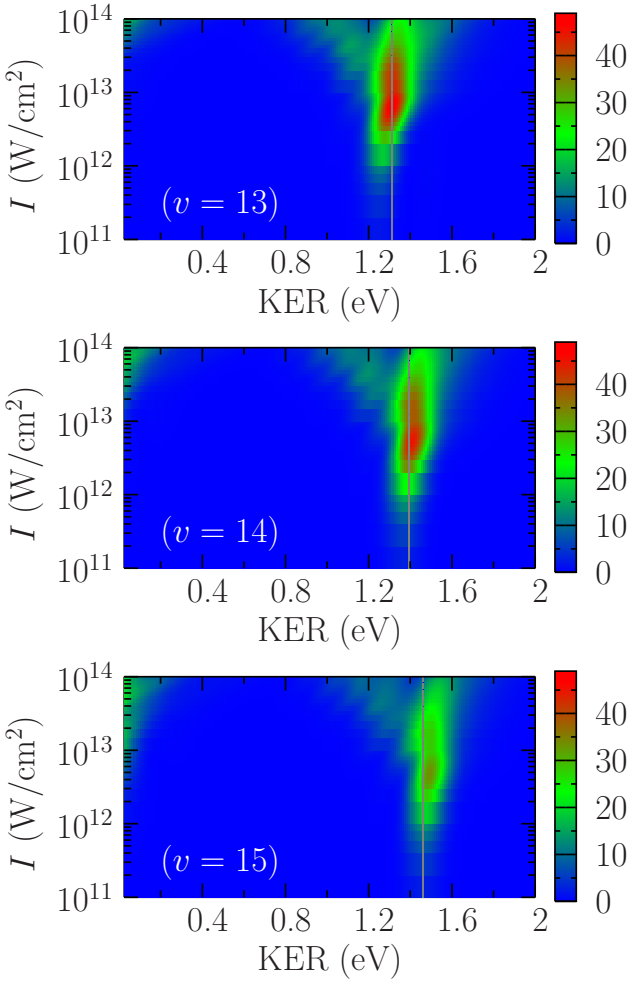

Figure 6.8 Density plots for dP/dE vs I for $v = 13$, 14, and 15 from top to bottom. In each panel, the gray vertical line indicates 1ω calculated from the field-free energy level (E_v). $\tau_{\mathrm{FWHM}} = 10$ fs.

shorter pulses give large 0ω dissociation.

6.5.2 Angular distribution

In this case, the AD can be expected to show $\cos^4\theta$ behavior because it is a two-photon (net zero-photon) process. Perturbatively, however, for an initial $J = 0$, the AD would be at least a linear combination of two spherical harmonics Y_{00} and Y_{20}. Clear separation between the ZPD and 1ω peaks in the KER distribution enables us to calculate the AD (see Fig. 6.8). Angular distributions for $v = 13$, 14, and 15 are obtained by integrating

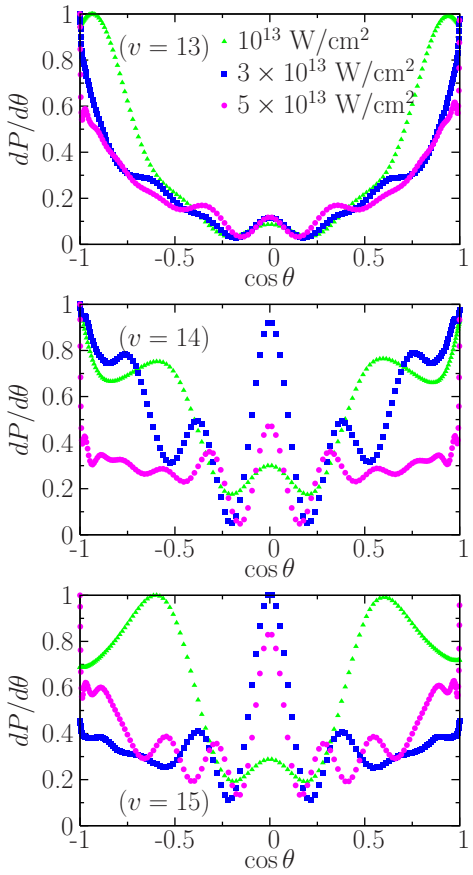

Figure 6.9 $dP/d\theta$ for selected I for $v = 13$, 14, and 15 from top to bottom. $\tau_{\mathrm{FWHM}} = 10$ fs.

$\rho(E, \theta)$ up to $E = 0.4$ eV. Figure 6.9 show ADs for $v = 13$, 14, and 15 corresponding to the 0ω distribution. Angular distributions show complicated structure in almost all cases. For $v = 14$ and 15, the AD's have a large peak perpendicular to the laser polarization for $I = 3 \times 10^{13}$ W/cm^2 and 5×10^{13} W/cm^2. Similar to previous cases, interference among many partial waves would be responsible for the complex structure in angular distributions. For $I = 5 \times 10^{13}$ W/cm^2, 30, 29, and 28 J's are populated for $v = 13$, 14, and 15 respectively.

6.6 Qualitative comparison of theoretical and experimental results

Here, I will first describe the experimental setup used in an ion-beam experiment. In a later section, I will present a comparison of KER-$\cos\theta$ plots and KER-distributions between

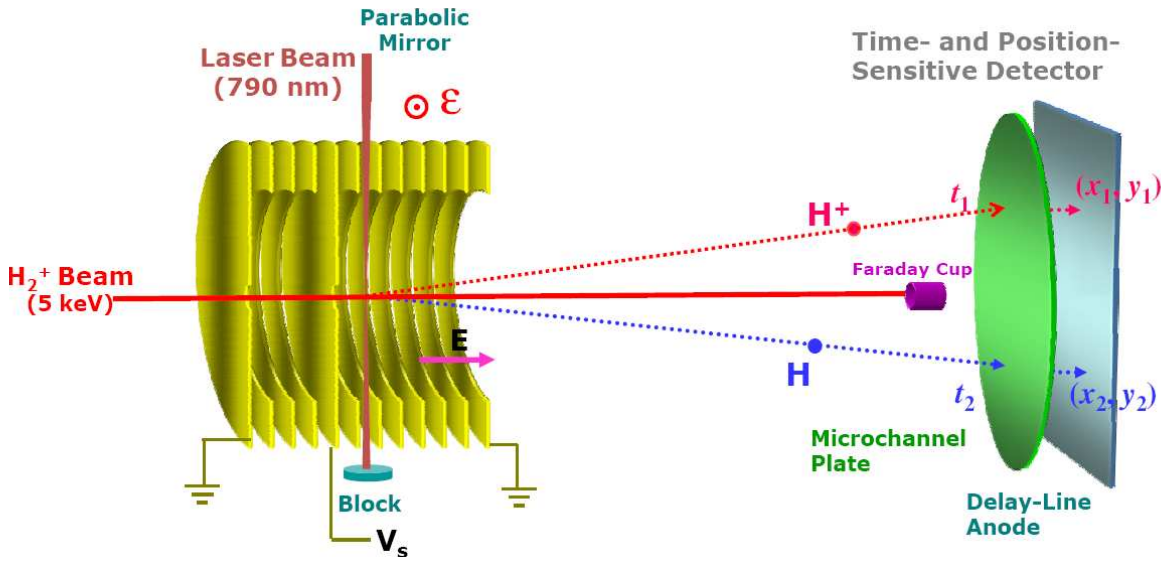

Figure 6.10 Experimental set up for dissociation of H_2^+ ion beam by laser pulses [15]. Figure is adapted from Ref. [15].

theory and experiment.

6.6.1 Experimental geometry and spatial intensity distribution of the pulse

As mentioned earlier, wherever possible, theoretical and experimental results are compared. Experiments are performed by crossing the molecular ion beam with a laser pulse and detecting both neutral and charged fragments in coincidence using a time and position sensitive detector. Figure 6.10 shows the set up used in the experiment. Specific details about the experimental techniques can be found in [15, 36, 79, 131].

Without going into further details of the experimental set up, I would like to mention an important point about the geometry of this set up for the spatial distribution of the focused laser pulse. In the experimental observation, all the molecules do not dissociate by the laser peak intensity. Rather, a large fraction of the signal comes from the lower intensities in the focal volume of the laser. So, to be able to have a meaningful comparison between experiment and theory, theoretical results should be averaged over the focal volume of the laser. The ion beam dimension helps somewhat with this averaging. For this case, instead

of doing three-dimensional averaging, two-dimensional averaging would be sufficient [21].

Here, I describe some of the consequences of focal volume averaging: (i) the relative signal for higher order ATD, which occurs only at higher intensities, compared to the 1ω signal, becomes very small, (ii) the problem (i) can be compensated for by increasing I to increase the effective volume for the higher intensities. However, this can cause H_2^+ ionization, making theoretical study difficult as it is not included in our formulation (10^{14} W/cm^2 is the limit for a 10 fs pulse), (iii) a trivial problem is that many calculations have to be performed to do focal volume averaging which is not efficient compared to the time for calculations at a single peak intensity.

To make reasonable comparisons with experiment, we have adopted two approaches:

- Perform focal volume averaging by using the following relation for any observable $O(I)$

$$O(I_0) \propto \int_0^{I_0} \frac{O(I)}{I} dI \tag{6.3}$$

  The factors to remove the proportionality in the above expression [131–133] depend on the focusing geometry and sometimes cannot be determined precisely in an experiment. Moreover, these factors keep changing with the experiment and give just an overall factor. Since the measurements are not absolute, these factors are not important.

- Sometimes, we made a choice to not do intensity averaging, but rather performed calculations at somewhat lower intensity than the experiment assuming that the effect of focal volume averaging is to merely change the effective peak intensity. While this approach is not accurate, it requires many fewer calculations and can be very useful to build qualitative understanding.

6.6.2 Experimental setup to detect near 0 eV fragments

In the experimental set up shown in Fig. 6.10, we can see that all the neutral fragments with very low KER would strike the Faraday cup placed to catch the H_2^+ ion beam. To avoid this from happening, Ben-Itzhak and co-workers developed a new scheme to precisely

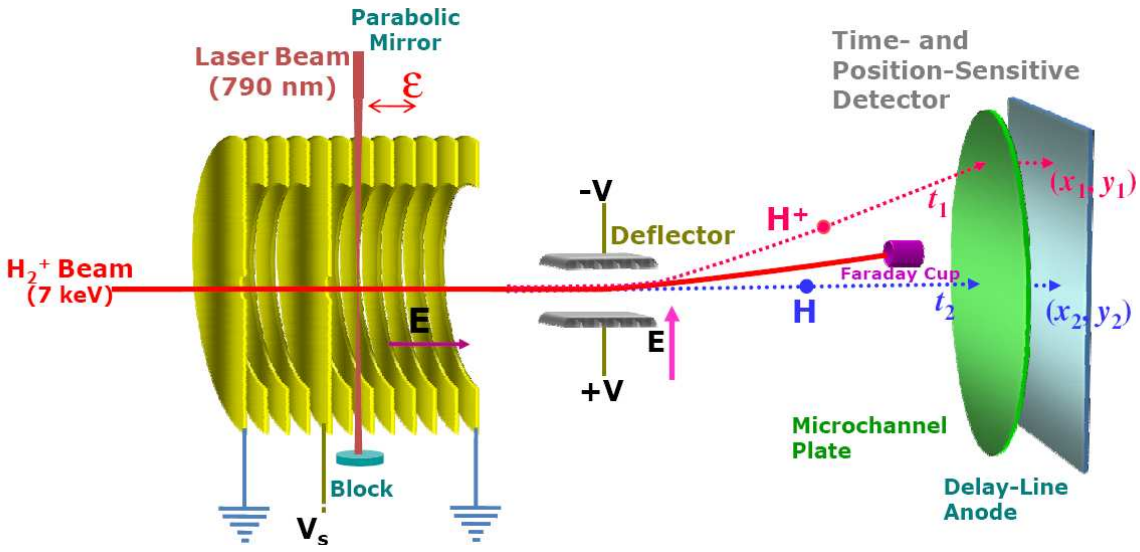

Figure 6.11 The experimental set up to observe very low KER fragments in H_2^+ dissociation. Figure is adapted from Ref. [11].

observe very low energy fragments. This new setup is shown in Fig. 6.11 [11]. In this setup, the H_2^+ beam is deflected by applying a high voltage, thereby separating it from low energy dissociating fragments. The scheme was successfully implemented to confirm 0ω dissociation [11].

6.6.3 Experimental and theoretical results

Efforts are underway to perform quantitative comparison between experimental and theoretical results. This requires thermal averaging, convolution with respect to experimental resolution, and a realistic pulse shape in addition to Franck-Condon and focal-volume averaging. It would take about 500,000 cpu hours to do thermal averaging from $J = 0$ to 10, for a 10 fs pulse and peak intensities up to 10^{14} W/cm^2. We are in the process of doing such calculations, but I will show here only the initial $J = 0$ results which we already have.

Figure 6.12 shows KER-$\cos\theta$ plots for three peak intensities. Theoretical results shown in Fig. 6.12 are intensity averaged to make them more comparable to the experiment. The agreement between experiment and theory, though still qualitative, is remarkable. We see a clear 1ω peak which starts developing an aligned "nose" at low KER with I, from the 1ω

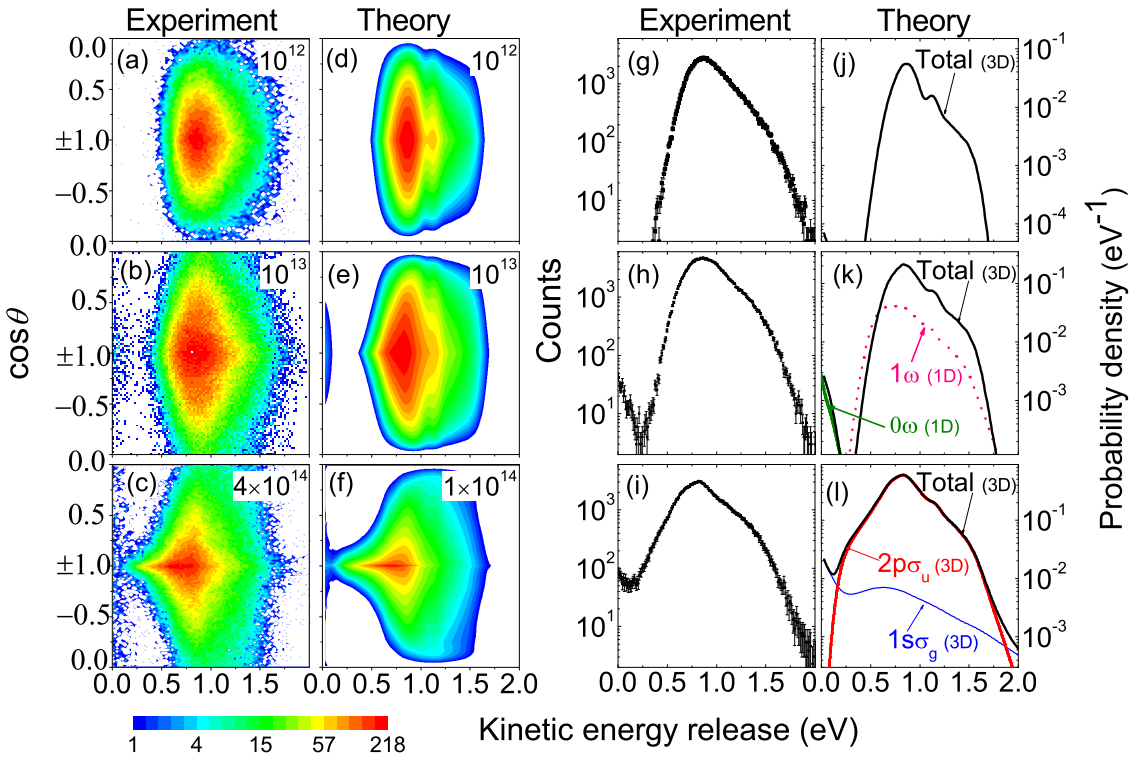

Figure 6.12 Experimental and theoretical KER-cos θ plots (two left columns) and KER-distributions (two right columns) for a 10 fs pulse with peak intensity of 10^{12} W/cm^2 top and 10^{13} W/cm^2 middle row. In the bottom row intensity is 10^{14} W/cm^2 for theoretical results, however, experimets has a different intensity of 4×10^{14} W/cm^2; $\tau_{\mathrm{FWHM}} = 10$ fs. Figure is adapted from Ref. [11].

dissociation of $v = 5$ and 6, and also the 2ω dissociation of $v = 2$, 3, and 4. The lowest two vibrational levels have a negligible dissociation for these intensities. We can only see a hint of a high KER tail in the KER-cos θ plots for the higher intensity of 10^{14} W/cm^2, as the focal volume averaging suppresses the signal from 3ω dissociation. Similar to our earlier discussion, we see that at $I = 10^{12}$ W/cm^2 no zero energy fragments appear, and then some fragments appear as a distinct peak with zero KER for a moderate intensity of 10^{13} W/cm^2. For the highest intensity shown, zero KER and higher KER population can no longer be distinguished as separate peaks, as the 2ω peak shifts significantly towards low KER with I (see Fig. 6.4). Moreover, features like a broader AD for the 1ω peak at $I = 10^{12}$ and 10^{13} W/cm^2 and the narrowing of the peak with intensity also compare well between

experiment and theory.

Figures 6.12(g)-(l) also shows KER distributions for different intensities after integrating the density over all angles. Comparing KER distributions confirms the conclusions already established for 1ω and ATD. Particularly, in Fig. 6.12(right panels), a zero energy peak can be seen clearly in both experiment and theory.

6.6.4 Suppressed dissociation of H_2^+ vibrational states by reduced dipole coupling

The curious suppression in the dissociation of the twelveth vibrational state was briefly discussed in Sec. 3.4. By looking into the dipole matrix elements $\mathcal{D}_v(E)$ for this state, we found that the suppression results from a minimum in $\mathcal{D}_v(E)$ for KER=$E_{12}+\omega-U_{R\to\infty}$. Dipole matrix elements show structure with KER for all vibrational states and, therefore, suppression would occur for different vibrational states for different laser frequencies as predicted from first-order time-dependent perturbation theory in Sec. 3.4.

In reality, many laser-molecule experiments are performed in the strong-field non-linear ($\gtrsim 10^{12}\,\mathrm{W/cm^2}$) regime. Thus, for the predictions of perturbation theory to be useful they must survive to high intensities. Since the dipole matrix elements determine the multi-photon transition rates, this is expected. Nonetheless, to explore the robustness of the dissociation suppression, we performed calculations for higher, non-perturbative intensities. As ionization is omitted from the theory, we limit the intensities explored to below the onset ionization.

Figure 6.13(a) shows the KER distribution of H_2^+ (integrated over all angles) calculated using our intense-field theory for 790 nm, 45 fs, $4\times10^{12}\,\mathrm{W/cm^2}$ pulses, after Franck-Condon averaging. Distinct peaks are observed corresponding to one-photon dissociation of the v states as indicated by the vibrational-comb ticks along the top of the plot, calculated from the field-free vibrational energies. The corresponding (non-weighted) P_D for each v state is shown in Fig. 6.13(c) along with the perturbation theory calculation. Clearly, a reduction in P_D of v=12 with respect to the neighboring states is predicted by the intense-

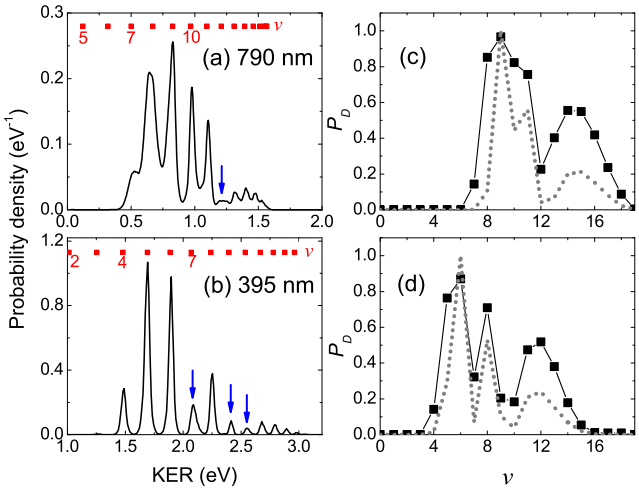

Figure 6.13 Calculated kinetic energy release (KER) distributions of H_2^+ using 45 fs, 4×10^{12} W/cm^2 pulses at (a) 790 nm, and (b) 395 nm. Vibrational comb ticks for one-photon dissociation are shown along the top of the panels. The corresponding dissociation probabilities P_D are shown in (c) 790 nm and (d) 395 nm (solid points), as well as normalized perturbation results (dashed lines). Figure is adapted from Ref. [12].

field calculation, with the perturbation result in good qualitative agreement. This v=12 suppression can also be found in the KER distribution in Fig. 6.13(a) by a dip (see arrow) at the v=12 KER value (1.2 eV), and the magnitude of the dip suggests that it should be measurable experimentally. Our calculations further reveal that the dissociation suppression persists at intensities at least up to 10^{13} W/cm^2 (the highest that we tested for 45 fs, and 10^{14} W/cm^2 for 7 fs) — albeit gradually reducing in contrast — and thus survives intensity-averaging due to the laser focal volume in an experiment. It is also present for all pulses that we have explored in the range 5 – 170 fs. Moreover, since our calculations account for nuclear rotation, these results show that this dissociation suppression is not washed out by rotation, unlike intensity-dependent stabilization and dynamical dissociation quenching as discussed in Chap. 3.

As a check to ensure that the dissociation suppression is also measurable at other wavelengths, we repeated the calculations at 395 nm, the second-harmonic of a 790 nm Ti:Sapphire laser. The KER distribution and P_D results are shown in Figs. 6.13(b) and

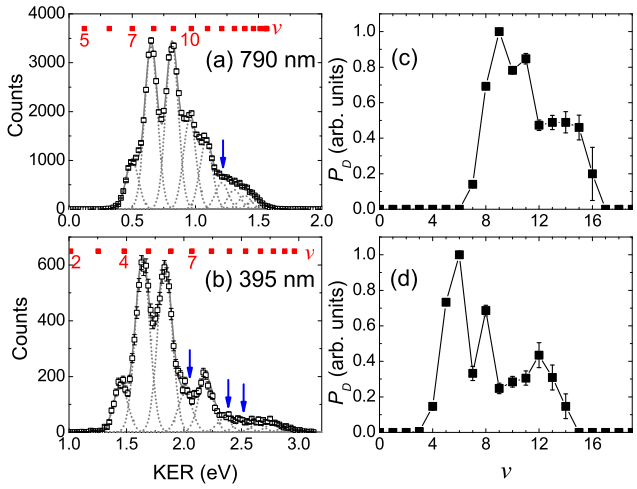

Figure 6.14 Experimental kinetic energy release (KER) distributions of H_2^+ using 40 fs, 3×10^{13} W/cm^2 pulses at (a) 790 nm, and (b) 395 nm. Vibrational comb ticks for one-photon dissociation are shown along the top of the panels. Error bars denote the statistical uncertainty. The corresponding relative dissociation probabilities P_D are shown in (c) 790 nm and (d) 395 nm. Error bars are a sampling estimate of the uncertainty from the fitting procedure. Figure is adapted from Ref. [12].

6.13(d), respectively. Significant suppression is observed for v=7, 9 and 10, in agreement with the perturbation calculation. As with 790 nm, these suppressions can be seen in the KER distribution as amplitude dips at KER values of 2.1, 2.4 and 2.6 eV, respectively. Thus, the suppression does indeed persist for other wavelengths as predicted in Sec. 3.4.

A crucial check of this dissociation suppression is if we can observe it in the laboratory. For this purpose, McKenna and co-workers conducted the experiment for H_2^+ dissociation using the setup described in Sec. 3.4. The measured KER dissociation spectra of H_2^+ using 40 fs, 3×10^{13} W/cm^2 pulses at 790 nm and 395 nm are shown in Figs. 6.14(a) and 6.14(b), respectively. The spectra are plotted for a $\pm37^\circ$ angular cut along the laser polarization to help reduce the effects of intensity-averaging. Reasonably well resolved structures are observed at both wavelengths. The resolution is mostly limited by the position-sensitive detector (delay-line anode) resolution. These structures come from one-photon dissociation of H_2^+ v states and agree well in KER with the field-free vibrational-comb energies (see ticks on plots).

To extract the relative P_D values for the different v states, we fit each of the peaks with Gaussian distributions as shown by the dashed curves in Figs. 6.14(a) and 6.14(b). The widths of all the Gaussians are fixed for each wavelength (FWHM=0.12 eV for 790 nm; FWHM=0.15 eV for 395 nm) to limit the number of free parameters. Also, their KER positions are restricted to a downward shift of <3% from the field-free vibrational energies. This small KER shift is likely to be caused by a systematic energy calibration uncertainty from our imaging setup. Essentially, the main remaining parameter is the amplitude of each peak, which is adjusted to give the best overall fit (solid curve) to the data. The integrated area of each Gaussian distribution is then divided by the fractional Franck-Condon population of that v state to give the relative P_D value. The results are shown in Figs. 6.14(c) and 6.14(d) for 790 nm and 395 nm, respectively.

At 790 nm, a reduction in P_D around v=12 is observed. This suppression was predicted by our intense-field theory, and importantly, also by perturbation theory underscoring its usefulness [Fig. 6.13(c)]. Similarly, 395 nm shows a reduction for v=7 and around v=9–11, again in good correspondence with our theory [Fig. 6.13(d)]. Overall, comparison of the theory and experiment in Figs. 6.13 and 6.14 show remarkable similarities in both the KER distributions and the P_D plots despite the pulse durations, intensities (and intensity-averaging) and angular integration range all differing — in addition to the uncertainty from the experimental fitting procedure. The observed suppression in Fig. 6.14 is clear evidence that the suppression effect from the dipole coupling is measurable even in the non-perturbative regime.

Chapter 7

Controlling asymmetry in momentum distribution

7.1 Introduction

In this chapter, my discussion will focus on the momentum distribution of the dissociating fragments. In recent experiments involving H_2^+ dissociation, the momentum distribution of p+H is the most differential observable [4][15, 79]. A state selective momentum distribution would be more differential, however, since H_2^+ has an initial distribution of rovibrational states both in an ion-beam and neutral gas target. From Eqs. (2.49) and (2.48) the momentum distribution $\rho(\mathbf{K})$ is

$$\rho(\mathbf{K}) = \rho(E,\theta)\sqrt{\frac{2E}{\mu}} = \sqrt{\frac{2E}{\mu}}\left| s_+ \sum_{L \text{ even}} (-i)^L Y_{Lm_L}(\hat{K}) e^{-i\delta_{EL+}} \langle EL+|F_{L+}(R,t_f)\rangle - \right.$$
$$\left. s_- \sum_{L \text{ odd}} (-i)^L Y_{Lm_L}(\hat{K}) e^{-i\delta_{EL-}} \langle EL-|F_{L-}(R,t_f)\rangle \right|^2 . \tag{7.1}$$

Similar to the work done in Ref. [73], Eq. (7.1) shows that the momentum distribution $\rho(\mathbf{K})$ is the coherent sum of $1s\sigma_g$ and $2p\sigma_u$. In some of the previous studies, the up-down KER-distribution is studied instead of the momentum distribution as nuclear rotation was not included [134–136]. Now, each molecular channel in $\rho(\mathbf{K})$ exhibits a symmetric momentum distribution as it contains only even (for $1s\sigma_g$) or odd (for $2p\sigma_u$) partial waves. But the interference of even and odd partial waves from these channels will give an up-down asymmetry in the momentum distribution. The laser field is vertical and thus up means

along the field. Equation 7.1 shows that interference occurs when both channels contribute to the same energy. Asymmetry depends on the laser parameters as it is determined by the phase of the amplitudes $\langle EL+(-)|F_{L+(-)}(R,t_f)\rangle$. In Sec. 6.4, we discussed that two-photon and below-threshold dissociation (net one-photon) KER-distributions overlap in energy, and thus can give asymmetry in the momentum distribution. To avoid confusing notation, I will use "net-0ω" for zero-photon dissociation, "1ω" for bond-softening or one-photon dissociation, "2ω" and "3ω" for above-threshold dissociation (ATD) according to their respective energy range, and "net-1ω" for below-threshold dissociation.

Generally, the interference of different pathways to the same energy causes asymmetry in the momentum distributions of photoelectrons in the ionization of atoms and molecules and of fragments in ionizations and dissociation of the molecules. Its dependence on the carrier-envelope phase (CEP) of few-cycle laser pulses is the topic of many theoretical and experimental studies [45, 136–140]. For a Gaussian laser field,

$$\mathcal{E}(t) = \mathcal{E}_0 e^{-t^2/\tau^2} \cos(\omega t + \varphi), \tag{7.2}$$

and φ is the carrier-envelope phase. The earlier work of Paulus [137] for CEP effects was about the left-right asymmetry in the above-threshold ionization of atoms. Since then, this effect has been discussed to characterize the CEP of the pulses [141]. Apart from the asymmetry in the momentum distribution, CEP also affects the total dissociation probabilities of H_2^+ and HD^+ [139]. Moreover, CEP affects high harmonic generation [142]. Some recent studies involve the CEP effects on photoexcitation and total ionization of alkali atoms [143]. Carrier-envelope phase-locked pulses have an important application in generating attosecond pulses [144, 145].

Asymmetry in the momentum distribution of p+H is also commonly referred to as up-down asymmetry and electron localization. Both of these terms mean the asymmetry in the momentum distribution. Up-down asymmetry becomes lower by using a more massive hydrogen molecule, that is, D_2^+ [136]. Electron localization can also be controlled as a function of phase between the components of a two-color laser field [73, 134, 135]. Up-down

asymmetry can also be achieved in H_2^+ or D_2^+ dissociation as a function of time delay between an attosecond pulse and infrared field and also the CEP of the infrared field [22, 146], where one or more attosecond pulses are used for an early excitation of the initial wave function in the $1s\sigma_g$ channel. The origin of the asymmetry in the momentum distribution by a single pulse or by the combination of a few and CEP effects in the total probabilities can be interpreted in all cases as an interference between the different pathways contributing to the same energy [44].

Despite the recent advances in producing carrier-envelope phase controlled few cycle laser pulses, measuring CEP effects in the dissociation of diatomic molecules remains a challenging task for experimentalists. To date only a few successful measurements of CEP effects have reported an asymmetry in the momentum distribution of dissociative single ionization of D_2 [45, 147]. While the prediction of asymmetric break up of HD^+ and H_2^+ as a function of CEP was made a few years ago [139], successful measurements have not been made to test these predictions starting directly from these molecular ions, for example in an ion beam experiment [79]. And the question still remains, *"How does nuclear rotation effect up-down asymmetry?"*, as all the theoretical calculations for few cycle pulses have been performed using the aligned model.

7.2 Role of nuclear rotation in CEP effects

Up-down asymmetry arises from the interference of the $1s\sigma_g$ and $2p\sigma_u$ contributions. Thus an intuitive way to predict asymmetry is to look at the branching ratios of these channels in the total dissociation probability P_{D}. Here, I am reporting all the results after incoherent Franck-Condon averaging to resemble H_2^+ the vibrational state distribution in an ion-beam experiment [15].

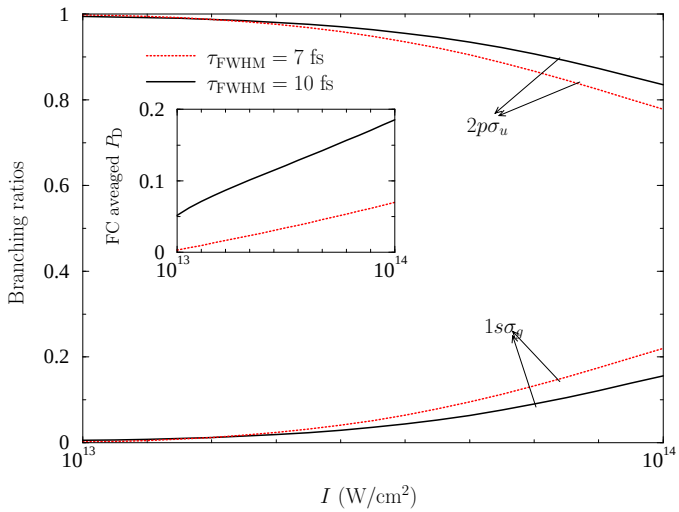

Figure 7.1 Branching ratios of FC-averaged $1s\sigma_g$ and $2p\sigma_u$ as a function of laser peak intensity for two different pulse length; Inset shows FC-averaged total dissociation probability for these pulses.

7.2.1 Branching ratios

Figure 7.1 shows the branching ratios of dissociation probabilities in the $1s\sigma_g$ and $2p\sigma_u$ channels. The branching ratio is calculated by taking the ratio between the FC-averaged dissociation probabilities in each $1s\sigma_g$ and $2p\sigma_u$ channel and the total FC-averaged dissociation probability P_{D}. Figure 7.1 shows that $2p\sigma_u$ dominates the dissociation for all intensities, but for $I > 8 \times 10^{13}$ W/cm^2 $1s\sigma_g$ starts contributing with more than ten percent probability. The difference between the two channels becomes smaller by about ten percent for a short pulse of 7 fs, indicating that a shorter pulse would give a large asymmetry. This finding agrees with an earlier prediction that carrier-envelope phase effects decrease exponentially with pulse duration [44]. Taking it as a first good indication, we will use a 7 fs pulse to study up-down asymmetry in the momentum distribution. The difference between the branching ratios of $1s\sigma_g$ and $2p\sigma_u$ also decreases with intensity and thus increases the up-down asymmetry. The inset in Fig. 7.1 shows that the dissociation probability for 7 fs is smaller than that of 10 fs for the enitre intensity range, indicating that the shorter pulse will give a larger asymmetry in a smaller signal. Using a higher intensity would be

better to improve the signal and to make the channel dissociations comparable in an experiment. Threrefore, branching ratios provide the necessary information about the required laser parameters. Comparable branching ratios of $1s\sigma_g$ and $2p\sigma_u$ are only a necessary but not sufficient condition for their interference. Both of the channels should contribute to the same energy.

7.2.2 Momentum distribution and up-down asymmetry

From the discussion in Secs. 6.3–6.5 regarding different photon processes, we found that the 2ω peaks overlap in energy with net-1ω peaks for lower vibrational states. Vibrational states dissociating mainly by 1ω will have small overlap tails with 0ω and 2ω dissociation. To elaborate, KER-distributions for several individual vibrational states are plotted in Fig. 7.2(a)-(h). Vibrational states $v = 3$, 4 have comparable contributions from two channels, $v = 5$, 6, and 7 have small overlaps in energy from two channels, and for others, the contribution from $1s\sigma_g$ is negligible compared to $2p\sigma_u$. Thus, we expect lower vibrational states to show large up-down asymmetry. Carrier-envelope phase effects are found to be dominant for lower vibrational states in HD^+ dissociation [148]. The KER-distributions from $1s\sigma_g$ and $2p\sigma_u$ overlap in the energy range of 0.5 to 1.5 eV (corresponding to the momentum of 6 to 10 a.u.). The overlap occurs between 2ω in $1s\sigma_g$ and net-1ω in $2p\sigma_u$ for $v = 3$ and 4 (see Fig. 7.2), while for $v \geq 5$, 1ω and 2ω dissociation overlap in energy.

From the above discussion, we conclude that the momentum distribution will have an up-down asymmetry in the range of 6 to 10 a.u. of momentum, and a weaker contribution from lower vibrational states ($v = 3$ to 6 or 7) determines the strength of the asymmetry in the Franck-Condon averaged momentum distribution. Let us look at the momentum distribution. Franck-Condon averaged momentum distributions for several CEP are shown in Figs. 7.3(a)-(h) for a 7 fs pulse. The momentum distributions are aligned along the laser polarization (along $P_\parallel$). Closely examining the distributions, we find that an aligned peak at about $(P_\parallel, P_\perp) = (7, 0)$ a.u. in Fig. 7.3(a) becomes broader and slightly lower in momentum

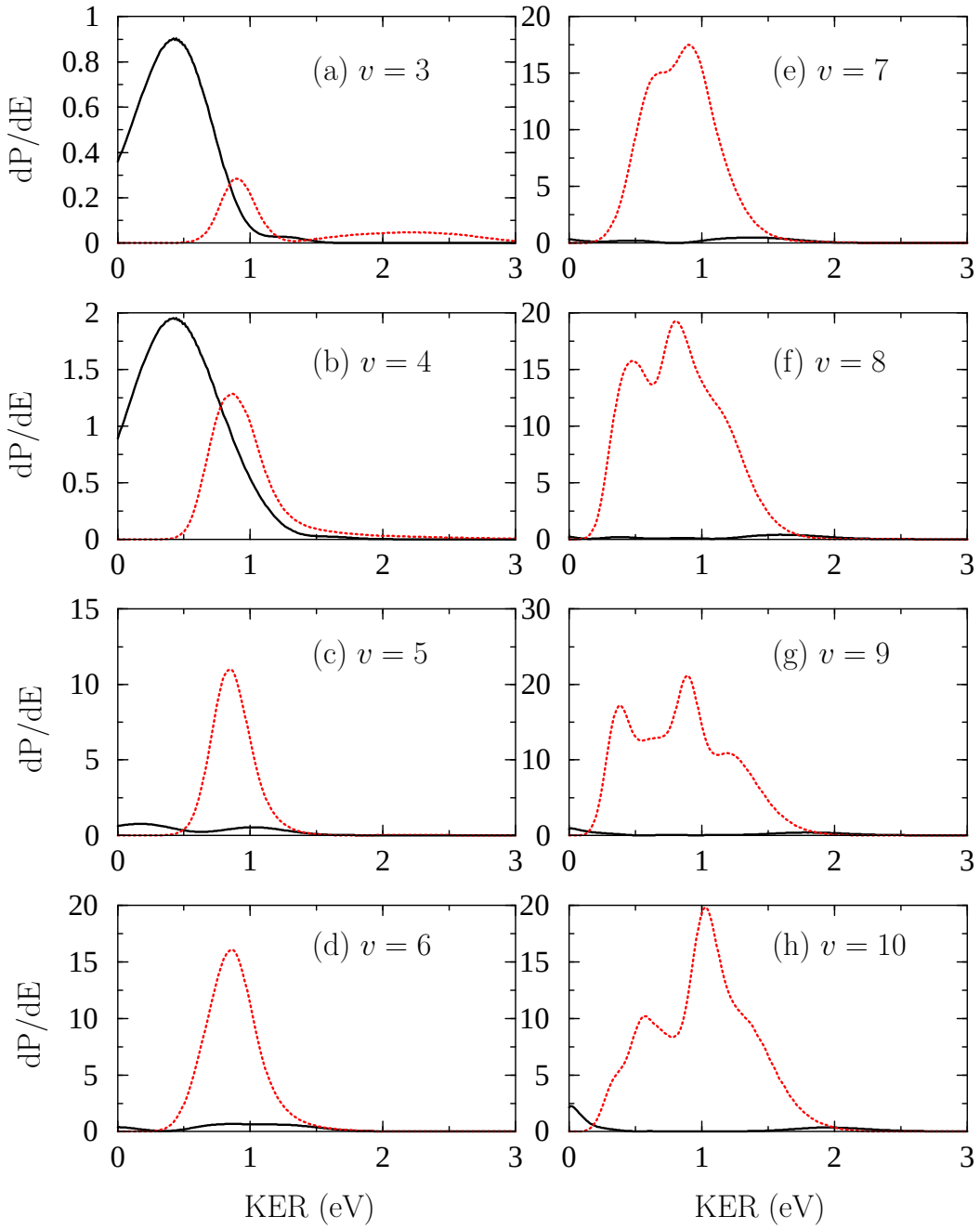

Figure 7.2 (a)-(h) show the KER-distribution from $1s\sigma_g$ (black solid line) and $2p\sigma_u$ (red dotted line) channels for individual initial vibrational states from 3 to 10, respectively. $\tau_{\mathrm{FWHM}} = 7$ fs and $I = 10^{14}$ W/cm^2.

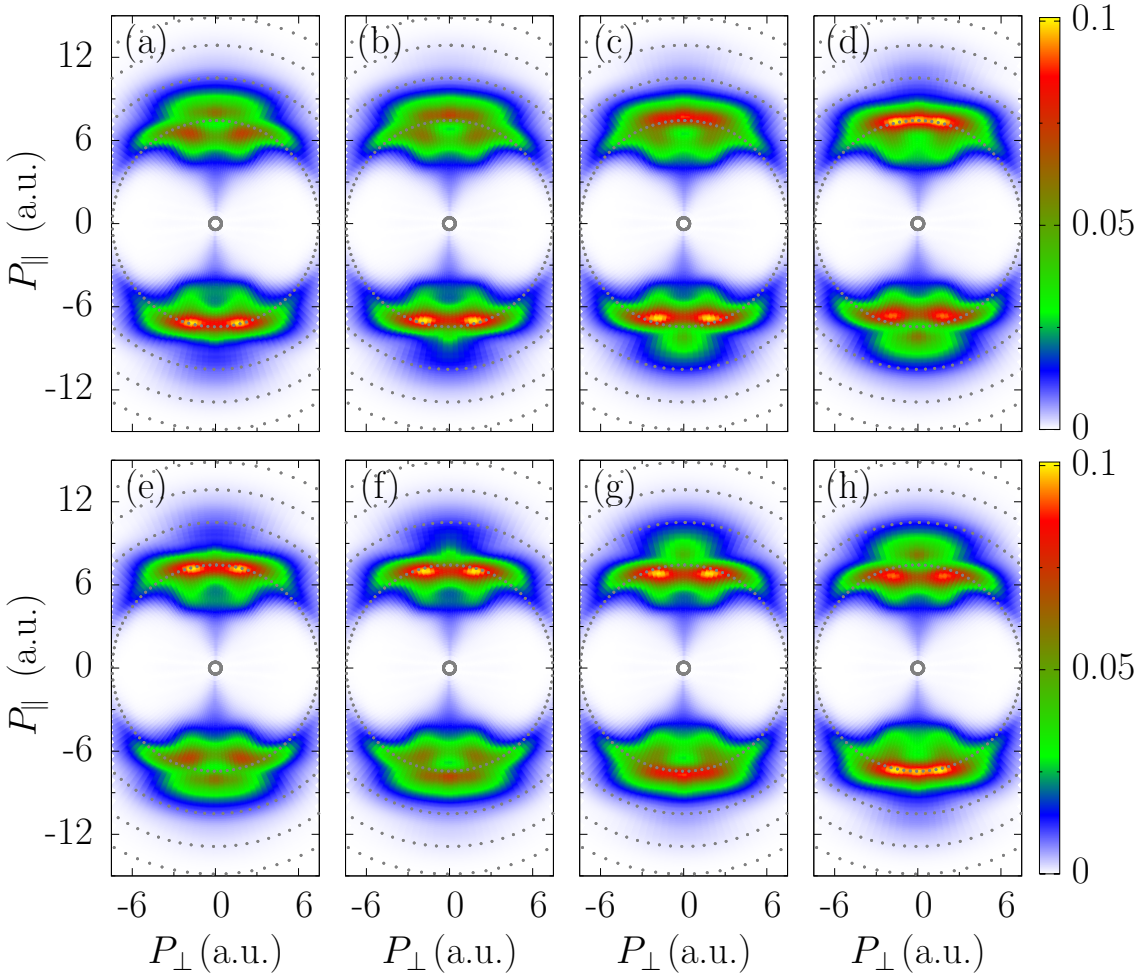

Figure 7.3 (a)-(g) show FC-averaged momentum distributions for $\varphi = 0$ to 1.75π with an increment of 0.25π between successive plots. Gray dotted circles are constant momentum lines. $\tau_{\mathrm{FWHM}} = 7$ fs and $I = 10^{14}$ W/cm^2.

[see Fig. 7.3(b)] and then appears opposite to $P_{\parallel}$ for $\varphi = \pi/2$ with $(P_{\perp}, P_{\parallel}) = (-7, 0)$ a.u., and then again becomes broader and apears along $P_{\parallel}$. The momentum distribution for $\varphi = \pi$ in Fig. 7.3(e) is the mirror image of Fig. 7.3(a), which is guaranteed from the symmetry of the Schrödinger equation. Besides the aligned peak at $(P_{\parallel}, P_{\perp}) = (7, 0)$ a.u. in Fig. 7.3(a), other structure like the double peak structure at about 25 and 155 degrees (from $P_{\parallel}$ close to the $P = 7$ a.u.) remains unaffected by CEP. To quantify CEP-dependence, we define an asymmetry parameter $A(E)$ similar to previous studies [45, 136, 140] as

$$A(E, \varphi) = \frac{\int_0^{\pi/2} \rho(E, \theta) \sin\theta d\theta - \int_{\pi/2}^{\pi} \rho(E, \theta) \sin\theta d\theta}{dP/dE}. \tag{7.3}$$

We integrate over the whole upper and lower halves of the distribution unlike some experimental studies [45, 140], where a narrow cut in angle along the laser polarization direction is used to calculate A. An angular cut would enhance $A(E, \varphi)$, since the peak of the momentum distribution changing significantly with CEP lies in the angular range of $0 \rightarrow 3\pi/8$ and $5\pi/8 \rightarrow \pi$ in the upper and lower half of the distribution, respectively. Moreover, we found no CEP dependence in the total KER distribution (which is the denominator in Eq. (7.3)) within the accuracy of our calculations. It is an interesting result and contradicts the aligned model results, where both the total KER distribution and up-down asymmetry show CEP dependence [136].

Figure 7.4 shows $A(E, \varphi)$ as a function of KER and carrier-envelope phase. We can see reasonable asymmetry in the range 0.2–2.5 eV. It oscillates between -0.12 and 0.12 and the maximum amplitude appears at 2.2 eV, which does not lie in our estimated range of 0.5 to 1.5 eV. The reason for large asymmetry at 2.2 eV is not the bigger contrast between the up and down probability but the small dP/dE in the denominator (see Fig. 7.2). We find that A qualitatively resembles the aligned model results in Ref. [136]. It is not clear why the results agree for asymmetry but not for the CEP effects in the total KER distribution from the two calculations. In Ch. 4, we found that only after the angle-averaging defined in Eq. (4.2) did the total dissociation probability from the aligned model agree with that obtained from our method including nuclear rotation. Thus to have a more reliable answer about the

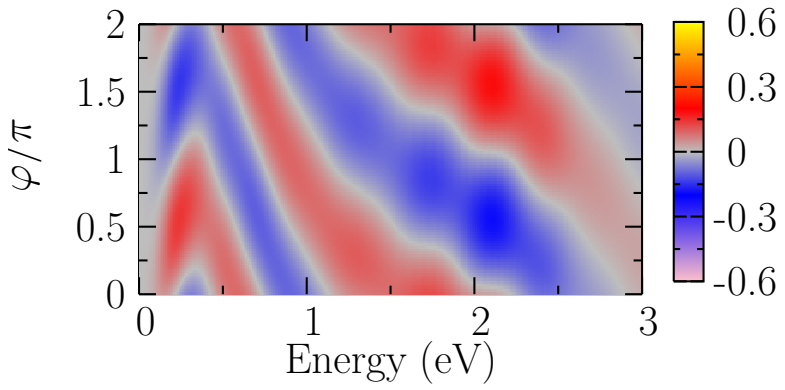

Figure 7.4 Asymmetry defined in Eq. (7.3) plotted with KER and CEP (φ); laser parameters are same as in Fig. 7.3.

asymmetry from the aligned model, one might perform angle averaging as described in Chap. 4. We think it is something that should be further investigated. We also looked at the angular distribution of the fragments after integrating over the entire energy range. The angular distribution shows negligible CEP effects. That is not surprising given that up-down asymmetries are different in different energy ranges and get averaged out after integration.

7.2.3 Intensity averaging

The most crucial test for an intensity-dependent effect to be observable in an experiment is whether it survives intensity or focal volume averaging (see Sec. 6.6.1 for details). We performed intensity averaging for a fixed carrier-envelope phase of $\varphi = 0$ for a 7 fs laser pulse up to the peak intensity of 1.2×10^{14} W/cm^2. From Fig. 7.3(a) and Fig. 7.4, we see clear up-down asymmetry for zero carrier-envelope phase. So, if the asymmetry does not survive for $\varphi = 0$, it is hard to imagine that it would survive for any other CEP. Figure 7.5(b) shows asymmetry before and after the intensity averaging. The total KER distribution for the two cases is also plotted in Fig. 7.5(a) to indicate that the small dP/dE is the reason for the large up-down asymmetry for some energies. Intensity averaging indeed reduces up-down asymmetry by more than a factor of three over the entire energy range shown in Fig. 7.5 and makes it 17 times smaller for 0.5 to 1.0 eV, where dP/dE is large and the single intensity

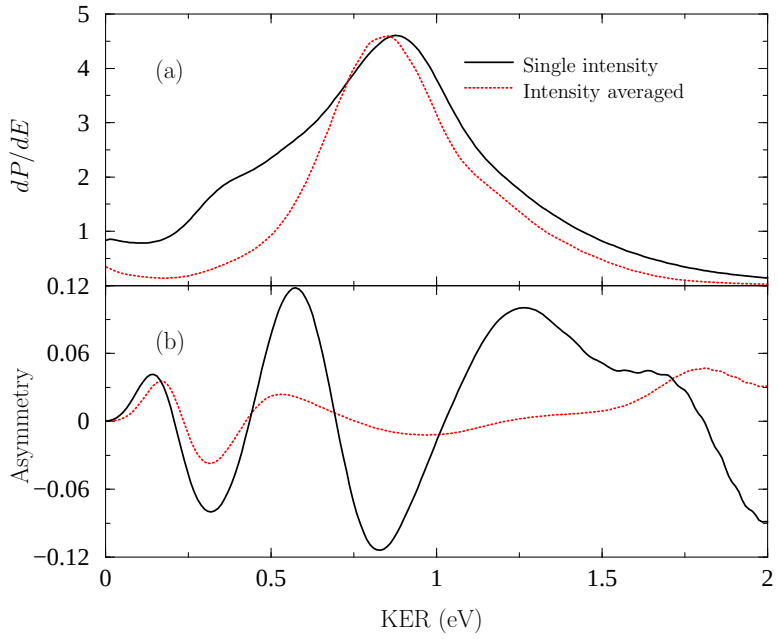

Figure 7.5 (a) total KER distribution for the peak intensity of 1.2×10^{14} W/cm^2 before (black solid line) and after (red dotted lines) the intensity averaging. Peaks for the two cases are normalized to the same value. (b) Asymmetry before (black solid line) and after (red dotted lines) the intensity averaging. $\tau_{\mathrm{FWHM}} = 7$ fs.

shows maximum amplitude for A. In a previous study, intensity averaging also reduced the CEP effects in HD^+ channel asymmetry [44].

The reason for the significant reduction in A lies in the fact that 1ω dissociation for $v \geq 7$ overlaps in energy with the KER-distribution from lower vibrational states and does not show any up-down asymmetry (as it has primarily a $2p\sigma_u$ contribution). I should emphasize that different vibrational states will not interfere with each other to give any asymmetry as their contributions are added incoherently. Also, very weak intensities can dissociate H_2^+ by 1ω. Therefore, in an intensity averaged momentum distribution, 1ω gives a large symmetric contribution compared to the small asymmetric contribution from the 2ω and net-1ω dissociation interference and reduces up-down asymmetry. The intensity-differencing scheme proposed in Ref. [149] can make the asymmetry stronger.

I will conclude this section by pointing out that we have presented the first theoretical study of carrier-envelope phase effects in the momentum distribution including nuclear ro-

tation. Nuclear rotation does not completely wash out CEP-effects in H_2^+ dissociation by a single few-cycle laser pulse. Up-down asymmetry appears in the momentum distribution mainly by the interference of 2ω above-threshold dissociation and below-threshold dissociation in $1s\sigma_g$ and $2p\sigma_u$ channels, respectively, for $v < 5$. Interference between 1ω and 2ω gives asymmetry from the fifth to the seventh vibrational states. High-lying vibrational states $v \geq 8$ dissociate mostly by one photon or bond-softening giving a symmetric momentum distribution. It is this one photon symmetric distribution that reduces up-down asymmetry after the intensity averaging. Thus, large one photon dissociation from high lying vibrational states makes measuring CEP-effects in H_2^+ dissociation by a single few-cycle pulse a challenging experiment. From our results, we can also interpret the reason for the successful CEP measuremnts in a gas-jet experiment. Field ionization of H_2 has a narrow distribution in lower vibrational states [150], thus their subsequent dissociation gives significant CEP effects as up-down asymmetry in momentum distribution.

7.3 A pump-probe study: Enhanced CEP effects from a prepared initial state of H_2^+

From our discussion in the previous section, we have identified one photon dissociation as the main reason for the reduced up-down asymmetry in the momentum distribution. Here, we will propose a pump-probe scheme to reduce the effect of 1ω dissociation by depleting high lying states with the pump and thereby enhancing the up-down asymmetry by up to an order of magnitude in the intensity averaged momentum distribution. Pump-probe techniques have existed for a long time and have developed greatly in recent years for experiments involving short laser pulses. In the intense laser community, the pump is generally used to excite a coherent state and the probe to monitor its dynamics [68, 151].

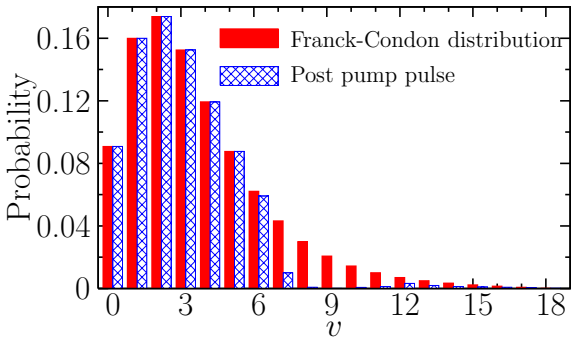

Figure 7.6 Initial vibrational states distribution before and after the pump pulse with $\tau_{\text{FWHM}} = 45$ fs, $I = 10^{13}$ W/cm^2.

7.3.1 Preparing the initial state with the pump pulse

In our study, we will use a long weak pulse of 45 fs with a peak intensity of 10^{13} W/cm^2 as the pump pulse. The long and weak pump pulses ensure the depletion of higher vibrational states by 1ω and effect the population of lower states that can give up-down asymmetry. We don't want to use a short intense pulse for the pump as it will not serve the purpose of depleting higher vibrational states and can dissociate them all. In the later step, we will dissociate the remaining bound part of the wave function by a few cycle probe pulse. For the probe pulse, we used the same laser parameters as in Sec. 7.2. So, we will refer to the results described in the previous section as a "probe-only" as opposed to a "pump-probe" study for the results in this section. Moreover, the pump-probe results will contain only the probe part assuming there is no pump signal. The combined pump and probe signal will be discussed at the end of the section. Our 45 fs pump pulse efficiently depletes all the vibrational states lying in the bond-softening region (lying close to the one photon crossing in the Floquet-picture). Figure 7.6 shows the v-distribution before and after the pump pulse. Initial distributions have been taken to be Franck-Condon (FC). In this case, 9.58 % of the population lies in $v \geq 8$, and the pump pulse dissociates 90 percent of this population. Therefore, $v \geq 8$ becomes only 1.36 % of the total bound population after the pump pulse. While dissociating most of the high lying vibrational states, the 45 fs pulse makes the

bound and dissociating wave function rotationally excited by populating J up to 38 in the remaining bound population of $v \geq 8$. This complicates the probe-pulse calculations as the high intensity probe causes further excitations, making the calculations very tedious. To avoid these tedious calculations, we chose to perform probe-pulse calculations only for $v = 0 - 7$, as these states account for most of the bound population. In a single case study including all vibrational states, we found that the results remain unaffected by the absence of the high-lying vibrational states.

After the pump pulse, we can propagate the remaining bound wave function numerically using a Crank-Nicholson propagator as was done for field-assisted propagation. This approach can be very time consuming for propagatation to long time-delays. Another approach is to extract the amplitudes for each ro-vibrational bound states and then calculate the bound wave function at any time delay analytically. We used the approach in our calculations. So, the bound nuclear wave function $\psi_{\mathrm{B}v}(\mathbf{R}, t > t_f)$ in the $1s\sigma_g$ channel for each vibrational state at time $t > t_f$ after the pump pulse (t_f is the final time for the pump) as defined in Eq. (2.29) will be

$$\Psi_{Bv}(\mathbf{R}, t) = \sum_J \Omega^J_{0M}(\hat{R}) \sum_{v'} a_{v'J}(t_f) e^{iE_{v'J}(t-t_f)} \chi_{v'J}(R). \tag{7.4}$$

Using this as an initial state, we propagated the above wave function in the probe pulse for the time delay of 267 fs between the peak of the pump and probe and analyzed the final wave function to calculate the momentum distribution and up-down asymmetry.

7.3.2 Carrier-envelope phase effects after the probe pulse

To compare with the probe-only results, we performed the calculations as a function of the carrier-envelope phase of the probe pulse with a peak intensity of 10^{14} W/cm^2 and a 7 fs duration. For most of the results, the time delay between the peaks of the pump and probe pulses is 267 fs (marked (A) in Fig. 7.11) unless otherwise specified.

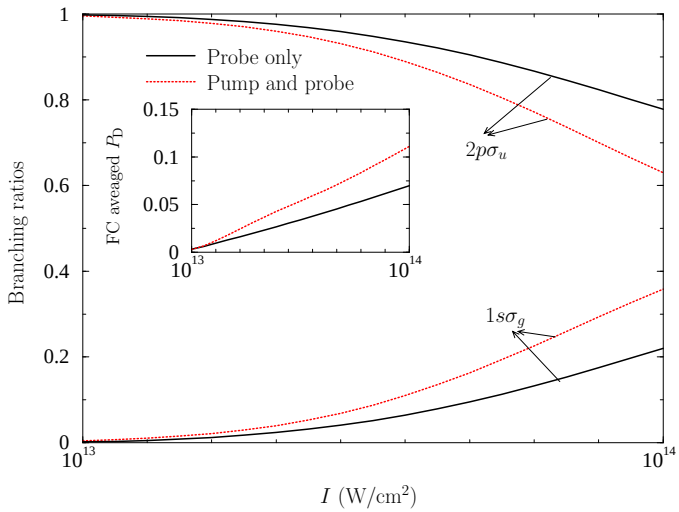

Figure 7.7 Branching ratios of FC-averaged $1\sigma_g$ and $2p\sigma_u$ dissociation probabilities with laser peak intensity for probe-only (black solid line) and pump-probe (red dotted line) studies. Inset shows FC-averaged total dissociation probability for the two cases.

7.3.2.1 Comparison of the branching ratios

Similar to Fig. 7.1, we compare the probe-only and pump-probe branching ratios of the $1s\sigma_g$ and $2p\sigma_u$ channels. Figure 7.7 shows that for lower intensity, dissociation is dominated by $2p\sigma_u$, and therefore no up-down asymmetry is expected for the lower intensities in both cases. The difference between the branching ratios of the two channels reduces faster with intensity in the pump-probe study compared to the probe-only case. It indicates that the momentum distribution in pump-probe dissociation should show a larger up-down asymmetry than the single pulse dissociation. The inset in Fig. 7.7 shows that the FC-averaged dissociation probability becomes larger for the 7 fs pulse in the pump-probe study. The dissociation probability for the pump-probe case has not been normalized by the initial bound population after the pump pulse and thus represents an absolute number and indicates that the rotational pumping of the lower vibrational states enhances the dissociation probability. This makes our scheme more attractive to study CEP effects as it will be from a large signal.

7.3.2.2 Momentum distribution and the up-down asymmetry

Momentum distributions for various carrier-envelope phases are shown in Figs. 7.8(a–h). Comparing Fig. 7.8 with Fig. 7.3, we find that the momentum distributions are more aligned for the pump-probe study. In this case, the momentum distribution significantly varies with the carrier-envelope phase. We see an interesting double-peak structure along $P_{\parallel}$ in the upper half of the plane and a single peak in the lower half of Fig. 7.8(a). Peaks start merging for $\varphi = \pi/4$ and a small peak starts building up near $(P_{\parallel}, P_{\perp}) = (-7.5, 0)$ a.u. in Fig. 7.8(b). Later, for $\varphi = \pi/2$ and $\varphi = \pi$, the double-peak structure becomes clearer in the lower half of the momentum distributions in Fig. 7.8(c) and Fig. 7.8(d) to give a mirror image of Fig. 7.8(a) in Fig. 7.8(e). Further changing φ shifts the double-peak back to the upper half of the momentum distribution. A signature of the up-down asymmetry can be seen by following the inner most gray dotted line in Fig. 7.8(a) as it passes through a peak in lower half and a minimum in the upper half of the momentum distribution.

Nevertheless, to make a quantitative comparison between the pump-only and the pump-probe results, we calculated $A(E, \varphi)$ using Eq. (7.3). Comparing Fig. 7.9(a) and Fig. 7.9(b), we find that depleting higher vibrational states leads to a five-fold enhancement in up-down asymmetry with carrier-envelope phase for a single intensity. We also see from Fig. 7.9(b) that the asymmetry is large in the energy range of 0.8–1.5 eV, which corresponds to the large KER distribution. Both cases show stripes in the density plot of $A(E, \varphi)$ with KER and φ. The slope for these stripes is large for the pump-probe case. While the stripes have also been seen in previous CEP studies, their origin is unknown. It would be interesting to investigate why the asymmetry shows these well-defined stripes.

7.3.2.3 Intensity averaging

Similar to the probe-only case, we also performed intensity averaging for the pump-probe results at a fixed CEP of $\varphi = 0$. Since we saw significant enhancement in A in our pump-probe scheme for a 7 fs pulse, we also performed the study for a longer 10 fs pulse to

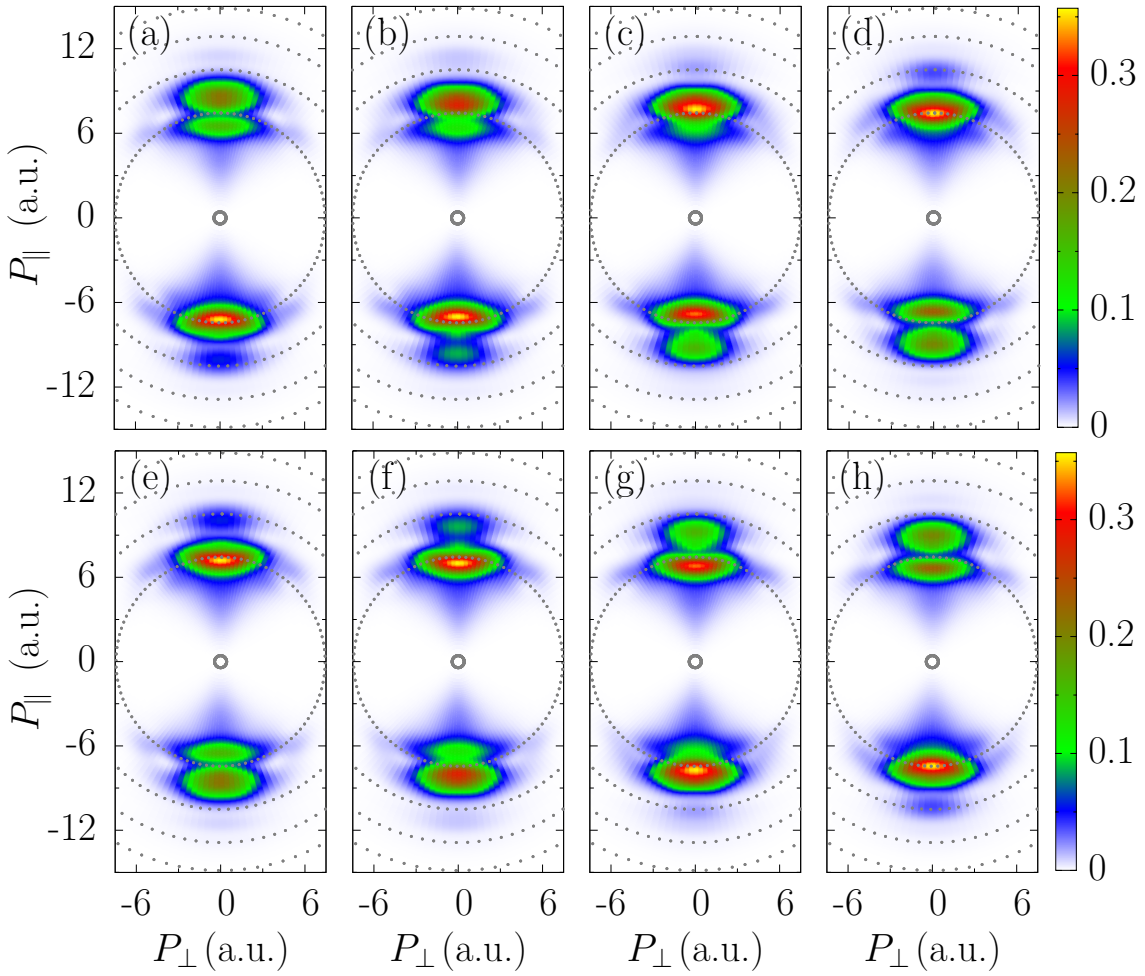

Figure 7.8 (a)-(h) shows FC-averaged momentum distributions for $\varphi = 0$ to 1.75π with an increment of 0.25π between successive plots. Gray dotted lines are constant momentum lines. Probe pulse $\tau_{\mathrm{FWHM}} = 7$ fs and $I = 10^{14}$ W/cm^2.

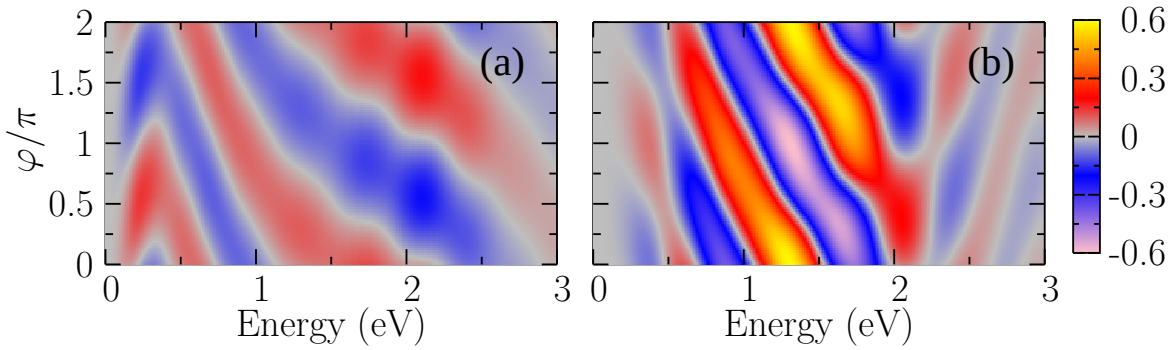

Figure 7.9 (a) Figure 7.4 replotted to compare with the pump-probe asymmetry in (b). $\tau_{\mathrm{FWHM}} = 7$ fs and $I = 10^{14}$ W/cm^2.

check if the asymmetry becomes large. The resulting asymmetry for the two pulse lengths, namely 7 and 10 fs at peak intensities of 1.2×10^{14} and 10^{14} W/cm^2 is shown in Fig. 7.10(a) and Fig. 7.10(b), respectively. These show clearly an order of magnitude enhancement in asymmetry for both the 7 and 10 fs pulses in pump-probe results compared to the pump-only results. These pulses are longer than the 6 fs pulses usualy used to observe CEP effects. So, we report a remarkable CEP effect in the up-down asymmetry in H_2^+ dissociation by a 10 fs pulse. Figure 7.10(b) shows that intensity averaging makes it impossible to measure the CEP-effects from a single 10 fs pulse in an experiment.

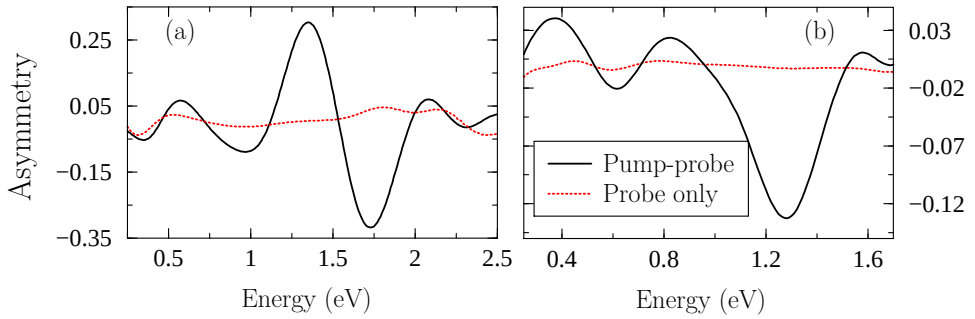

Figure 7.10 (a) Asymmetry from the intensity-averaged momentum distribution for pump-only (red) and pump-probe (blue) study for a 7 fs pulse with a peak intensity of 1.2×10^{14} W/cm^2. (b) Same as (a) for 10 fs with peak intensity of 10^{14} W/cm^2.

7.3.2.4 Asymmetry for different pump-probe time delays

In addition to the depletion of the high-lying vibrational states, the pump also non-adiabatically aligns the molecule as shown in Fig. 7.11, which shows $\langle \cos^2\theta \rangle$ for the bound wave function. Rotational revivals of H_2^+ were already discussed in detail in Chap. 5. So far, all the pump-probe results are for a fixed time delay of 267 fs, which is marked as (A) in Fig. 7.11. We see from Fig. 7.11 that the angular distribution of H_2^+ at (A) is sharply aligned along the laser polarization, which means that the alignment can also be the reason for the enhanced asymmetry. To investigate the sensitivity of A on the initial angular distribution, we compare the asymmetry from three different time delays of 267, 2455, and 3749 fs marked as (A), (B), and (C) respectively in Fig. 7.11. The initial angular distributions for the three time delays are clearly different from each other. The kinetic energy release distribution and $A(E)$ for the three (A), (B), and (C) cases are shown in Figs. 7.12(a) and 7.12(b), respectively. It is evident from Fig. 7.12(a) that the total dissociation probability decreases significantly as the initial angular distribution changes from aligned to anti-aligned ((A) to (C)), while $A(E)$ remains comparable for these cases. For the entire energy range in Fig. 7.12, the difference between maximum up and maximum down asymmetry is 1.04, 0.675, and 1.04 for (A), (B), and (C), respectively. For the 0–1.5 (eV) range with large dP/DE, this difference for (A),

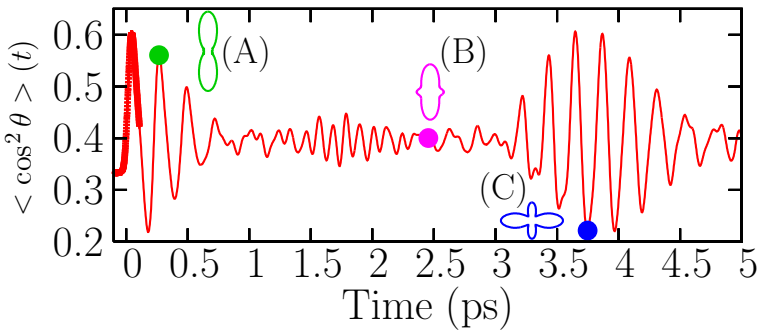

Figure 7.11 Franck-Condon averaged $\cos^2\theta$ for the bound population of H_2^+ during (red symbol) and after the pump (solid line);(A), (B), and (C) labels angular distribution of FC-averaged bound population at the delay of 267 (green), 2455 (magenta), and 3749 fs (blue) from the peak of the pump; $\tau_{\mathrm{FWHM}} = 45$ fs, $I = 10^{13}$ W/cm^2.

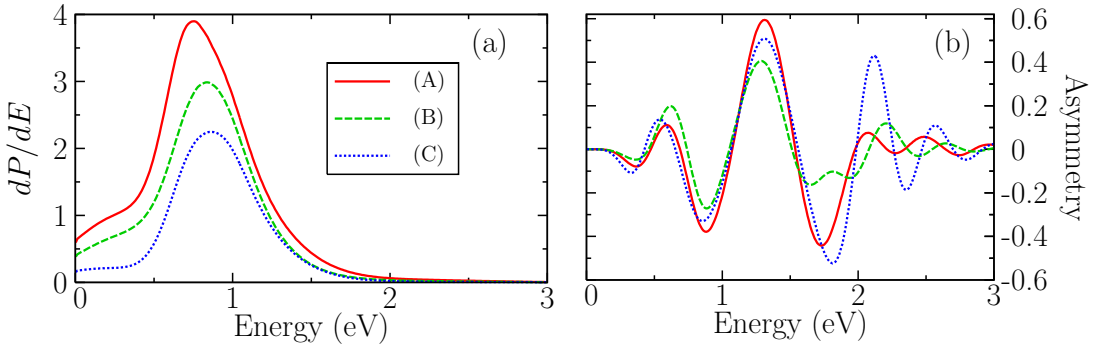

Figure 7.12 (a) KER-distribution (dP/dE) for the pump-probe time delay of 267, 2455, and 3749 fs marked as (A) (red solid line), (B) (green dashed line), and (C) (blue dotted line) respectively. (b) Up-down asymmetry defined in Eq. (7.3) for (A), (B), and (C). $\tau_{\mathrm{FWHM}} = 7$ fs and peak intensity of 10^{14} W/cm^2.

(B), and (C) is 0.98, 0.675, and 0.84, respectively. This indicates that while the asymmetry for (A) and (C) is equivalent, a significant dissociation signal in an experiment will lie in the 0–1.5 (eV) range in these cases, where (A) has a larger amplitude in $A(E)$ than (C). We can draw two conclusions from this comparison. Firstly, the depletion of high-lying vibrational states is the major reason for enhanced up-down asymmetry, and secondly, asymmetry can be further enhanced up to 30% by initially aligning the molecule.

7.3.2.5 Separating pump and probe signals in an experiment

Here we will discuss an important issue of separating the pump and probe signals in our scheme as dissociating fragments from both pulses would fly to the same detector in an experiment. In the following discussion we will show that the separation can be done in a number of ways. The reason for the reduced asymmetry in the probe-only study was the overlap of the KER-distribution from bond-softening, ATD, and below-threshold dissociation to the same low energy range of 0.5-1.5 eV. The same is true in the pump-probe study. We still expect the asymmetry to be large in a combined pump-probe signal because the relative dissociation probability for lower vibrational states becomes much larger after the rotational pumping, giving a better contrast. And, the long pump pulse also produces KER-distribution with well defined peaks from different vibrational states because

of the small bandwidth of laser. Therefore, the pump-probe momentum distribution and the asymmetry would have symmetric structure on the top of asymmetric signal (not just the overall symmetric signal as in probe-only case). To demonstrate, we have calculated

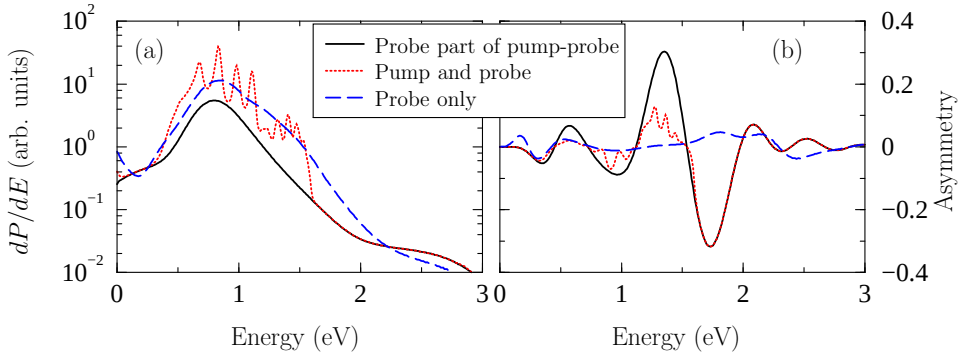

Figure 7.13 (a) Intensity-averaged total KER-distribution. (b) Intensity-averaged up-down asymmetry for the three cases in (a). $\tau_{\mathrm{FWHM}} = 7$ fs and peak intensity for pump up to 10^{13} W/cm^2 and for probe up to 1.2×10^{14} W/cm^2.

the asymmetry for the combined pump-probe intensity-averaged momentum distribution. Figure 7.13 shows the results for the combined pump-probe results along with just the probe part of the pump-probe and probe-only KER-distribution and asymmetry. We see from Fig. 7.13 that $A(E)$ remains unaffected for $E \geq 1.5$ eV, since the pump pulse dissociation does not contribute to this energy range. Although in the 0.5–1.5 eV energy range, the $A(E)$ amplitude becomes small, it is still larger than in the probe-only case on average by a factor of five. This check ensures the feasibility of measuring the effect in an experiment.

The contrast can be further enhanced using pulses longer than 45 fs, thereby increasing the depletion of the higher vibrational states. Also, the pump signal will be more structured and therefore have a small overlap over the whole energy range. A longer pulse will give more alignment, which can also enhance asymmetry. An angular cut can be helpful as $A(E)$ becomes the more aligned part of the angular distribution. It would be better to use different laser focusing for the pump and probe pulses, i.e. relatively flat spatial focusing for pump compared to the probe pulse. It will ensure the depletion of higher vibrational states in all the molecules interacting with the probe pulse, thus giving a large signal from the

subsequent dissociation. As the dissociation primarily occurs along the laser polarization, a better way might be to use different laser polarization directions for pump and probe pulses to separate their signals. For this one might want to use the time-delay when the molecules are antialigned to improve the signal. Since depletion is the major reason for enhanced CEP effects, we believe the effect should survive by using different laser polarizations. Similar to the probe-only case, an intensity differencing scheme might also be useful to enhance asymmetry. One might also be able to separate the pump-probe signals by repeating the experiment with and without the probe pulse and then subtracting the two to get the probe part of the signal. Differencing schemes mostly require a dense target density and hence for an H_2^+ ion beam will not be very effective.

7.4 Summary

To summarize, we presented a benchmark study for the momentum distribution of H_2^+ dissociation by few-cycle laser pulses. We see an up-down asymmetry in the incoherently FC-averaged momentum distribution of H_2^+ dissociation fragments by short pulses of 7 and 10 fs and an intensity of 10^{14} W/cm^2. Asymmetry changes as a function of carrier envelope phase of the short pulse. While significant for a single intensity, asymmetry becomes negligible after intensity averaging due to the large contribution from the higher vibrational states with symmetric momentum distributions. Thus, we propose a pump-probe scheme to deplete higher vibrational states by a long, weak pump pulse and see an order of magnitude enhancement in intensity averaged up-down asymmetry. Besides depletion, an initially aligned molecule can further enhance the asymmetry. We are optimistic that by using different techniques pump and probe signals can be efficiently separated. Moreover, we are optimistic that the effect should be observable in neutral hydrogen, its isotopes and also other molecules.

Chapter 8

Conclusion

This dissertation presents a systematic theoretical study of H_2^+ dissociation in intense short laser pulses. Our study proved to be very useful in giving a basic understanding about the behavior of H_2^+ dissociation.

By developing a theoretical formulation that is essentially exact for H_2^+ dissociation, we were able to solve the TDSE for H_2^+ in Gaussian laser pulses for a range of intensities and pulse durations. The dissertation thus provides a benchmark study of H_2^+ dissociation by few-cycle laser pulses, because most previous calculations were done for aligned molecules. This dissertation is comprehensive, discussing the total dissociation probability of H_2^+, the dynamics of dissociating and bound wave functions, and the angular, kinetic energy, and momentum distributions of p+H.

In the beginning, we had little knowledge about the role of nuclear rotation in H_2^+ dissociation by short (10 fs) laser pulses. Given that the H_2^+ rotational period is much longer than the laser duration in most of the recent studies, it was not obvious that nuclear rotation would have any impact on the molecular dynamics. By comparing full-dimensional total dissociation probabilities to that of the aligned model and also by studying the dynamics of the dissociating fragments, we found that even for pulses shorter than 10 fs, the aligned model results only agree qualitatively with the exact results.

We developed an intuitive way to quantify dynamical alignment by comparing the angle-averaged (effectively intensity-averaged) aligned model dissociation probabilities to those

of our full-dimensional method. This comparison showed that angle-averaged dissociation probabilities compare better with the full-dimension dissociation probabilities. So, if unavoidable, calculations can be performed without including the nuclear rotation, but angle-averaging should be performed.

The laser electric field initiates a coherent rotational wavepacket for individual vibrational states which evolves and revives after the laser field. Incoherent FC-averaging pushes the revival time to long intervals of about 4 ps. The revival time depends on the slowest frequency in the wave function. The slowest frequency for an initial $J = 0$ is different, for example, from the slowest frequency for initial $J = 1$ and for initial $J = 2$, $M = 1, 2$. Therefore, thermal averaging would be necessary to get information about physically observable rotational revivals as the revival times depend strongly on the initial angular momentum state.

Our work was a big step forward for quantitative comparison with experimental observables like kinetic-energy release angular, and momentum distributions. Further investigation should be done to include thermal-averaging. Nevertheless, intensity averaging greatly improves the agreement between theory and experiment.

The carrier-envelope phase of few cycle pulses affects the direction of the emission of the proton and hydrogen. This appears as an up-down asymmetry in the momentum distribution along the laser polarization direction. Up-down asymmetry is large for the lower vibrational states of H_2^+ as different photon processes are comparable and contribute to the same energy. The high-lying vibrational states exhibit symmetric momentum distributions and dissociate very easily primarily by 1ω dissociation. Thus, they give a large contribution to the dissociation in an experiment because of the intensity averaging, and makes the asymmetry negligible. To get around this problem, we proposed a pump-probe study, where a long pulse depletes all the higher vibrational states and aligns the remaining bound population. A CEP-locked probe will then give an enhanced up-down asymmetry. We believe the asymmetry can be observed in an experiment.

Finally, our study has not yet taken into account thermal averaging. This will be an important next step to make the study complete and to make quantitative comparison with experimental findings. Our group will take the theoretical formulation I developed and continue to explore the behavior of H_2^+ and D_2^+ in a laser field. Further, the generalized structure of the theoretical formulation will help extend the formulation for the interaction of H_2^+ with elliptically polarized light and also to more generalized problems including multielectron diatomic molecules and heteronuclear molecules. In one such effort, we have already performed the numerical calculations for the dissociation of metastable ground state CO^{2+} by a laser field [14].

My Publications

[1] F. Anis, V. Roudnev, R. Cabrera-Trujillo, and B. D. Esry, "*Laser-assisted charge transfer in He^{2+} + H collisions*," Phys. Rev. A **73**, 043414 (2006).

[2] I. Ben-Itzhak, A. M. Sayler, P. Q. Wang, J. McKenna, B. Gaire, N. G. Johnson, M. Leonard, E. Parke, K. D. Carnes, F. Anis, and B. D. Esry, "*Ionization and dissociation of molecular ion beams caused by ultrashort intense laser pulses*," Journal of Physics: Conference Series **88**, 012046 (2007).

[3] F. Anis and B. D. Esry, "*Role of nuclear rotation in dissociation of H_2^+ in a short laser pulse*," Phys. Rev. A (Atomic, Molecular, and Optical Physics) **77**, 033416 (2008).

[4] J. McKenna, A. M. Sayler, F. Anis, B. Gaire, N. G. Johnson, E. Parke, J. J. Hua, H. Mashiko, C. M. Nakamura, E. Moon, Z. Chang, K. D. Carnes, B. D. Esry, and I. Ben-Itzhak, "*Enhancing High-Order Above-Threshold Dissociation of H_2^+ Beams with Few-Cycle Laser Pulses*," Phys. Rev. Lett. **100**, 133001 (2008).

[5] F. Anis, T. Cackowski, and B. D. Esry, "*Rotational dynamics of dissociating H+2 in a short intense laser pulse*," J. Phys. B **42**, 091001 (2009).

[6] F. Anis and B. D. Esry, "*3D Calculations using a new method for Hydrogen atom in intense laser field*," J. Phys. B: Atomic, Molecular and Optical Physics (2009), (to be submitted).

[7] F. Anis and B. D. Esry, "*Controlling asymmetry in momentum distribution of H_2^+ dissociation*," Phys. Rev. Lett. (2009), (to be submitted).

[8] F. Anis and B. D. Esry, "*Enhancement of carrier-envelope phase effects in photoexcitation of alkali atoms*," J. Phys. B (FTC) **42**, 191001 (2009).

[9] F. Anis and B. D. Esry, "*Ro-vibrational revivals structure of H_2^+ in short laser pulses*," Phys. Rev. A (2009), (to be submitted).

[10] S. De, I. Znakovskaya, D. Ray, F. Anis, N. Johnson, I. Bocharova, M. Magrakvelidze, B. Esry, C. Cocke, I. Litvinyuk, and M. Kling, "*Field-free orientation of CO molecules by femtosecond two-color laser fields*," Phys. Rev. Lett. **103**, 153002 (2009).

[11] B. Gaire, J. McKenna, A. Sayler, F. Anis, M. Zohrabi, N. G. Johnson, J. J. Hua, K. D. Carnes, B. D. Esry, and I. Ben-Itzhak, "*Zero-photon dissociationof H_2^+ in intense few cycle laser pulses*," Phys. Rev. Lett. (2009), (to be submitted).

[12] J. McKenna, F. Anis, B. Gaire, N. G. Johnson, M. Zohrabi, K. D. Carnes, B. D. Esry, and I. Ben-Itzhak, "*Suppressed Dissociation of H_2^+ Vibrational States by Reduced Dipole Coupling*," Phys. Rev. Lett. **103**, 103006 (2009).

[13] J. McKenna, F. Anis, A. M. Sayler, B. Gaire, N. G. Johnson, E. Parke, K. D. Carnes, B. D. Esry, and I. Ben-Itzhak, "*Temporal effects in H_2^+ intense-field fragmentation with few-cycle infrared laser pulses*," Phys. Rev. A (2009), (to be submitted).

[14] J. McKenna, A. Sayler, F. Anis, N. Johnson, B. Gaire, U. Lev, M. Zohrabi, K. Carnes, B. Esry, and I. Ben-Itzhak, "*Vibrationally-cold CO^{2+} in intense ultrashort laser pulses*," Phys. Rev. Lett. (2009), (submitted).

References

[15] P. Q. Wang, A. M. Sayler, K. D. Carnes, J. F. Xia, M. A. Smith, B. D. Esry, and I. Ben-Itzhak, Phys. Rev. A **74**, 043411 (2006).

[16] A. S. Alnaser, B. Ulrich, X. M. Tong, I. V. Litvinyuk, C. M. Maharjan, P. Ranitovic, T. Osipov, R. Ali, S. Ghimire, Z. Chang, C. D. Lin, and C. L. Cocke, Phys. Rev. A **72**, 030702 (2005).

[17] T. Ergler, A. Rudenko, B. Feuerstein, K. Zrost, C. D. Schroter, R. Moshammer, and J. Ullrich, PRL **97**, 193001 (2006).

[18] F. Légaré, K. F. Lee, I. V. Litvinyuk, P. W. Dooley, A. D. Bandrauk, D. M. Villeneuve, and P. B. Corkum, Phys. Rev. A **72**, 052717 (2005).

[19] T. Weber, M. Weckenbrock, A. Staudte, M. Hattass, L. Spielberger, O. Jagutzki, V. Mergel, H. Bocking, G. Urbasch, H. Giessen, H. Brauning, C. Cocke, M. Prior, and R. Dorner, Opt. Exp. **8**, 368 (2001).

[20] A. Giusti-Suzor, F. H. Mies, L. F. DiMauro, E. Charron, and B. Yang, Journal of Physics B: Atomic, Molecular and Optical Physics **28**, 309 (1995).

[21] J. H. Posthumus, Reports on Progress in Physics **67**, 623 (2004).

[22] F. He, C. Ruiz, and A. Becker, Phys. Rev. Lett. **99**, 083002 (2007).

[23] P. A. Orr, I. D. Williams, J. B. Greenwood, I. C. E. Turcu, W. A. Bryan, J. Pedregosa-Gutierrez, and C. W. Walter, Phys. Rev. Lett. **98**, 163001 (2007).

[24] J. J. Thomson, Phil. Mag. **13**, 561 (1907).

[25] J. J. Thomson and G. P. Thomson (Cambridge Univ. Press, 1928), 3rd ed.

[26] Ø. Burrau and K. Danske, Vid. Selsk. **7** (1927).

[27] E. Schrödinger, Phys. Rev. **28**, 1049 (1926).

[28] A. Carrington and R. A. Kennedy, *In Gas Phase Ion Chemistry*, vol. 3 (Academic Press Inc, London, 1985).

[29] D. R. Bates, The Journal of Chemical Physics **19**, 1122 (1951).

[30] E. E. Aubanel, J.-M. Gauthier, and A. D. Bandrauk, Phys. Rev. A **48**, 2145 (1993).

[31] V. N. Serov, A. Keller, O. Atabek, and N. Billy, Phys. Rev. A **68**, 053401 (2003).

[32] A. Giusti-Suzor and F. H. Mies, Phys. Rev. Lett. **68**, 3869 (1992).

[33] E. E. Aubanel, A. Conjusteau, and A. D. Bandrauk, Phys. Rev. A **48**, R4011 (1993).

[34] F. Châteauneuf, T.-T. Nguyen-Dang, N. Ouellet, and O. Atabek, J. Chem. Phys. **108**, 3974 (1998).

[35] K. Sändig, H. Figger, and T. W. Hänsch, Phys. Rev. Lett. **85**, 4876 (2000).

[36] P. Q. Wang, A. M. Sayler, K. D. Carnes, J. F. Xia, M. A. Smith, B. D. Esry, and I. Ben-Itzhak, J. Phys. B: Atomic, Molecular and Optical Physics Lett. **38**, L251 (2005).

[37] P. H. Bucksbaum, A. Zavriyev, H. G. Muller, and D. W. Schumacher, Phys. Rev. Lett. **64**, 1883 (1990).

[38] G. N. Gibson, M. Li, C. Guo, and J. Neira, Phys. Rev. Lett. **79**, 2022 (1997).

[39] I. D. Williams, P. McKenna, B. Srigengan, I. M. G. Johnston, W. A. Bryan, J. H. Sanderson, A. El-Zein, T. R. J. Goodworth, W. R. Newell, P. F. Taday, and A. J. Langley, J. Phys. B: Atomic, Molecular and Optical Physics **33**, 2743 (2000).

[40] A. Zavriyev, P. H. Bucksbaum, J. Squier, and F. Saline, Phys. Rev. Lett. **70**, 1077 (1993).

[41] A. Kondorskiy and H. Nakamura, Phys. Rev. A **66**, 053412 (2002).

[42] L. B. Madsen and M. Plummer, J. Phys. B: Atomic, Molecular and Optical Physics **31**, 87 (1998).

[43] B. D. Esry, A. M. Sayler, P. Q. Wang, K. D. Carnes, and I. Ben-Itzhak, Phys. Rev. Lett. **97**, 013003 (2006).

[44] V. Roudnev and B. D. Esry, Phys. Rev. Lett. **99**, 220406 (2007).

[45] M. Kling, C. Siedschlag, A. Verhoef, J. Kahn, M. Schultze, Y. Ni, T. Uphues, M. Uiberackerand, M. Drescher, F. Krausz, and M. Vrakking, Science **312**, 246 (2006).

[46] X. M. Tong and C. D. Lin, Phys. Rev. Lett. **98**, 123002 (2007).

[47] C. P. J. Martiny and L. B. Madsen, Phys. Rev. Lett. **97**, 093001 (2006).

[48] R. S. Mulliken, The Journal of Chemical Physics **7**, 20 (1939).

[49] G. H. Dunn, Phys. Rev. **172**, 1 (1968).

[50] F. von Busch and G. H. Dunn, Phys. Rev. A **5**, 1726 (1972).

[51] J. D. Argyros, Journal of Physics B: Atomic and Molecular Physics **7**, 2025 (1974).

[52] H. G. Dehmelt and K. B. Jefferts, Phys. Rev. **125**, 1318 (1962).

[53] C. B. Richardson, K. B. Jefferts, and H. G. Dehmelt, Phys. Rev. **165**, 80 (1968).

[54] S. Saha, K. K. Datta, D. Basu, and A. K. Barua, Journal of Physics B: Atomic and Molecular Physics **13**, 3755 (1980).

[55] A. Giusti-Suzor, X. He, O. Atabek, and F. H. Mies, Phys. Rev. Lett. **64**, 515 (1990).

[56] G. Jolicard and O. Atabek, Phys. Rev. A **46**, 5845 (1992).

[57] P. A. Orr, I. D. Williams, J. B. Greenwood, I. C. E. Turcu, W. A. Bryan, J. Pedregosa-Gutierrez, and C. W. Walter, Phys. Rev. Lett. **98**, 163001 (2007).

[58] J. H. Posthumus, J. Plumridge, L. J. Frasinski, K. Codling, E. J. Divall, A. J. Langley, and P. F. Taday, J. Phys. B: Atomic, Molecular and Optical Physics **33**, L563 (2000).

[59] T. Zuo and A. D. Bandrauk, Phys. Rev. A **52**, R2511 (1995).

[60] A. Staudte, D. Pavičić, S. Chelkowski, D. Zeidler, M. Meckel, H. Niikura, M. Schöffler, S. Schössler, B. Ulrich, P. P. Rajeev, T. Weber, T. Jahnke, D. M. Villeneuve, A. D. Bandrauk, C. L. Cocke, P. B. Corkum, and R. Dörner, Phys. Rev. Lett. **98**, 073003 (2007).

[61] P. B. Corkum, Phys. Rev. Lett. **71**, 1994 (1993).

[62] P. A. Franken, A. E. Hill, C. W. Peters, and G. Weinreich, Phys. Rev. Lett. **7**, 118 (1961).

[63] X. F. Li, A. L'Huillier, M. Ferray, L. A. Lompré, and G. Mainfray, Phys. Rev. A **39**, 5751 (1989).

[64] D. Ray, B. Ulrich, I. Bocharova, C. Maharjan, P. Ranitovic, B. Gramkow, M. Magrakvelidze, S. De, I. V. Litvinyuk, A. T. Le, T. Morishita, C. D. Lin, G. G. Paulus, and C. L. Cocke, Phys. Rev. Lett. **100**, 143002 (2008).

[65] M. Okunishi, T. Morishita, G. Prümper, K. Shimada, C. D. Lin, S. Watanabe, and K. Ueda, Phys. Rev. Lett. **100**, 143001 (2008).

[66] A.-T. Le, R. R. Lucchese, M. T. Lee, and C. D. Lin, Phys. Rev. Lett. **102**, 203001 (2009).

[67] I. V. Litvinyuk, K. F. Lee, P. W. Dooley, D. M. Rayner, D. M. Villeneuve, and P. B. Corkum, Phys. Rev. Lett. **90**, 233003 (2003).

[68] A. Rudenko, T. Ergler, B. Feuerstein, K. Zrost, C. Schrter, R. Moshammer, and J. Ullrich, Chemical Physics **329**, 193 (2006).

[69] V. Serov, A. Keller, O. Atabek, H. Figger, and D. Pavicic, Phys. Rev. A **72**, 033413 (2005).

[70] B. H. Bransden and C. J. Joachain, *Physics of Atoms and Molecules* (Pearson Education Limited, Harlow, England, 2003).

[71] Z. Amitay, A. Baer, M. Dahan, J. Levin, Z. Vager, D. Zajfman, L. Knoll, M. Lange, D. Schwalm, R. Wester, A. Wolf, I. F. Schneider, and A. Suzor-Weiner, Phys. Rev. A **60**, 3769 (1999).

[72] S.-I. Chu and D. A. Telnov, Physics Reports **390**, 1 (2004).

[73] E. Charron, A. Giusti-Suzor, and F. H. Mies, Phys. Rev. A **49**, R641 (1994).

[74] J. F. McCann and A. D. Bandrauk, Phys. Rev. A **42**, 2806 (1990).

[75] J. F. McCann and A. D. Bandrauk, The Journal of Chemical Physics **96**, 903 (1992).

[76] H. Abou-Rachid, T. T. Nguyen-Dang, and O. Atabek, The Journal of Chemical Physics **114**, 2197 (2001).

[77] R. Numico, A. Keller, and O. Atabek, Phys. Rev. A **57**, 2841 (1998).

[78] R. Numico, A. Keller, and O. Atabek, Phys. Rev. A **52**, 1298 (1995).

[79] I. Ben-Itzhak, P. Q. Wang, J. F. Xia, A. M. Sayler, M. A. Smith, K. D. Carnes, and B. D. Esry, Phys. Rev. Lett. **95**, 073002 (2005).

[80] J. J. Hua and B. D. Esry, Phys. Rev. A **78**, 055403 (2008).

[81] S. Chelkowski, T. Zuo, O. Atabek, and A. D. Bandrauk, Phys. Rev. A **52**, 2977 (1995).

[82] O. Atabek and R. Lefebvre, Phys. Rev. A **78**, 043419 (2008).

[83] B. D. Esry and H. R. Sadeghpour, Phys. Rev. A **60**, 3604 (1999).

[84] C. D. Lin, Physics Reports **257**, 1 (1995).

[85] M. W. J. Bromley and B. D. Esry, Phys. Rev. A **69**, 053620 (2004).

[86] J. Colgan, M. S. Pindzola, and F. Robicheaux, Phys. Rev. A **68**, 063413 (2003).

[87] S. J. Singer, K. F. Freed, and Y. B. Band, The Journal of Chemical Physics **79**, 6060 (1983).

[88] S. J. Singer, K. F. Freed, and Y. B. Band, The Journal of Chemical Physics **81**, 3091 (1984).

[89] S. J. Singer, K. F. Freed, and Y. B. Band, The Journal of Chemical Physics **81**, 3064 (1984).

[90] T. A. Green and J. M. Peek, Phys. Rev. **183**, 166 (1969).

[91] T. A. Green and J. M. Peek, Phys. Rev. Lett. **21**, 1732 (1968).

[92] C. Lefebvre, T. T. Nguyen-Dang, and O. Atabek, Phys. Rev. A **75**, 023404 (2007).

[93] J. H. Posthumus, J. Plumridge, M. K. Thomas, K. Codling, L. J. Frasinski, A. J. Langley, and P. F. Taday, Journal of Physics B: Atomic, Molecular and Optical Physics **31**, L553 (1998).

[94] M. Pont and M. Gavrila, Phys. Rev. Lett. **65**, 2362 (1990).

[95] R. N. Zare, The Journal of Chemical Physics **47**, 204 (1967).

[96] L. D. A. Siebbeles, M. Glass-Maujean, O. S. Vasyutinskii, J. A. Beswick, and O. Roncero, The Journal of Chemical Physics **100**, 3610 (1994).

[97] R. M. Wood, Q. Zheng, A. K. Edwards, and M. A. Mangan, Review of Scientific Instruments **68**, 1382 (1997).

[98] Q. Zheng, A. K. Edwards, R. M. Wood, and M. A. Mangan, Phys. Rev. A **52**, 3945 (1995).

[99] V. V. Kuznetsov and O. S. Vasyutinskii, The Journal of Chemical Physics **123**, 034307 (2005).

[100] X. M. Tong, Z. X. Zhao, A. S. Alnaser, S. Voss, C. L. Cocke, and C. D. Lin, J. Phys. B: Atomic, Molecular and Optical Physics **38**, 333 (2005).

[101] H. Stapelfeldt and T. Seideman, Rev. Mod. Phys. **75**, 543 (2003).

[102] M. Busuladžić, A. Gazibegović-Busuladžić, D. B. Milošević, and W. Becker, Phys. Rev. Lett. **100**, 203003 (2008).

[103] T. K. Kjeldsen and L. B. Madsen, Journal of Physics B: Atomic, Molecular and Optical Physics **40**, 237 (2007).

[104] J. Itatani, J. Levesque, D. Zeidler, H. Niikura, H. Pepin, J. C. Kiefferm, P. B. Corkum, and D. M. Villeneuve, Nature **432**, 867 (2004).

[105] K. Miyazaki, M. Kaku, G. Miyaji, A. Abdurrouf, and H. M. Faisal, F. Phys. Rev. Lett. **95**, 243903 (2005).

[106] R. Torres, R. de Nalda, and J. P. Marangos, Phys. Rev. A **72**, 023420 (2005).

[107] J. H. Posthumus, J. Plumridge, M. K. Thomas, K. Codling, L. J. Frasinski, A. J. Langley, and P. F. Taday, Journal of Physics B: Atomic, Molecular and Optical Physics **31**, L553 (1998).

[108] P. W. Dooley, I. V. Litvinyuk, K. F. Lee, D. M. Rayner, M. Spanner, D. M. Villeneuve, and P. B. Corkum, Phys. Rev. A **68**, 023406 (2003).

[109] R. W. Robinett, Physics Reports **392**, 1 (2004).

[110] S. Guérin, L. P. Yatsenko, H. R. Jauslin, O. Faucher, and B. Lavorel, Phys. Rev. Lett. **88**, 233601 (2002).

[111] C. Z. Bisgaard, M. D. Poulsen, E. Péronne, S. S. Viftrup, and H. Stapelfeldt, Phys. Rev. Lett. **92**, 173004 (2004).

[112] M. Leibscher, I. S. Averbukh, and H. Rabitz, Phys. Rev. Lett. **90**, 213001 (2003).

[113] F. Rosca-Pruna and M. J. J. Vrakking, Phys. Rev. Lett. **87**, 153902 (2001).

[114] J. J. Larsen, K. Hald, N. Bjerre, H. Stapelfeldt, and T. Seideman, Phys. Rev. Lett. **85**, 2470 (2000).

[115] H. Sakai, C. P. Safvan, J. J. Larsen, K. M. H. e, K. Hald, and H. Stapelfeldt, The Journal of Chemical Physics **110**, 10235 (1999).

[116] O. Ghafur, A. Rouzee, A. Gijsbertsen, W. K. Siu, S. Stolte, and M. J. J. Vrakking, Nat. Phys. **5**, 289 (2009).

[117] R. Tehini and D. Sugny, Phys. Rev. A **77**, 023407 (2008).

[118] T. Suzuki, Y. Sugawara, S. Minemoto, and H. Sakai, Phys. Rev. Lett. **100**, 033603 (2008).

[119] S. Zou, G. G. Balint-Kurti, and F. R. Manby, The Journal of Chemical Physics **127**, 044107 (2007).

[120] K. F. Lee, F. Legare, D. M. Villeneuve, and P. B. Corkum, Journal of Physics B: Atomic, Molecular and Optical Physics **39**, 4081 (2006).

[121] I. A. Bocharova, H. Mashiko, M. Magrakvelidze, D. Ray, P. Ranitovic, C. L. Cocke, and I. V. Litvinyuk, Phys. Rev. A **77**, 053407 (2008).

[122] S. C. Althorpe and T. Seideman, The Journal of Chemical Physics **113**, 7901 (2000).

[123] C. Wunderlich, E. Kobler, H. Figger, and T. W. Hänsch, Phys. Rev. Lett. **78**, 2333 (1997).

[124] D. Pavičić, A. Kiess, T. W. Hänsch, and H. Figger, Phys. Rev. Lett. **94**, 163002 (2005).

[125] J. B. Greenwood, I. M. G. Johnston, P. McKenna, I. D. Williams, T. R. J. Goodworth, J. H. Sanderson, W. A. Bryan, A. A. A. El-Zein, W. R. Newell, A. J. Langley, and E. J. Divall, Phys. Rev. Lett. **88**, 233001 (2002).

[126] E. Gagnon, P. Ranitovic, X.-M. Tong, C. L. Cocke, M. M. Murnane, H. C. Kapteyn, and A. S. Sandhu, Science **317**, 1374 (2007).

[127] J. Ullrich, R. Moshammer, R. Dörner, O. Jagutzki, V. Mergel, H. Schmidt-Böcking, and L. Spielberger, J. Phys. B: Atomic, Molecular and Optical Physics **30**, 2917 (1997).

[128] F. Martin, J. Fernandez, T. Havermeier, L. Foucar, T. Weber, K. Kreidi, M. Schoffler, L. Schmidt, T. Jahnke, O. Jagutzki, A. Czasch, E. P. Benis, T. Osipov, A. L. Landers, A. Belkacem, M. H. Prior, H. Schmidt-Bocking, C. L. Cocke, and R. Dorner, Science **315**, 629 (2007).

[129] R. Dörner, V. Mergel, O. Jagutzki, L. Spielberger, J. Ullrich, R. Moshammer, and H. Schmidt-Böcking, Phys. Rep. **330**, 95 (2000).

[130] J. H. Posthumus, B. Fabre, C. Cornaggia, N. de Ruette, and X. Urbain, Phys. Rev. Lett. **101**, 233004 (2008).

[131] A. M. Sayler, P. Q. Wang, K. D. Carnes, B. D. Esry, and I. Ben-Itzhak, Phys. Rev. A **75**, 063420 (2007).

[132] I. Ben-Itzhak, P. Wang, J. Xia, A. M. Sayler, M. A. Smith, J. Maseberg, K. D. Carnes, and B. D. Esry, Nucl. Instrum. Meth. **233**, 56 (2005).

[133] P. Wang, A. M. Sayler, K. D. Carnes, B. D. Esry, and I. Ben-Itzhak, Opt. Lett. **30**, 664 (2005).

[134] E. Charron, A. Giusti-Suzor, and F. H. Mies, Phys. Rev. Lett. **71**, 692 (1993).

[135] E. Charron, A. Giusti-Suzor, and F. H. Mies, Phys. Rev. Lett. **75**, 2815 (1995).

[136] J. J. Hua and B. D. Esry, Journal of Physics B: Atomic, Molecular and Optical Physics **42**, 085601 (2009).

[137] G. G. Paulus, F. Grasbon, H. Walther, P. Villoresi, M. Nisoli, S. Stagira, E. Priori, and S. De Silvestri, Nature **414**, 182 (2001).

[138] D. B. Milošević, G. G. Paulus, and W. Becker, Phys. Rev. Lett. **89**, 153001 (2002).

[139] V. Roudnev, B. D. Esry, and I. Ben-Itzhak, Phys. Rev. Lett. **93**, 163601 (2004).

[140] M. F. Kling, J. Rauschenberger, A. J. Verhoef, E. Hasovic, T. Uphues, D. B. Milosevic, H. G. Muller, and M. J. J. Vrakking, New Journal of Physics **10**, 025024 (2008).

[141] G. G. Paulus, F. Lindner, H. Walther, A. Baltuška, E. Goulielmakis, M. Lezius, and F. Krausz, Phys. Rev. Lett. **91**, 253004 (2003).

[142] A. Baltuška, T. Udem, M. Uiberacker, M. Hentschel, E. Goulielmakis1, C. Gohle, R. Holzwarth, V. S. Yakovlev1, A. Scrinzi1, T. W. Hnsch, and F. Krausz1, Nature (London) **421**, 611 (2003).

[143] T. Nakajima and S. Watanabe, Phys. Rev. Lett. **96**, 213001 (2006).

[144] Z. Chang, Phys. Rev. A **76**, 051403 (2007).

[145] H. Mashiko, S. Gilbertson, C. Li, S. D. Khan, M. M. Shakya, E. Moon, and Z. Chang, Phys. Rev. Lett. **100**, 103906 (2008).

[146] F. He, A. Becker, and U. Thumm, Phys. Rev. Lett. **101**, 213002 (2008).

[147] B. Fischer *et. al.* (2009), poster in Second Attosecond conference.

[148] V. Roudnev and B. D. Esry, Phys. Rev. A **76**, 023403 (2007).

[149] P. Q. Wang, A. M. Sayler, K. D. Carnes, B. D. Esry, and I. Ben-Itzhak, Opt. Lett. **30**, 664 (2005).

[150] X. Urbain, B. Fabre, E. M. Staicu-Casagrande, N. de Ruette, V. M. Andrianarijaona, J. Jureta, J. H. Posthumus, A. Saenz, E. Baldit, and C. Cornaggia, Phys. Rev. Lett. **92**, 163004 (2004).

[151] A. S. Alnaser, B. Ulrich, X. M. Tong, I. V. Litvinyuk, C. M. Maharjan, P. Ranitovic, T. Osipov, R. Ali, S. Ghimire, Z. Chang, C. D. Lin, and C. L. Cocke, Phys. Rev. A **72**, 030702 (2005).

Appendix A

Dipole matrix element

We used a laser pulse linearly polarized along the z-axis in all of our calculations. For this case, though, we need only the z-component of the dipole operator. We must thus calculate the following dipole matrix elements:

$$D_{\alpha\alpha'} = -\langle \Phi_\alpha | z | \Phi_{\alpha'} \rangle. \tag{A.1}$$

In Eq. (A.1), $\Phi_\alpha = \Omega^{J\Pi}_{M\Lambda}\phi_{n\Lambda\sigma_z}$. The polarization axis is defined in the lab frame, but we performed all adiabatic calculations of the electronic states in the body-fixed frame. So, to evaluate the matrix elements, we transform the dipole operator from the lab frame to the body frame. The lab frame coordinate z is related to the body-fixed coordinates as follows:

$$d_z = -z = -\sum_{\mu=0,\pm1} D^{1*}_{0\mu}(\phi,\theta,\chi) r'_\mu. \tag{A.2}$$

To connect most directly with the electronic part of the body-frame dipole matrix elements (involving $\phi_{n\Lambda\sigma_z}$), we can rewrite the spherical body-frame components r'_0 and $r'_\pm$ in terms of the cylindrical coordinates as $r'_0 = z'$ and $r'_\pm = \mp(1/\sqrt{2})\rho'$ (the χ-dependence of $r'_\pm$ is included in the D-functions). This transformation has been made to be able to use existing electronic dipole couplings. Using Eq. (A.2) to transform z into body-fixed coordinates and

using Eqs. (2.7)-(2.8) in Eq. (A.1), we obtain

$$\begin{aligned} D_{\alpha\alpha'} &= -\sum_{\mu} \langle \phi_{n\sigma_z\Lambda} \Omega^{J\Pi}_{M\Lambda} | D^{1*}_{0\mu} r_\mu | \phi_{n'\sigma'_z\Lambda'} \Omega^{J'\Pi'}_{M'\Lambda'} \rangle \\ &= -\sum_{\mu} \langle \phi_{n\sigma_z\Lambda} | r_\mu | \phi_{n'\sigma'_z\Lambda'} \rangle \langle \Omega^{J\Pi}_{M\Lambda} | D^{1*}_{0\mu} | \Omega^{J'\Pi'}_{M'\Lambda'} \rangle . \end{aligned} \tag{A.3}$$

The first matrix element is determined numerically from the BO states, while the second is purely angular and is analytic:

$$\begin{aligned} \langle \Omega^{J\Pi}_{M\Lambda} | D^{1*}_{0\mu} | \Omega^{J'\Pi'}_{M'\Lambda'} \rangle \;=\; & \frac{1}{2}\sqrt{\frac{(2J'+1)(2J+1)}{(1+\delta_{\Lambda'0})(1+\delta_{\Lambda 0})}} (-1)^{\mu - M' + \Lambda'} \begin{pmatrix} J & 1 & J' \\ -M & 0 & M' \end{pmatrix} \Bigg[\begin{pmatrix} J & 1 & J' \\ -\Lambda & -\mu & \Lambda' \end{pmatrix} \\ & + \Pi (-1)^{J+\Lambda} \begin{pmatrix} J & 1 & J' \\ \Lambda & -\mu & \Lambda' \end{pmatrix} + \Pi' (-1)^{J'+\Lambda'} \begin{pmatrix} J & 1 & J' \\ -\Lambda & -\mu & -\Lambda' \end{pmatrix} \\ & + \Pi\Pi' (-1)^{J+J'+\Lambda+\Lambda'} \begin{pmatrix} J & 1 & J' \\ \Lambda & -\mu & -\Lambda' \end{pmatrix} \Bigg] . \end{aligned} \tag{A.4}$$

These dipole matrix elements preserve all of the expected selection rules.

A.1 Structure of dipole matrix for initial $M = 0$

For the bound $1s\sigma_g$ channel of H_2^+, the parity Π is given by $\Pi = (-1)^J$. We have used an initial $M = 0$ in most of the calculations. For $M = 0 = M'$, the dipole selection rules require $J' = J \pm 1$. Moreover, for parallel transitions, *i.e.* $\Lambda' = \Lambda$, the body frame reflection symmetry will change as $\sigma'_z = -\sigma_z$ and only $\mu = 0$ will contribute to the angular matrix elements. For perpendicular transitions, $\Lambda' = \Lambda \pm 1$ are the allowed transitions and require $(-1)^{\Lambda'}\sigma'_z = -(-1)^{\Lambda}\sigma_z$ ($g \leftrightarrow u$ in standard notation). In this case, the $\mu = \pm 1$ terms add to give the angular contribution to the matrix elements. After implementing the dipole selection rules, our total dipole matrix has the structure indicated in Fig. A.1 for $n = 1, 2$ and $\Lambda = 0, 1$. Each block is for a given total angular momentum J, starting from $J = 0$, for which the only allowed value of Λ is zero — hence we have a 6×6 block. For the remaining J's, the blocks are 8×8. Of the 6 elements corresponding to $\Lambda = 0$, three are for $\sigma_z = 1$, and the other three are for $\sigma_z = -1$. One of these three elements is for $n = 1$; and the other two, for $n = 2$. For the 8×8 blocks, the last two columns or rows are for couplings with

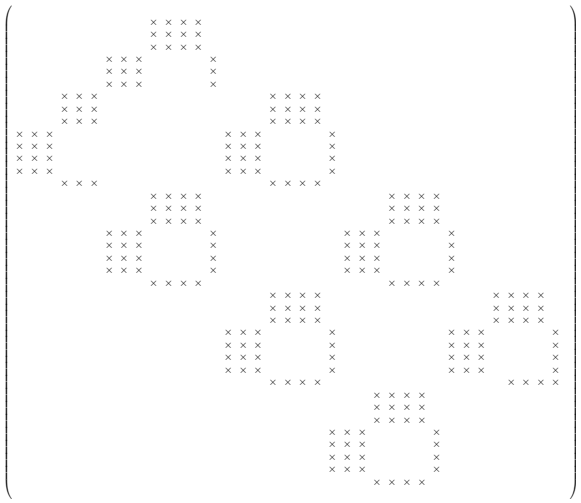

Figure A.1 Structure of the dipole coupling matrix. Blanks indicate vanishing matrix elements, and $\times$s, non-zero elements.

$\Lambda = 1, \sigma_z = \pm 1$ and $n = 2$. Overall, the dipole matrix has a block tri-diagonal structure as one would expect from the dipole selection rules and our choice to increment J most slowly in our basis.

Basis index	J	M	Π	Λ	σ_z	n
1	0	0	+	0	+	1
2	0	0	+	0	+	2
3	0	0	+	0	+	2
4	0	0	+	0	−	1
5	0	0	+	0	−	2
6	0	0	+	0	−	2
7	1	0	−	0	+	1
8	1	0	−	0	+	2
9	1	0	−	0	+	2
10	1	0	−	0	−	1
11	1	0	−	0	−	2
12	1	0	−	0	−	2
13	1	0	−	1	+	2
14	1	0	-	1	−	2
15	2	0	+	0	+	1
16	2	0	+	0	+	2
17	2	0	+	0	+	2
18	2	0	+	0	−	1
19	2	0	+	0	−	2
20	2	0	+	0	−	2
21	2	0	+	1	+	2
22	2	0	+	1	−	2
23	3	0	−	0	+	1
24	3	0	−	0	+	2
25	3	0	−	0	+	2
26	3	0	−	0	−	1
27	3	0	−	0	−	2
28	3	0	−	0	−	2
29	3	0	−	1	+	2
30	3	0	−	1	−	2

Table A.1 Quantum numbers in each column (row) of the basis in the dipole matrix shown in Fig. A.1. The pattern will continue up to $J_{\max}$. For odd J's, the first six rows will be omitted. It is described earlier in Sec. 2.3.7 that asymptotically molecular states are linear combinations of Stark states for p+H with quantum numbers $n_1, n_2, |\Lambda|$. Note that $n = n_1 + n_2 + \Lambda + 1$, and only n is shown in the last column.

Appendix B

Derivation of the momentum distribution

Here I will document in detail all of the steps mentioned in Sec. 2.3.7 in going from Eq. (2.36) to Eq. (2.37) and also the steps involved in deriving Eq. (2.38). From Eq. (2.36),

$$e^{i\mathbf{K}.\mathbf{R}}|nlm\rangle_A \quad \xrightarrow[R\to\infty]{} \frac{1}{KR}\sum_{Lm_L} i^L j_L(KR)Y^*_{Lm_L}(\hat{K})Y_{Lm_L}(\hat{R})|nlm\rangle_A \tag{B.1}$$

Since our molecular basis is defined in terms of the total orbital angular momentum J, we construct the total angular momentum basis from $|Lm_L\rangle \equiv Y_{Lm_L}(\hat{R})$ and $|nlm\rangle_A$ as

$$|JMLln\rangle_A = \sum_{m_L m}\langle Llm_L m|JM\rangle|Lm_L nlm\rangle_A \tag{B.2}$$

here $\langle Llm_L m|JM\rangle$ are Clebsch-Gordon (CG) coefficients and $|Lm_L nlm\rangle_A$ represents $|Lm_L\langle|nlm\rangle_A$. Similarly, for the electron localized on proton B, we can define $|JMLln\rangle_B$ as

$$|JMLln\rangle_B = \sum_{m_L m}\langle Llm_L m|JM\rangle|Lm_L nlm\rangle_B \tag{B.3}$$

Now, we will return to the molecular basis and express them in terms of the basis defined in Eqs. (B.2) and (B.3). Recalling molecular basis functions are

$$|\Phi_\alpha\rangle = |JM\Pi n\Lambda\sigma_z\rangle \equiv \Omega^{J\Pi}_{M\Lambda}|n\Lambda\sigma_z\rangle \tag{B.4}$$

where $|n\Lambda\sigma_z\rangle \equiv \phi_{n\Lambda\sigma_z}(R;\xi,\eta)$. Since the χ dependence is incorporated into $\Omega^{J\pi}_{M\Lambda}$, $|n\Lambda\sigma_z\rangle$ and $|n-\Lambda\sigma_z\rangle$ are the same. In a more general form, Φ_α is

$$\Phi_\alpha \;=\; \sqrt{\frac{2J+1}{8\pi^2}}\frac{1}{\sqrt{2(1+\delta_{\Lambda 0})}}\Big[D^J_{-M-\Lambda}|n\Lambda\sigma_z\rangle + \pi(-1)^{J+\Lambda}D^J_{-M\Lambda}|n-\Lambda\sigma_z\rangle\Big] \tag{B.5}$$

Asymptotically, the electronic wave function in the molecular basis $|n\Lambda(\sigma_z = \pm)\rangle$ can be defined in terms of the body-frame (BF) atomic basis ($|nl\Lambda\rangle$) with the electron localized on proton $A(B)$ as

$$\begin{aligned} |n\Lambda\sigma_z\rangle &= \frac{1}{\sqrt{2}}(|nl\Lambda\rangle_A + \sigma_z|nl\Lambda\rangle_B) \\ |n-\Lambda\sigma_z\rangle &= \frac{1}{\sqrt{2}}(|nl-\Lambda\rangle_A + \sigma_z|nl-\Lambda\rangle_B). \end{aligned} \tag{B.6}$$

The molecular basis functions $|n\Lambda\sigma_z\rangle$ are calculated numerically and the above expressions are true up to an overall phase. Since the functions are defined to be real, the phase can be +1 or -1. More precisely,

$$\begin{aligned} |n\Lambda\sigma_z\rangle &= \frac{s_\beta}{\sqrt{2}}(|nl\Lambda\rangle_A + \sigma_z|nl\Lambda\rangle_B) \\ |n-\Lambda\sigma_z\rangle &= \frac{s_\beta}{\sqrt{2}}(|nl-\Lambda\rangle_A + \sigma_z|nl-\Lambda\rangle_B) \end{aligned} \tag{B.7}$$

where parameter s_β is the overall phase for each $|n\Lambda\sigma_z\rangle$. The phase becomes important to asymptotically define electron localization on each center. Moreover, asymptotically $|n\Lambda\sigma_z\rangle$ goes to the linear combination of atomic Stark states of p+H and not the spherical basis as expressed in Eq. (B.7). However, these states can be combined to get the spherical basis. We have opted to write the asymptotic relation between the molecular and atomic bases in this form to take advantage of the properties of spherical harmonics. Thus, implicitly, each $|nl\Lambda\rangle_{A(B)}$ atomic state is a linear combination of Stark states. Also note that $|nl\Lambda\rangle_{A(B)}$ is not equivalent to $|nl-\Lambda\rangle_{A(B)}$. The body-frame atomic basis on the right-hand side in Eq. (B.7) is related to the lab-frame $|nlm\rangle_{A(B)}$ by the Wigner rotation matrix as

$$|nl\pm\Lambda\rangle_{A(B)} = \sum_m D^l_{m\pm\Lambda}|nlm\rangle_{A(B)}. \tag{B.8}$$

Using Eqs. (B.5), (B.7) and (B.8) in Eq. (B.4), we get

$$\begin{aligned} |JM\Pi n\Lambda\sigma_z\rangle = \sqrt{\frac{2J+1}{8\pi^2}}\frac{1}{\sqrt{2(1+\delta_{\Lambda 0})}}\sum_m \left(D^J_{-M-\Lambda}D^l_{m\Lambda} + \Pi(-1)^{J+\Lambda}D^J_{-M\Lambda}D^l_{m-\Lambda}\right) \\ \times \frac{s_\alpha}{\sqrt{2}}\left(|nlm\rangle_A + \sigma_z|nlm\rangle_B\right) \end{aligned} \tag{B.9}$$

In the above equation, the product of two D-functions from Ref. [89] can be expressed as

$$\begin{aligned} D^J_{-M-\Lambda} D^l_{m\Lambda} &= (-)^{-M-\Lambda} D^{J*}_{M\Lambda} D^l_{m\Lambda} \\ &= \sum_L \sum_{m_L} (2L+1) \begin{pmatrix} J & l & L \\ -M & m & m_L \end{pmatrix} \begin{pmatrix} J & l & L \\ -\Lambda & \Lambda & 0 \end{pmatrix} D^{L*}_{m_L 0}. \end{aligned} \tag{B.10}$$

Similarly,

$$\begin{aligned} D^J_{-M\Lambda} D^l_{m-\Lambda} &= (-)^{-M+\Lambda} D^{J*}_{M-\Lambda} D^l_{m\Lambda} \\ &= \sum_L \sum_{m_L} (2L+1) \begin{pmatrix} J & l & L \\ -M & m & m_L \end{pmatrix} \begin{pmatrix} J & l & L \\ \Lambda & -\Lambda & 0 \end{pmatrix} D^{L*}_{m_L 0}. \end{aligned} \tag{B.11}$$

Moreover,

$$D^{L*}_{m_L 0} = \sqrt{\frac{8\pi^2}{2L+1}} Y_{Lm_L}. \tag{B.12}$$

The factor $\sqrt{8\pi^2/2L+1}$ ensures normalization with respect to all angles, namely ϕ, θ, and χ. Substituting the above three equations into Eq. (B.9) gives

$$\begin{aligned} |JM\Pi n\Lambda\sigma_z\rangle = \sqrt{\frac{2J+1}{8\pi^2}} \frac{1}{\sqrt{2(1+\delta_{\Lambda 0})}} \sqrt{8\pi^2} \sum_L \sqrt{2L+1} \begin{pmatrix} J & l & L \\ -\Lambda & \Lambda & 0 \end{pmatrix} (1+\pi(-1)^{J+\Lambda+J+l+L}) \\ \times \sum_{m_L m} \begin{pmatrix} J & l & L \\ -M & m & m_L \end{pmatrix} Y_{Lm_L} \left\{ \frac{s_\beta}{\sqrt{2}} (|nlm\rangle_A + \sigma_z |nlm\rangle_B) \right\}. \end{aligned} \tag{B.13}$$

We used the following identity to convert the $3j$ to a Clebsch-Gordon coefficient

$$\begin{aligned} \sqrt{2J+1} \begin{pmatrix} J & l & L \\ -M & m & m_L \end{pmatrix} &= \sqrt{2J+1} (-)^{J+l+L} \begin{pmatrix} L & l & J \\ m_L & m & -M \end{pmatrix} \\ &= (-)^{J+l+L} (-)^{L-l+M} \langle Llm_L m | JM \rangle \\ &= (-)^{J+M} \langle Llm_L m | JM \rangle. \end{aligned}$$

Rearranging the above equation,

$$\begin{aligned} |JM\Pi n\Lambda\sigma_z\rangle = \frac{1}{\sqrt{2(1+\delta_{\Lambda 0})}} \sum_L \sqrt{\frac{2L+1}{2J+1}} (-)^{J+M+J+\Lambda} \langle Ll0\Lambda | J\Lambda \rangle (1+\Pi(-1)^{L+l+\Lambda}) \\ \times \frac{s_\beta}{\sqrt{2}} \left[\sum_{m_L m} (-)^{J+M} \sqrt{2J+1} \begin{pmatrix} L & l & J \\ m_L & m & -M \end{pmatrix} Y_{Lm_L} |nlm\rangle_A \right. \\ \left. + \sigma_z \sum_{m_L m} (-)^{J+M} \sqrt{2J+1} \begin{pmatrix} L & l & J \\ m_L & m & -M \end{pmatrix} Y_{Lm_L} |nlm\rangle_B \right] \end{aligned}$$

The two sums in the square bracket can be recognized as the total orbital angular momentum basis defined in Eqs. (B.2) and (B.3), respectively. Finally, we will have

$$|JM\Pi n\Lambda\sigma_z\rangle = \frac{1}{\sqrt{2(1+\delta_{\Lambda 0})}}\sum_L \sqrt{\frac{2L+1}{2J+1}}.(-)^{M+\Lambda}\langle Ll0\Lambda|J\Lambda\rangle(1+\Pi(-1)^{L+l+\Lambda}) \times\left\{\frac{s_\beta}{\sqrt{2}}(|JMLln\rangle_A+\sigma_z|JMLln\rangle_B)\right\} \tag{B.14}$$

Once we have developed Eq. (B.14), it becomes easier to transform between the BF molecular basis and the LF atomic basis. We can express $|JMLln\rangle_A$ as

$$|JMLln\rangle_A = \sum_{\Pi\Lambda\sigma_z}\langle JM\Pi n\Lambda\sigma_z|JMLln\rangle_A|JM\Pi n\Lambda\sigma_z\rangle \tag{B.15}$$

We can write a similar equation for $|JMLln\rangle_B$. Using Eq. (B.14), we have

$$|JMLln\rangle_{A(B)} = \sum_{\Pi\Lambda}(-)^{J+\Lambda}\sqrt{\frac{2L+1}{2J+1}}\frac{1}{\sqrt{2(1+\delta_{\Lambda 0})}}(1+\Pi(-)^{L+l+\Lambda})\langle Ll0\Lambda|J\Lambda\rangle \times\frac{1}{\sqrt{2}}\left(s_{\beta_+}|JM\Pi n\Lambda+\rangle \pm s_{\beta_-}|JM\Pi n\Lambda-\rangle\right) \tag{B.16}$$

In the above equation, the symbol $\alpha_{+(-)}$ has been adopted to express $\alpha=\{JM\Pi n\Lambda+(-)\}$. Also, $s_{\beta_{+(-)}}$ represents $|n\Lambda+(-)\rangle$. Using Eqs. (B.2) and (B.16) in Eq. (B.1), the final expression for the $e^{i\mathbf{K}.\mathbf{R}}|nlm\rangle_A$ is as follows:

$$e^{i\mathbf{K}.\mathbf{R}}|nlm\rangle_A \xrightarrow[R\to\infty]{} \sum_{Lm_LJ\Pi\Lambda}(-)^{M+\Lambda}i^L Y^*_{Lm_L}(\hat{K})j_L(KR)\sqrt{\frac{2L+1}{2J+1}}\langle Ll0\Lambda|J\Lambda\rangle\langle Llm_Lm|JM\rangle \times\frac{(1+\Pi(-)^{L+l+\Lambda})}{\sqrt{2(1+\delta_{\Lambda 0})}}\frac{1}{\sqrt{2}}\{s_{\beta_+}|JM\Pi n\Lambda+\rangle+s_{\beta_-}|JM\Pi n\Lambda-\rangle\} \tag{B.17}$$

Equation (B.17) appears as Eq. (2.37).

From Eq. (2.35),

$$\Psi_A(\mathbf{K},\mathbf{R},\mathbf{r}) = \sum_\alpha C_\alpha(\mathbf{K})F_{E\alpha}(R)\Phi_\alpha(R;\hat{R},\mathbf{r}). \tag{B.18}$$

Asymptotically,

$$F_{E\alpha} \xrightarrow[R\to\infty]{} \frac{1}{KR}\sin(KR-\frac{\kappa\pi}{2}+\delta_{E\alpha}) \tag{B.19}$$

where,

$$\kappa(\kappa+1) = \zeta^2$$

and $\delta_{E\alpha}$ is the scattering phase shift for each $F_{E\alpha}$. The discussion about κ has already come following Eq. (2.39).

In a half-collision problem, the scattering solution can be written as the linear combination of an outgoing plane wave and an incoming spherical wave,

$$\Psi^{-}_{(\mathrm{sc})}(\mathbf{K},\mathbf{R},\mathbf{r}) \quad \xrightarrow[R\to\infty]{} D\left[e^{i\mathbf{K}.\mathbf{R}} + f^{*}(K.\hat{R})\frac{e^{-iKR}}{R}\right]|nlm\rangle_A \tag{B.20}$$

where, $e^{i\mathbf{K}.\mathbf{R}}|nlm\rangle$ is defined in Eq. (2.37) in terms of the BO basis Φ_α. In Eq. (2.37), the $j_L(KR)$ are spherical Bessel function, and behave as $\sin(KR - L\pi/2)/KR$ asymptotically. The next step will be to use the asymptotic form for $F_{E\alpha}$ defined in Eq. (B.19) and $j_L(KR)$ in Eqs. (B.18) and (B.17) and then compare the coefficients of e^{iKR}/R in both equations and also project $\langle\Phi_\alpha|$ to get

$$\begin{aligned} C_\alpha(\mathbf{K}) =& G(-)^{M+\Lambda}e^{i\pi\kappa/2-i\delta_{E\alpha}}\sum_{Lm_L} Y^{*}_{Lm_L}(\hat{K})\sqrt{\frac{2L+1}{2J+1}}\langle Ll0\Lambda|J\Lambda\rangle\langle Llm_Lm|JM\rangle \\ &\times\frac{(1+\Pi(-)^{L+l+\Lambda})}{\sqrt{2(1+\delta_{\Lambda 0})}}\frac{s_\beta}{\sqrt{2}} \end{aligned} \tag{B.21}$$

The coefficient G can be obtained from energy normalization of the continuum states $F_{E\alpha}(R)$. This completes the discussion for the derivation of the continuum state and results in the following final equation ($|\mathbf{K},nlm\rangle_A \equiv \Psi_A(\mathbf{K},\mathbf{R},\mathbf{r})$).

$$\begin{aligned} |\mathbf{K},nlm\rangle_A =& \sum_{Lm_LJ\Pi\Lambda} e^{i\frac{\kappa\pi}{2}}Y^{*}_{Lm_L}(\hat{K})(-)^{M+\Lambda}\sqrt{\frac{2L+1}{2J+1}}\langle Ll0\Lambda|J\Lambda\rangle\langle Llm_Lm|JM\rangle \\ &\times\frac{(1+\Pi(-)^{L+l+\Lambda})}{\sqrt{2(1+\delta_{\Lambda 0})}}\frac{1}{\sqrt{2}}\{s_{\beta_+}e^{-i\delta_{E\alpha_+}}|E\alpha_+\rangle + s_{\beta_-}e^{-i\delta_{E\alpha_-}}|E\alpha_-\rangle\} \end{aligned} \tag{B.22}$$

In the above equation, $|E\alpha\rangle \equiv F_{E\alpha}(R)\Phi_\alpha(\hat{R},)$. Equation (B.22) appeared in Sec. 2.3.7 as Eq. (2.38). Further, the continuum wave function needs to be symmetrized with respect to exchange of nuclei, which is discussed in Sec. 2.3.7.

Appendix C

Convergence results

v	Number of grid point			
	Grid in Fig. 2.1(a)			WKB grid
	1600	2000	2400	3739
0	0.0000	0.0000	0.0000	0.0000
1	0.0003	0.0003	0.0003	0.0003
2	0.0103	0.0103	0.0103	0.0103
3	0.0698	0.0698	0.0698	0.0698
4	0.1584	0.1585	0.1585	0.1585
5	0.3191	0.3191	0.3192	0.3192
6	0.4779	0.4780	0.4781	0.4781
7	0.6354	0.6356	0.6357	0.6357
8	0.7921	0.7923	0.7924	0.7924
9	0.8595	0.8596	0.8596	0.8596
10	0.7085	0.7082	0.7081	0.7081
11	0.6150	0.6151	0.6152	0.6152
12	0.5605	0.5602	0.5649	0.5600
13	0.5780	0.5776	0.5774	0.5774
14	0.5351	0.5350	0.5349	0.5349
15	0.4683	0.4682	0.4681	0.4681
16	0.3921	0.3919	0.3918	0.3918
17	0.3130	0.3125	0.3123	0.3123
18	0.1294	0.1285	0.1279	0.1279
19	0.0079	0.0078	0.0078	0.0078
FC-averaged	0.1853	0.1853	0.1854	0.1853

Table C.1 Change in dissociation probability with number of grid points of a 70.a.u. box for each v and also in FC-averaged. $\tau_{\mathrm{FWHM}} = 10$ fs, $I = 10^{14}$ W/cm^2.

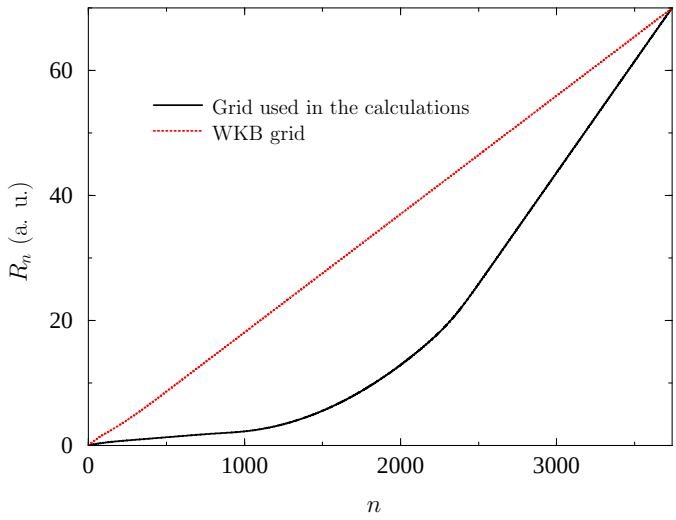

Figure C.1 Non-uniform grid used in all calculations (black solid line) and WKB grid (red dotted line). We call the second grid WKB as it is based on the local wavelength of the continuum wave function for the maximum energy component of the wave function.

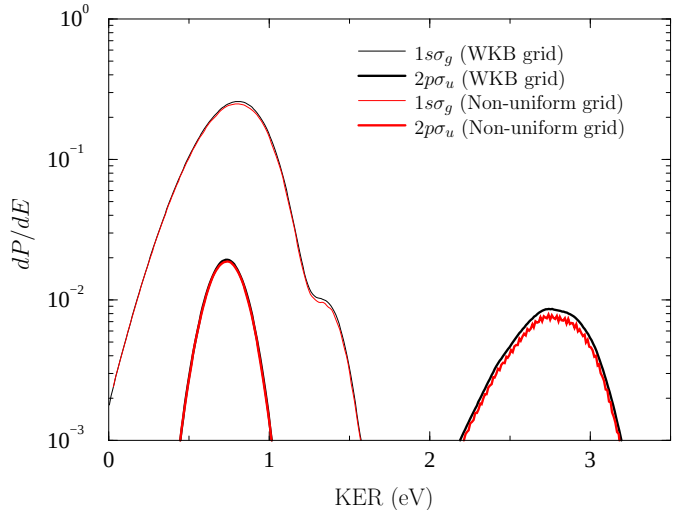

Figure C.2 Same as Fig. 6.5 along with KER-distribution obtained by using WKB grid (shown in Fig. C.1) for $v = 3$. The error in total dissociation probability is 0.26 percent. $\tau_{\mathrm{FWHM}} = 10$ fs and $I = 5 \times 10^{13}$ W/cm^2

v	Two channels	including $n = 2$ manifold	maximum P_{D} $n = 2$ manifold	final P_{D} $n = 2$ manifold
0	0.0000	0.0000	0.0025	0.0000
1	0.0002	0.0003	0.0030	0.0000
2	0.0093	0.0103	0.0037	0.0000
3	0.0721	0.0698	0.0054	0.0002
4	0.1486	0.1585	0.0078	0.0005
5	0.3144	0.3192	0.0105	0.0005
6	0.4569	0.4781	0.0154	0.0023
7	0.6172	0.6357	0.0213	0.0055
8	0.7864	0.7924	0.0263	0.0081
9	0.8609	0.8596	0.0342	0.0118
10	0.7093	0.7081	0.0321	0.0118
11	0.6184	0.6152	0.0333	0.0127
12	0.5678	0.5600	0.0314	0.0117
13	0.5778	0.5774	0.0311	0.0119
14	0.5344	0.5349	0.0321	0.0133
15	0.4671	0.4681	0.0394	0.0174
16	0.3879	0.3918	0.0486	0.0216
17	0.3098	0.3123	0.0410	0.0145
18	0.1351	0.1279	0.0296	0.0036
19	0.0079	0.0078	0.0258	0.0004
FC-averaged	0.1817	0.1853	0.0089	0.0016

Table C.2 Comparison of the two-channels dissociation probabilities with calculations including the $n = 2$ manifold. The forth column shows the maximum population in the $n = 2$ manifold during the pulse and the last column is the final population in the higher electronic channels. $\tau_{\mathrm{FWHM}} = 10$ fs and $I = \times 10^{14}$ W/cm^2.

v	Total dissociation probability	maximum P_{D} $n = 2$ manifold	final P_{D} $n = 2$ manifold
0	0.0000	0.0032	0.0000
1	0.0003	0.0038	0.0000
2	0.0064	0.0045	0.0000
3	0.0492	0.0060	0.0001
4	0.1219	0.0087	0.0007
5	0.2341	0.0120	0.0011
6	0.3481	0.0162	0.0018
7	0.4925	0.0224	0.0054
8	0.6366	0.0277	0.0097
9	0.6883	0.0283	0.0098
10	0.5890	0.0268	0.0088
11	0.5359	0.0277	0.0092
12	0.5114	0.0285	0.0097
13	0.4997	0.0302	0.0110
14	0.4712	0.0355	0.0143
15	0.4111	0.0469	0.0224
16	0.3513	0.0594	0.0308
17	0.2852	0.0554	0.0228
18	0.1134	0.0414	0.0065
19	0.0073	0.0391	0.0009
FC-averaged	0.1435	0.0095	0.0016

Table C.3 Total dissociation probabilities with calculations including the $n = 2$ manifold in the second column. The third column shows the maximum population in the $n = 2$ manifold during the pulse and the last column is the final population in the higher electronic channels. $\tau_{\mathrm{FWHM}} = 7$ fs and $I = 1.2 \times 10^{14}$ W/cm^2.

Intensity (W/cm^2)	τ_{FWHM} (fs)	$J_{\max}$
10^{14}	5	34
1.2×10^{14}	7	45
10^{14}	10	47
10^{13}	45	38
10^{13}	60	40
10^{13}	90	42
10^{13}	135	43

Table C.4 Intensities in the first column are the maximum for each pulse length in our calculations. The third column shows the maximum number of partial waves populated